Interaction Of Molecular Rydberg States With Metal Surfaces

A thesis submitted to the
University of Oxford for the
degree of Doctor of Philosophy

Geoffrey Robert Lloyd
Saint Edmund Hall. Trinity Term 2005

Physical Chemistry Laboratory
Department of Chemistry
University of Oxford

Dedicated to

Mum, Dad, Alison and Casper.

Interaction of Molecular Rydberg States with Metal Surfaces

A thesis submitted in partial fulfilment of the requirements for degree of Doctor of Philosophy in the University of Oxford by

Geoffrey Robert Lloyd

St. Edmund Hall

Trinity 2005

The interaction between high-n Rydberg states of molecular hydrogen and metal surfaces has been investigated for the first time. Rydberg states of hydrogen possessing either 0 or 2 units of rotational angular momentum, defined by the quantum number N^+, and principal quantum numbers in the range $n = 17 - 22$ (for the $N^+ = 2$ states) and $n = 41 - 45$ (for the $N^+ = 0$ states) are directed at a grazing angle onto a metal surface (gold or aluminium). At a sufficiently close distance ionisation may occur via tunnelling of the Rydberg electron into the vacant metal conduction band. Any ions formed in the vicinity of the metal are extracted by the application of an electric field and information about the distance at which the ions are formed can be inferred from the magnitude of the applied field required for detection.

Two novel effects are observed. Firstly, it appears that the rotation of the $H_2{}^+$ core has a significant effect on the ionisation properties of the Rydberg states in a manner akin to rotational autoionisation, such that the rotational energy of the core is given up to the Rydberg electron. Secondly, the surface ionisation profiles do not vary smoothly with applied field suggesting that at certain fields the feasibility of ionisation is either enhanced or reduced. A preliminary discussion of the origin of the structure is presented in terms of the crossings in the Stark map between the $N^+ = 0$ and $N^+ = 2$ Stark manifolds.

The development of a theoretical model, and an associated Fortran program, involving the technique of complex scaling is also reported. The hydrogen molecules are modeled using an atomic hydrogen system which provides a good first approximation to the behaviour of the Rydberg electron for states with $n > 5$. Energies and linewidths, for states with principal quantum number $n = 6 - 9$ interacting with a model surface, are explicitly calculated at a range of surface separations. From this information, predictions of the ionisation behaviour expected for states of higher principal quantum number are presented.

PUBLICATIONS

1. "Ionisation of hydrogen Rydberg molecules at a metal surface"
   G. R. Lloyd, S. R. Procter, and T. P. Softley, Phys. Rev. Lett. **95**, 133202 (2005)

ACKNOWLEDGEMENTS

The road has been somewhat long, and during the journey I have had the good fortune to meet many people who have been there to share both the good and the bad times with me; people who have given me more of their time, companionship and expertise than was perhaps warranted by my seeming ability to position the deadline for finishing this thesis at "next year".

Firstly I would like to thank my supervisor, Professor Tim Softley. He not only gave me the support and supervision that was essential to the project but also allowed me to continue in the group in order to complete this task. His eternal optimism, when mine was lacking, that "the experiment *will* work next week", and his ability to convince me of this fact, finally proved correct and the fruits of his belief are contained within. I am sure at times I tested his patience but he never let on. This was demonstrated when I dismantled the laser, and seemingly dumbfounded by my inability to get the thing working, Tim suggested "you may need to realign that". A sense of humour at such a difficult time was most appreciated.

Many people have passed through the doors of the Softley group office during my time there and all deserve mention for guiding and distracting me over the years. Sadly there is only room to list a few. Special mention must go to Simon Procter whose experimental expertise proved invaluable while grappling with the intricacies of lasers and electronics. He was always on hand to see the funny side of any disaster and to go for a pint with on those long winter nights, for which I, if not the bank, am most grateful. Anne Goodgame has also played a vital rôle since I arrived as a Part II student way back in 1999, providing an attentive ear for discussions on rowing, science and the quality of the Alternative Tuck Shop cakes. Since leaving Oxford she has always been on the end of email or a phone to haul me back into reality when things were going badly. Adam and Gareth also join this short helpers "hit parade" for tolerating weeks of tinkering

with the chamber with no apparent progress. I am sure my accurate renditions of *Dire Straits* hits impressed them as much as my terrible sense of humour. I wish both of them success in their own doctoral ambitions and hope that I taught them well. In the last year Martin has proved a handy reference point for all things maths and physics. I apologise for nagging him about simple things; it seems my brain is failing of late! Last but not least Helen Cruse, a past group member, deserves inclusion in this roll of honour. I had the pleasure of sharing a lab with her when I started out. I could always guarantee that she was in if I had weekend work to do and that she would provide constant updates when the cricket was on. I only hope that I was as easy to work with as she was.

Outside the Softley group I would like to express my gratitude to Rob Jacobs. His knowledge and assistance in the preparation and characterisation of the surfaces is most appreciated. Thanks must also go to the workshop staff without whom very little would ever have been done. Their ability to decipher sketches on the back of envelopes was most impressive and their patience, even when I went back for the third and fourth revision, seemed endless. John and Merv have also made my time in the department an enjoyable one; I often wonder where I will experience such a high level of service, or indeed where I will spend thirty minutes getting a single pen! More recently the tireless efforts of Andy White deserve mention whether it be dealing with exploding pumps or trying to kill the alien invasion in our water system.

All the people above have had a great influence on my work over the past few years but I cannot finish without mentioning the diverse range of people for whom a Rydberg state means nothing (if only they knew what they were missing out on!), but who were more than instrumental in making my time in Oxford enjoyable. It's hard to know where to start and so as not to forget anyone I won't name them - you know who you are. So to all those I have lived with, rowed with or shared a drink with, I will forever remember the fun we had. Your support over the years has been invaluable and you can all claim a little bit in making this thesis happen.

Finally I would like to thank my family. Without them I would never have been in a position to begin, let alone finish my D. Phil.. Their support, both financially and emotionally, is seemingly unending and I am sure that in my parents life plan, having their son move back home at the age of 27 was not considered. I hope I haven't been too much of a burden!

TABLE OF CONTENTS

List of Figures

List of Tables

What is a scientist after all?
It is a curious man looking through
a keyhole, the keyhole of nature,
trying to know what's going on.

JACQUES COUSTEAU

CHAPTER

ONE

Introduction

The interaction of particles (atoms, molecules and ions) and solid surfaces is of considerable interest both theoretically and experimentally. The interactions play a fundamental rôle in various applied fields such as heterogeneous catalysis, material processing and astrophysics. Additionally the scattering of ions on surfaces is frequently used to probe the composition of surfaces and to determine both surface structure and the location of adsorbates. Previous experimental work, however, has focused on the interaction of atoms, ions and ground state molecules with surfaces. This thesis describes a novel experiment to study the interaction between electronically excited molecules, in this case molecular hydrogen, and metallic surfaces. Molecular Rydberg states are ideal candidates for such an investigation due to their large physical size, and the resulting weak binding of the outermost electron, which makes them particularly sensitive to the electric fields present at the metal-vacuum interface. In the work presented here, charge transfer between hydrogen Rydberg molecules and metals has been observed for the first time and the results are presented in Chapter 4.

The following sections serve as an introduction to the topic of charge transfer at surfaces together with a detailed review of the particular properties of high-n Rydberg states that were utilised in this work.

1.1 Charge transfer at surfaces

The interaction of an atom, ion or molecule with a surface is usually accompanied by inelastic processes and in the majority of cases these are manifested as charge

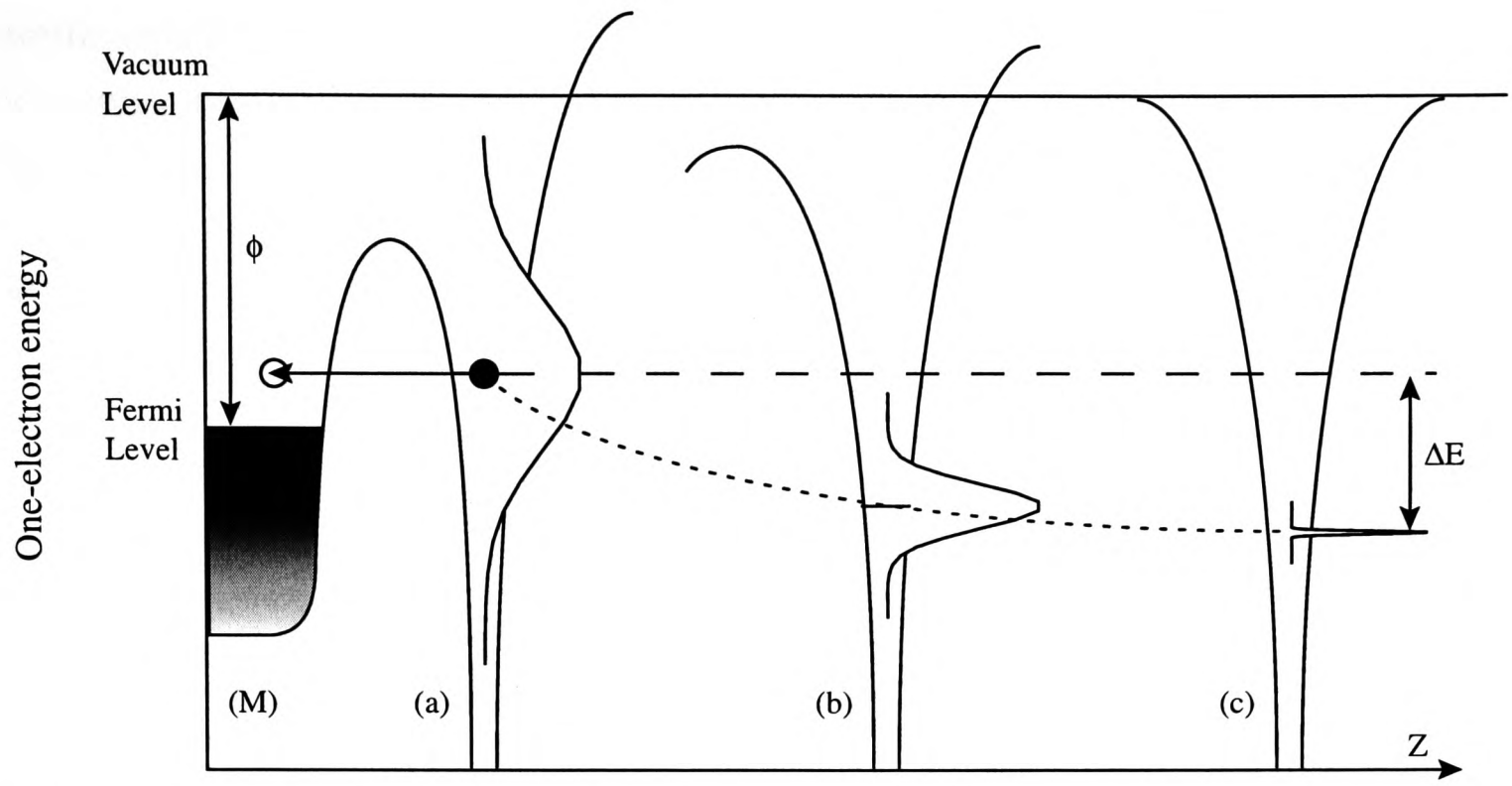

Figure 1.1: *One-electron energy level diagram illustrating the perturbation of the Rydberg electron level as the atom approaches the surface. Z is the separation between the atom/molecule core and the metal surface while ϕ is the work function of the metal. The dotted line represents the change in the energy of the state as the surface is approached assuming it has no width - that is the midpoint of the energy profile.*

exchange between the incident projectile and the surface. The charge transfer mechanisms were first summarised in the 1950s by Hagstrum [1] who successfully used this phenomenon, originally reported by Oliphant [2], to develop ion neutralization spectroscopy (INS) [3]. Other applications include a detection system used in atomic clocks which relies on the ionisation of ^{133}Cs beams at surfaces [4], and surface profiling using high energy ion beams in secondary ion mass spectrometry (SIMS) [5, 6]. More recently the applications of ion-surface scattering for the generation of H^- ions used in fusion plasmas has increased interest [7]. A general review of the charge transfer processes occurring in atom and ion beam scattering at surfaces is presented by Los and Geerlings [8].

In the investigations which follow it is feasible that ionisation of the outermost electron may occur via a process of resonant electron tunnelling whereby the electron tunnels through the potential barrier and occupies a vacant level in the metal. The one-electron energy-level diagram shown in Figure 1.1 illustrates a simplistic representation of the energetics involved in the transfer of the electron from an atom to a metal surface. The vacuum level indicates the zero energy level for completely removing an electron from the atom. The far right side of the diagram, (c), represents the energy level of the state when the ionic core is located at an infinite distance from the surface. The left hand side of the diagram, (M),

represents the occupied electronic states of the metal surface, where the difference in energy between the Fermi level and the vacuum level is the work function of the metal, ϕ.

The probability of ionisation is dictated by the degree of overlap between the atomic and metallic wavefunctions. When the atom/molecule core is located at a great distance from the surface (large Z, (c)) there is minimal overlap and as such the probability of ionisation is very low. The atomic energy levels are essentially discrete. However, as the core approaches the surface (Z decreases, (b)) the probability of ionisation increases as the barrier lowers and its width narrows. Transfer of the electron into the empty conduction band of the metal by electron tunnelling ((a)+(M)) is now more facile. Consequently the lifetime of the levels becomes finite and, in accord with Heisenberg's uncertainty principle, there is a width associated with each level. The smaller core-surface separation also leads to an increased interaction between the valence electron and the delocalised charges in the metal. The effect of this interaction is to raise the energy of the atomic levels. As such the overall result of approaching the surface is both a broadening of levels and an energy shift.

1.1.1 Previous investigations involving atomic Rydberg states

One area that has received particular attention involves the interaction of Rydberg atoms with surfaces. Rydberg states are ideal candidates for investigations of charge transfer phenomena due to the weak binding of the outermost electron which is manifested in high sensitivity to electric field effects. Studies have focused on the determination of the atom/surface separation at which ionisation occurs. The first experimental estimate of the atom/surface separation required for ionisation to occur was obtained by Fabre *et al* [9] in 1983. They performed experiments where a beam of sodium Rydberg atoms passed through a metallic (gold) grating made up of an array of micrometre slits. More recently similar experiments, by Kocher and co-workers [10, 11], using lithium Rydberg atoms and mesh grids have suggested that the previous estimates for the atom/surface ionisation distance may be incorrect due to the effect of surface deposition. It was found that the survival probability of the Rydberg states was greatly dependent upon the degree of sub-monolayer accumulations. The absorbed species can produce localised fields which lead to perturbations and ionisation. Other investigations using alkali atoms have been performed, and, most notably, the work of Dunning *et al* [12] was the first to investigate the interaction of an atomic

Rydberg beam (potassium atoms) at a near-grazing incidence with a solid target surface. However, all of these approaches suffer from the problem of alkali metal deposition on the surface.

Once again it was the work of Dunning *et al* that successfully addressed this issue. In order to provide a more controlled surface environment they repeated their earlier experiments using xenon Rydberg atoms under ultra-high-vacuum (UHV) conditions [13]. They used an Au(111) mirror as a target surface and efficient surface ionisation was observed. A field was applied such that any ions formed at the surface were pulled away towards a detector. The closer the ionisation occurred relative to the surface, the greater the field required to detect the ions. It was found that the atom/surface separation at which ionisation occurred scaled approximately with the atomic radius of the Rydberg state. In fact, in the range of quantum numbers investigated, $(13 \leq n \leq 20)$, ionisation was found to occur at a separation $Z_i = (4.5 \pm 0.9)\, n^2 a_0$. This is of comparable magnitude to the theoretically determined value, $Z_i \sim 3.8 n^2 a_0$, calculated using *ab initio* hydrogenic theory [14]. They also noted that if the states were populated in a field the position of ionisation had little or no dependence on the electron density distribution of the state initially populated (see Section 1.4 for a more detailed discussion of the effect of electric fields on Rydberg energy levels). This was explained by Zhou *et al* [15] by assuming that the states pass through energy level crossings adiabatically as the surface is approached. Consequently the exact character of the state, whether initially blue or red shifted in the field, becomes scrambled prior to ionisation. The behaviour of Rydberg states in the presence of a field is discussed later in Section 1.4.

1.1.2 Molecular interactions

The extension of these experimental investigations to *molecular* Rydberg states introduces to the system the possibility that internal couplings between the bound states and the ionisation continua may exist. Such couplings may be mediated due to the presence of charges in the surface and their associated fields. These charges arise in response to the location of the ion core and electron outside the surface and as such are termed "image charges" (see Chapter 2 for further discussion). The molecular ion core (H_2^+ in the work presented here) possesses vibrational and rotational degrees of freedom and their presence may lead to processes which are facilitated by channel interactions, such as predissociation or auto-ionisation (see Section 1.3.3), to occur competitively with the tunnelling

ionisation at the surface. There is also a greater chemical interest in using species other than rare gas or alkali metal atoms for these studies, in that the products of tunnelling ionisation (H_2^+) or dissociation (H atoms) could potentially become involved in secondary chemical processes at the surface. It is also feasible that reaction could be induced between the incident molecule and adsorbates on the surface. For example such a reaction could proceed via the transfer of the Rydberg electronic energy into the breaking of a chemical bond, followed by secondary reaction with the incident molecule.

1.2 Molecular Rydberg states

A Rydberg state can be described as a state in which one (or more) valence electron(s) has been excited into a hydrogenic orbital of high principal number, n, such that the average separation between the core and the electron is high. The properties of these Rydberg states are unusual compared to their ground state counterparts and stem from the almost macroscopic dimensions of the orbital radius. The property that has most relevance to the work in this thesis is the high susceptibility of the Rydberg electron to the presence of external electric fields.

1.2.1 A brief history of Rydberg spectroscopy

Although Rydberg[1] did not collect any experimental data himself, he had available to him several spectral lines of hydrogen (now know as the Balmer series) and data for the alkali metals, all of which lay well within the visible spectrum. The hydrogen lines had been identified in 1885, by Johann Balmer, as being well-characterised by the formula $\lambda \propto n^2/\left(n^2-2^2\right)$ [17], but Rydberg was unaware of this when his study began. Using his extended data set he was able to generalize Balmer's form of the transition frequency and the, now familiar, result is shown in Equation 1.1. His results and workings were published in 1889 [18].

$$\frac{n}{N_0} = \frac{1}{(m_1+c_1)^2} - \frac{1}{(m_2-c_2)^2}. \qquad 1.1$$

The names of the variables are presented using Rydberg's original choice of symbols: n is the wavenumber of the emitted light, N_0 (again in wavenumbers) is the constant now known as the Rydberg constant and m_1 and m_2 are positive integers.

[1] As an aside, for an interesting discussion of Rydberg's life and work see [16].

The additional constants c_i are the only modification necessary to extend the hydrogenic formula to the analysis of alkali spectra. While initially believed to be purely experimentally determined constants, it was later found that the constants c_i do have a meaning in theoretical approaches to the problem (see Section 1.2.3).

With sufficiently accurate spectroscopic methods, deviations from the general formula above began to emerge, reflecting a variety of perturbative effects that would be difficult to detect using ground state systems. However the separation between the lines of a hydrogenic energy spectrum diminishes rapidly with increasing principal quantum number, n, as $1/n^3$. Consequently the difference between the energy levels with $n = 99$ and $n = 100$ is already less than 1 cm^{-1}. Selective excitation of a particular state in the presence of a small external field demands even greater control over the energy and linewidth of the incident light due to the lifting of the degeneracy of states with identical principal quantum number, n, but different angular momentum quantum number, l. The extraction of detailed structure within the Rydberg spectrum, and subsequent investigations whereby a particular state is selectively populated, has therefore been dependent upon advances in the efficiency with which light can be produced at both high intensity and narrow bandwidth. A further complication arises from the necessity of working under vacuum conditions due to the absorption of radiation by background gas particles in the ultraviolet [19], where transitions to Rydberg states of atoms and small molecules are most commonly observed.

It is therefore understandable that high-resolution Rydberg spectroscopy (of the order of ΔE <1 cm^{-1}) was not practical until the 1970s. The earliest high-resolution discrete absorption spectrum of molecular hydrogen was that conducted by Herzberg [20], and the first continuum spectrum was that of Dehmer and Chupka [21].

Further improvement in experimental procedure and equipment has continued and examples include the use of high-intensity synchrotron radiation sources and the introduction of narrow bandwidth laser sources extending far into the ultraviolet through the use of tunable lasers, frequency doubling and efficient higher harmonic generation (see for example [22]).

As such state-selective population of Rydberg atoms and molecules is feasible with a high level of control. This fact, coupled with the physical properties of the Rydberg states, discussed below, make them ideal candidates for the study of many chemical and physical phenomena. For a survey of their possible applications see the reviews [23] and [24].

1.2.2 The classical picture

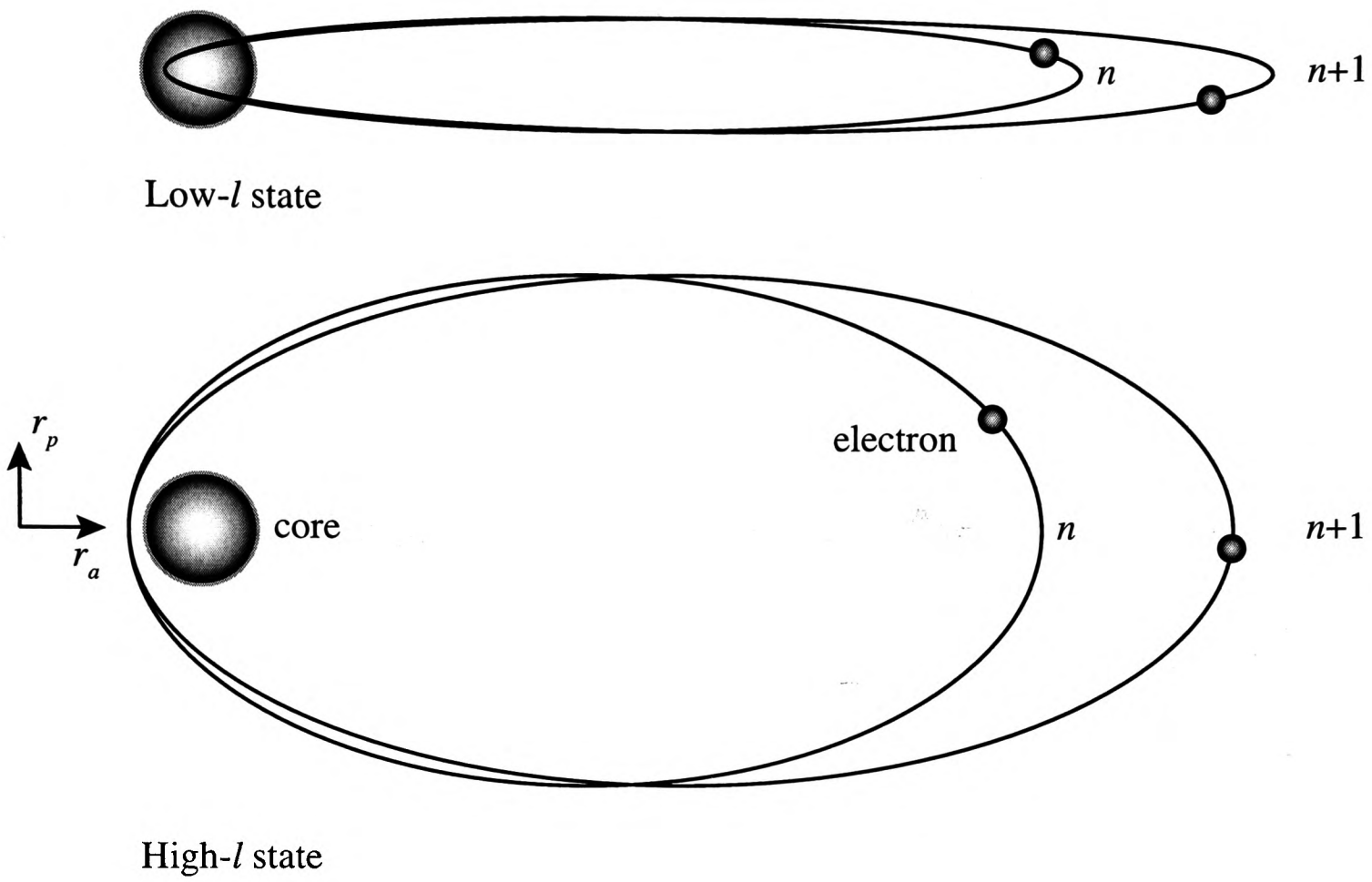

Figure 1.2: *The classical picture of a Rydberg orbit and its dependence on the electron quantum numbers, n and l. The penetration of the core exhibited by the low-l states is also depicted. The coordinates r_a and r_p are also shown.*

In the classical model a molecular Rydberg state can be described as an electron orbiting a molecular core where the orbital has sufficiently large mean radius that for the majority of a single orbit the electron experiences only the electrostatic potential due to a single positive point charge which represents the ionic core. As such it experiences the same potential as if it were in a hydrogen atom. The path of this elliptical orbit, first proposed by Sommerfeld [25], which has the ion core at one focus, can be characterised by both the principal quantum number, n, and the orbital angular momentum, l, of the Rydberg electron. The perihelion, r_p, is proportional to $\left(l+\frac{1}{2}\right)^2$ and the aphelion, r_a, proportional to n^2. The difference between low-l and high-l orbits and the effect on the orbit of populating a state of higher principal quantum number is shown in Figure 1.2. These properties will be discussed further when considering the molecular Rydberg energy levels.

It is evident that the aphelion will increase rapidly with the principal quantum number and this is just one of many physical properties of Rydberg states that varies dramatically as the value of n is increased. Much of the behaviour that makes Rydberg states so fascinating is due to the scaling of these physi-

property	scaling factor
radius r_a	n^2
binding energy	n^{-2}
degeneracy	n^2
orbital period	n^3
radiative lifetime	n^3
energy between adjacent n states	n^{-3}
polarisability	n^7

Table 1.1: *Properties of Rydberg states which scale with the principal quantum number, n.*

cal properties with the electron principal quantum number, and it is this which forms the basis for the growing number of applications of Rydberg states in experimental chemical physics including the preparation of state selected ions [26], studies of ion molecule reactions [27] and, more recently, translational control of atoms [28, 29, 30] and the preparation and study of cold molecules [31, 32]. These physical properties are dependent on the electron probability distribution and consequently the functional form of the radial wavefunction $R_{nl}(r)$. However, although it may seem too much of a simplification to use the classical Bohr model of the hydrogen atom [33] to determine the scaling of physical properties that are dependent on the quantum mechanical wavefunctions, previous experiments have found the classical model to provide accurate prediction of observed behaviour (see for example [34, 35]). A summary of some of the properties of Rydberg states that scale as a function of the principal quantum number, n, is given in Table 1.1. It is of interest to note that even for a Rydberg state with principal quantum number $n = 17$ the diameter, $2r_a$, of the Rydberg electron orbit is equal to 30.5 nm. It is this near macroscopic proportion that leads to Rydberg states exhibiting high sensitivity to effects such as electromagnetic fields and which make them ideal candidates for the investigations presented here.

It is also prudent to realise that there are many further properties of Rydberg states, chiefly associated with excitation and decay, that are dependent upon the electron-core interaction and not solely the expanse of the Rydberg electron orbit. The classical model does not accurately describe the region where the electron penetrates the core and as such these properties cannot be directly scaled as above. However, as a first approximation, the probability of processes such as radiative decay can be associated with the proportion of time spent in the core region, that is the inverse of the Bohr frequency, and hence scale as n^3.

1.2.3 Rydberg series

In the case of the hydrogenic Rydberg states the solution to the Schrödinger equation leads to the well-known result

$$E_n = -\frac{\Re_M}{n^2} \tag{1.2}$$

where $\Re_M$ is the Rydberg constant. This constant is dependent upon the reduced mass of the system. In the case of atomic hydrogen it takes the value $\Re_H = 109667\,\mathrm{cm}^{-1}$. Evidently the energy is dependent solely on the principal quantum number, n, and the states form a series that converges to the ionisation threshold as $n \to \infty$.

In non-hydrogenic systems such as many-electron atoms, where the potential experienced by the Rydberg electron is not purely Coulombic, the degeneracy of states with the same principal quantum number, n, but different angular momentum quantum number, l, is lifted. This arises as the degree of penetration of the electronic wavefunction in the core region decreases rapidly with increasing l as the centrifugal barrier, given by $l\,(l+1)\,/2r^2$, rises rapidly. The classical depiction of this effect is shown in Figure 1.2. As a result the electron is exposed to an increased core charge as l decreases, relative to higher-l states, and only higher l states behave in a predominantly hydrogenic way. This modified behaviour gives rise to an l-dependent quantum defect, δ_l, which although originally thought of as an experimentally determined parameter [18] does have a basis in quantum mechanical analysis [36]. It represents a phase-shift in the radial component of the total wavefunction of the Rydberg electron such that the wavefunction more accurately describes the electron probability distribution in the core region, that is at small r. This is illustrated below in Figure 1.3.

Typically the quantum defect is larger for lower l values, scaling as l^{-5} [37] and can be assumed to effectively vanish for non-penetrating high-l states ($l \geq 4$). Due to the lifting of the degeneracy of states of identical n but different l there are now several Rydberg series which converge to a given ionisation threshold. The energy of a state in these series is given by the Rydberg formula [18] presented in its more familiar form

$$E_{nl} = -\frac{\Re_M}{(n-\delta_l)^2}. \tag{1.3}$$

In the case of molecular Rydberg states the motion of the core must also be taken into account. If one treats the Rydberg state as a Rydberg electron moving independently of the ionic core then, as previously, the electron motion can be

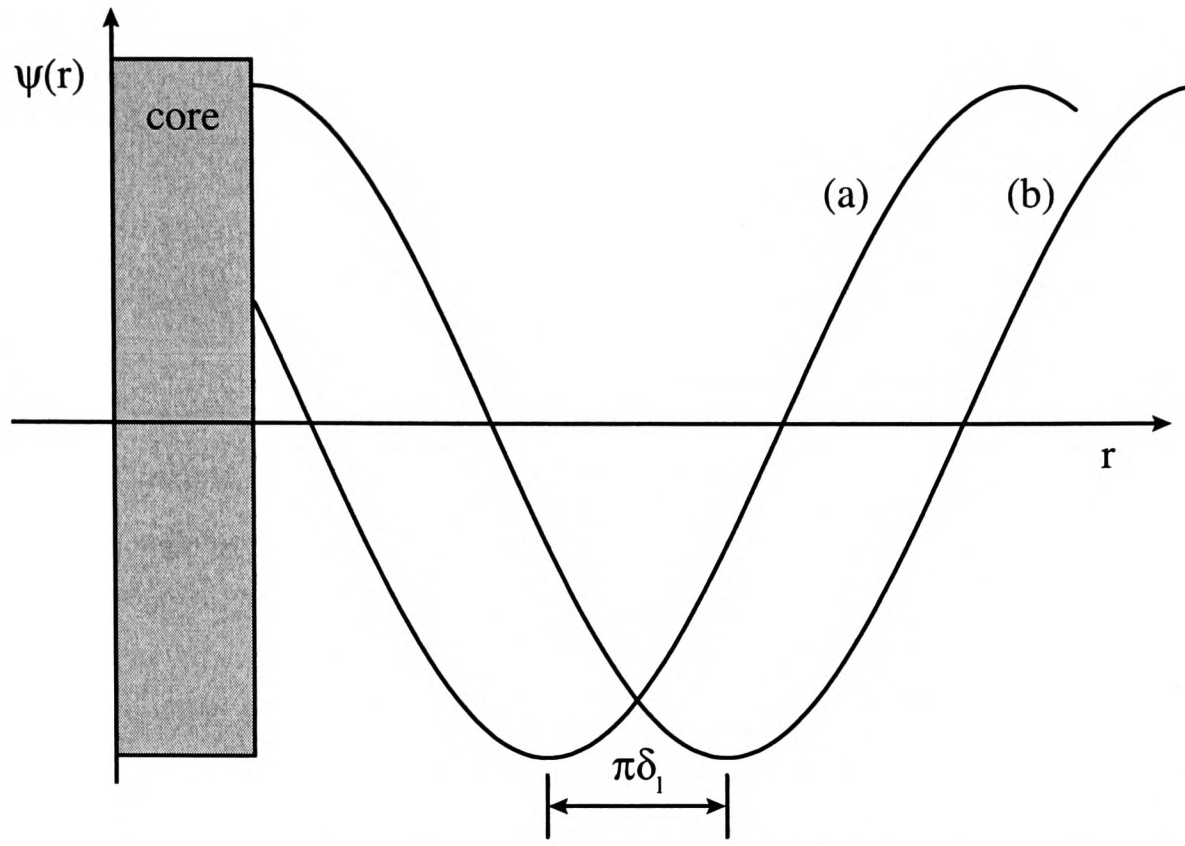

Figure 1.3: *Illustration of the quantum defect, δ_l, associated with the phase shift of the hydrogenic wavefunction (b) such that it more accurately describes the true wavefunction (a) in the core region.*

characterised by the hydrogenic quantum numbers n and l. The ionic core is also considered to vibrate and rotate independently of the Rydberg electron motion and can be characterised by the rotational and vibrational quantum numbers N^+ and v^+. The energy of the Rydberg state, in the absence of perturbations between states with different core or angular momenta, is now calculated as the sum of two terms

$$E_{N^+v^+;n,l} = IP\left(N^+v^+\right) - \frac{\Re_M}{(n-\delta_l)^2} \qquad 1.4$$

where $IP\left(N^+v^+\right)$ is the energy associated with the threshold for ionisation from the ground state of the molecule to an ion with specific rotational and vibrational character. As a result several series converging to different ionisation thresholds exist, dependent upon the rovibrational quantum numbers of the core. Each series contains Rydberg states where the principal quantum number of the Rydberg electron changes but which share identical core and electron angular momentum quantum numbers. Several such series converging to ionisation thresholds associated with different core rotational angular momentum quantum numbers, N^+, are shown in Figure 1.4. Each series can now be thought of as forming a channel to a given ionisation threshold and it is possible that interactions between these channels may occur. This phenomenon is discussed in more detail in Section 1.3.3.

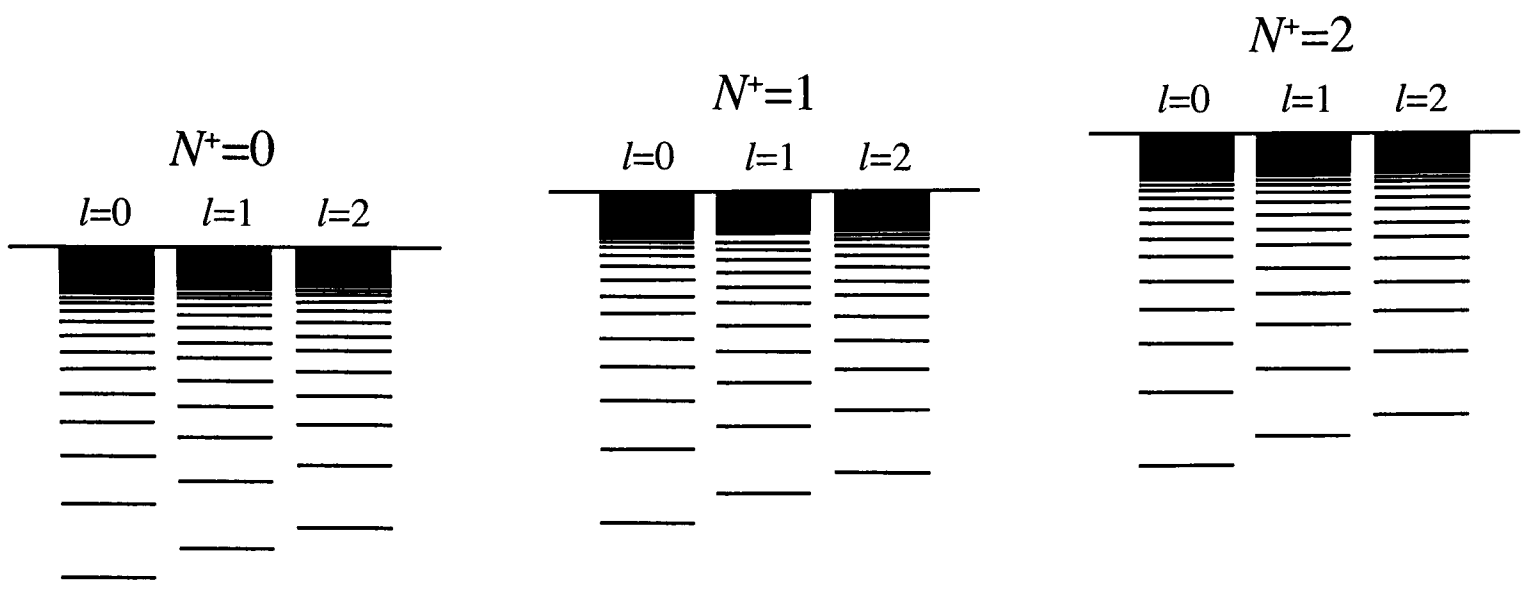

Figure 1.4: *Schematic representation of a number of Rydberg channels, in this case identified by the core rotational quantum number, N^+. Each channel comprises a group of Rydberg series converging to a single ionisation threshold.*

1.2.4 Rydberg energy levels in diatomic molecules

The description of Rydberg series given above, and encompassed in Equation 1.4, is associated with the limiting case where the ionic core charge distribution is assumed to be isotropic. In reality the coupling between the rotational motion of the core and the electronic angular momentum is sensitive to the excitation of the Rydberg electron. The electron undergoes a gradual transition from the low-n case of being strongly coupled to the internuclear axis to the high-n case where the electronic angular momentum decouples from the symmetry axis and is instead quantized along the ionic core's axis of rotation. This shift in behaviour can be understood by considering the fact that this coupling is facilitated by the electrostatic field of the core charges. Consequently when the Rydberg electron is in close proximity to the core, coupling will be strong. As the principal quantum number increases, so too does the extent of the Rydberg electron orbital. Similarly the proportion of time the Rydberg electron spends in the core region decreases with increasing n and so the strength of the interaction decreases. The limits of these two situations are referred to as Hund's case (b) coupling and Hund's case (d) coupling respectively. For the np states of H_2 it has been reported that this transition from case (b) to case (d) occurs at approximately $n = 9$ [38] while high-l states ($l \geq 3$), with principal quantum number $n \geq 4$, are already well described by case (d) [39]. When considering the coupling of angular momenta in diatomics four different kinds of angular momentum arise. These are the orbital angular momentum of the electrons, **L**, the nuclear rotational angular momentum, **R**, the spin angular momentum of the electrons, **S**, and the nuclear spin, **I**. The last of

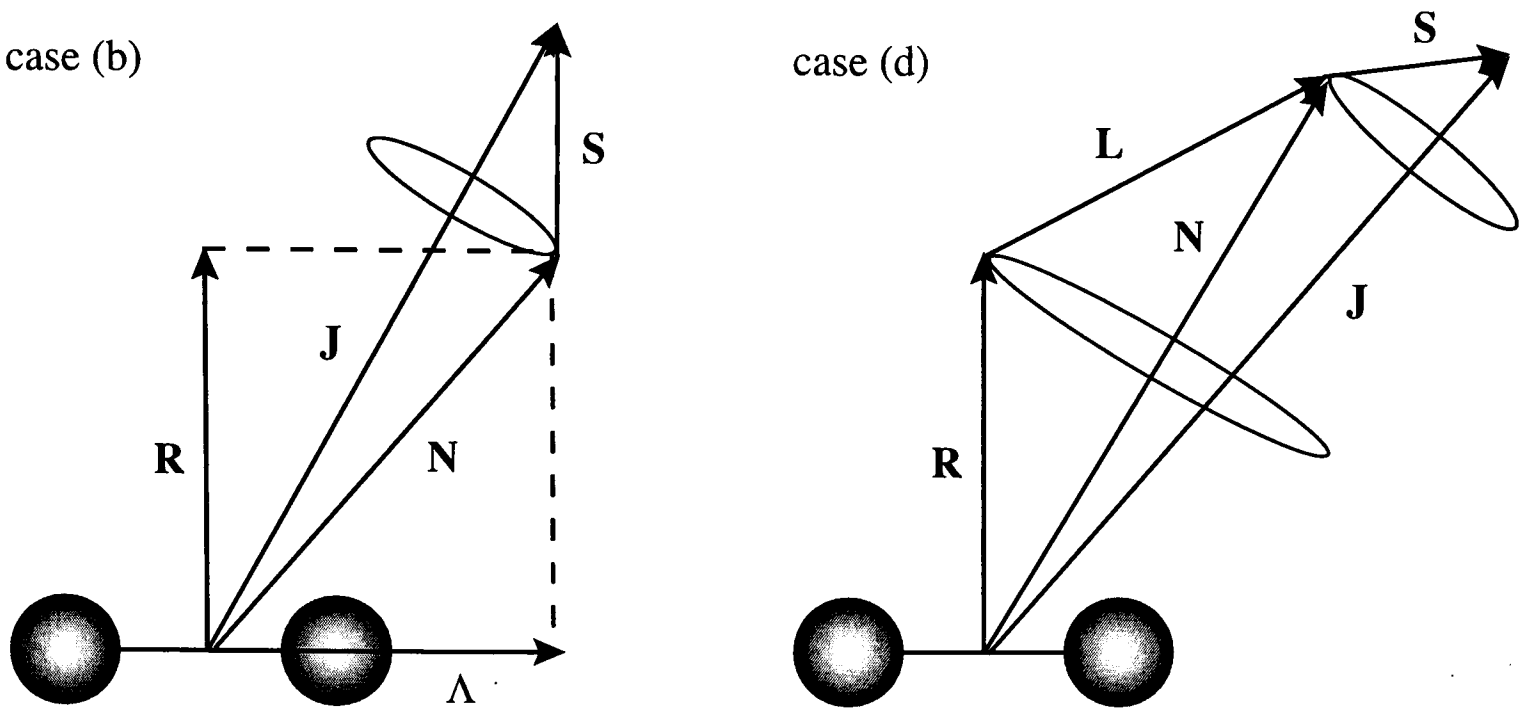

Figure 1.5: *Schematic representations of Hund's case (b) and Hund's case (d) coupling schemes as described in the text.*

these is neglected in the discussion which follows. Coupling of these angular momenta may also give rise to **N**, the total angular momentum vector neglecting the spin of the electrons, and **J**, the total angular momentum vector including spin. Finally the projection of the electron angular momentum along the internuclear axis is labelled **Λ**.

In the case where there is essentially very little interaction between the Rydberg electron and the ion core Hund's case (d) is a sufficient zero-order description of the system. The Rydberg electron orbital angular momentum, **L**, does not couple to the internuclear axis but instead couples directly to the axis of rotation of the molecule, **R**. The angular momentum of nuclear rotation is now quantized and N^+, the core rotation quantum number becomes "good". The angular momentum quantum number, l, of the Rydberg electron remains well defined and, assuming **S** is equal to zero, the total angular momentum quantum number, J, take the values

$$J = N^+ + l, N^+ + l - 1, N^+ + l - 2, \ldots, \left|N^+ - l\right|. \qquad 1.5$$

The Rydberg states form series that converge at distinct ionisation limits and are labelled $(nlN^+)_J$ as is essentially the case in the preceding section and Figure 1.4.

In Hund's case (b), the projection of the orbital angular momentum along the internuclear axis, **Λ**, is strongly coupled to the angular momentum of nuclear rotation, **R**, to give **N**. This in turn couples to the spin angular momentum, **S**, which is zero for the singlet states considered in this work, to give **J**. A quantum num-

ber, Λ, may be defined where $\Lambda = \lambda_{core} + \lambda$. (In the case of Rydberg states λ, the projection of the Rydberg electron orbital angular momentum, is well defined). In the present case, of hydrogen Rydberg molecules, $\lambda_{core} = 0$ and so $\Lambda = \lambda$. The molecular states are then labelled with the usual molecular term symbols, where the symbols Σ, Π and Δ represent $\Lambda = 0, 1$ and 2 respectively. For example, states arising from an *nd* electron are labelled $^1\Sigma_g^+$, $^1\Pi_g$ and $^1\Delta_g$. As in Hund's case (d) each state, $|nl\lambda\rangle$ also has associated rotational levels corresponding to the different values of the total angular momentum quantum number J. These two distinct cases are summarised in Figure 1.5.

In the range $n = 6 - 10$ the coupling is mixed and it is likely that neither case gives an adequate description of the situation.

1.3 Lifetimes of Rydberg molecules

Implicit in the fact that Rydberg states are generated by the excitation of one electron into a higher energy orbital is that they are unstable with respect to decay to a lower energy state. In the case of atoms this decay is governed primarily by radiative processes, namely black-body radiation stimulated transitions and spontaneous emission, while for molecules, alternative, non-radiative processes exist such as predissociation. In order to perform experiments with these species it is essential that they are stable during the course of the experiment with respect to these decay processes. This is especially important in the collisional surface experiments detailed later as the Rydberg states must survive for $10 - 15$ μs in order to reach the surface.

1.3.1 Spontaneous emission

A Rydberg state may emit a photon of energy $\hbar\omega$ corresponding to the electron spontaneously decaying to a state of lower energy. The overall decay rate of a state $|nl\rangle$ decaying to a lower lying state $|n'l'\rangle$ is given by

$$\Gamma_{nl} = \sum_{n'l'} A_{nl,n'l'} \tag{1.6}$$

where $A_{nl,n'l'}$ is the Einstein coefficient [40]

$$A_{nl,n'l'} = \frac{\omega_{nl,n'l'}^3 e^2}{3c^3 \pi h \varepsilon_0} \left| \langle nl \left| r \right| n'l' \rangle \right|^2 \tag{1.7}$$

which represents the probability of a spontaneous transition occurring. In the classical picture spontaneous emission can only occur when a charge is under an accelerating force. This occurs in the ion-core region of Rydberg states leading to a radiative lifetime which scales as n^3. This is reflected in the quantum mechanical approach (Equations 1.6 and 1.7) as the main contribution to the integral $|\langle nl\,|r|\,n'l'\rangle|^2$ is from the wavefunction in the core region and it is found experimentally that lifetimes do indeed scale as n^3.

Constraints imposed by the angular momentum and symmetry selection rules require the transitions to be of the form $\Delta l = \pm 1$ and the presence of the ω^3 term in Equation 1.7 suggests that the highest frequency transitions dominate the decay process. Consequently, in all but the case of $l = 0$, the major decay path will be to the lowest lying n', $l' = l - 1$ level. The frequency of these transitions decreases with increasing l and hence the stability of the Rydberg states with respect to spontaneous emission increases with increasing l.

1.3.2 Black body radiation induced decay

Two properties of the energy levels of Rydberg atoms and molecules make them particularly susceptible to transitions induced by black body radiation, even at room temperature. Firstly, as the principal quantum number is increased so the energy spacings between adjacent levels, ΔE, decrease and can be sufficiently small at room temperature that $\Delta E < kT$. Secondly, the transitions between Rydberg levels are characterised by large dipole matrix elements, resulting in excellent coupling between the Rydberg states and the thermal radiation. This results in rapid population redistribution and enhanced radiative decay rates for Rydberg systems, both of which are observed experimentally [41, 42, 43].

Quantitatively the rate of stimulated absorption or emission by the black-body radiation is given in atomic units by

$$\Gamma_{nl,n'l'} = \sum_{n'l'} \bar{n} A_{nl,n'l'} = \sum_{n'l'} \frac{-2\bar{n}e^2\omega^2_{nl,n'l'}}{hc^3} \bar{f}_{nl,n'l'} \qquad 1.8$$

where $\bar{f}$ is the m-independent oscillator strength, $A_{nl,n'l'}$ is the Einstein coefficient given by Equation 1.7 and $\bar{n}$ is the number of photons per mode of the radiation field [40]. This is derived from Planck's radiation law [44] for energy density and takes the form

$$\bar{n} = \frac{1}{e^{h\nu/kT} - 1}. \qquad 1.9$$

The addition of the $\bar{n}$ term to the rate equation results in a marked difference between the frequency dependence of black-body radiation-induced transitions compared with spontaneous emission. While spontaneous emission depends solely on the Einstein A coefficient, resulting in high frequency transitions to low lying states, black body radiation stimulated transitions are characterised by transitions to nearby states. For such a transition $\omega < kT$, the limit of which gives $\bar{n} = \frac{kT}{\omega}$. Substituting this term back into Equation 1.8 leads to the expression

$$\Gamma_{nl,n'l'} = \sum_{n'l'} \frac{-2e^2 kT\omega_{nl,n'l'}}{hc^3} \bar{f}_{nl,n'l'}. \tag{1.10}$$

Summation over n' implicitly includes the continuum of states and in the case of a one-electron atom, using the sum rule [45]

$$\sum \omega_{nl,n'l'} \bar{f}_{nl,n'l'} = \frac{2}{3n^2}. \tag{1.11}$$

So for a one-electron atom the rate of black-body radiation induced decay is dependent only upon the principal quantum number, n, and exhibits no l dependence. This is in marked contrast to the rate of spontaneous emission which decreases with increasing l. Consequently the lifetime of high-l states is dominated by black-body processes. Also apparent from Equation 1.11 is the n^2 scaling of black-body lifetimes. If one compares this to the scaling of spontaneous emission lifetimes, n^3, it is clear that at sufficiently high-n black-body processes will dominate, even for low-l states.

1.3.3 Non-radiative decay

Molecular Rydberg systems can also exhibit decay processes which proceed via a non-radiative pathway. Such mechanisms include predissociation and autoionisation. Of most importance in the experimental work presented later is autoionisation although predissociation is important in terms of molecule lifetimes. These alternative pathways arise due to the ability of individual Rydberg channels to interact.

Channel interactions

As mentioned in Section 1.2.3 a Rydberg channel is specified by a unique set of core quantum numbers and the angular momentum of the Rydberg electron. Associated with each channel is a Rydberg series converging to the ionisation

threshold determined by the energy of the free ion. Although the Rydberg electron and ion-core may be considered independent it is more accurate to consider the Rydberg states as a multi-channel problem where couplings exist between different series; so-called channel interactions. Such inter-series couplings may be viewed in a time-dependent manner as the scattering of the electron from the core during the course of the electron orbit. If this collision is inelastic then energy exchange may occur and the out going electron will have an orbit characteristic of a different channel. From a time-independent perspective the Rydberg series exhibit mixed-channel character. These interactions arise when the electron experiences a non-centrosymmetric potential in the core region. Such a potential can be attributed to configuration interaction or the presence of various multipole moments of the ion core. The effects of channel interactions are most often seen experimentally as intensity perturbations in spectra (see for example [46]).

Autoionisation

The emission of an electron that occurs when a Rydberg state, with an energy higher than that of the lowest ionisation threshold, interacts with an ionisation continuum of a different channel, is termed autoionisation and is shown schematically for rotational autoionisation in Figure 1.6(a).

This process can be regarded as an inelastic collision between the Rydberg electron and the ion core resulting in the transfer of energy from the electronically excited ion core to the Rydberg electron which is subsequently ejected with excess

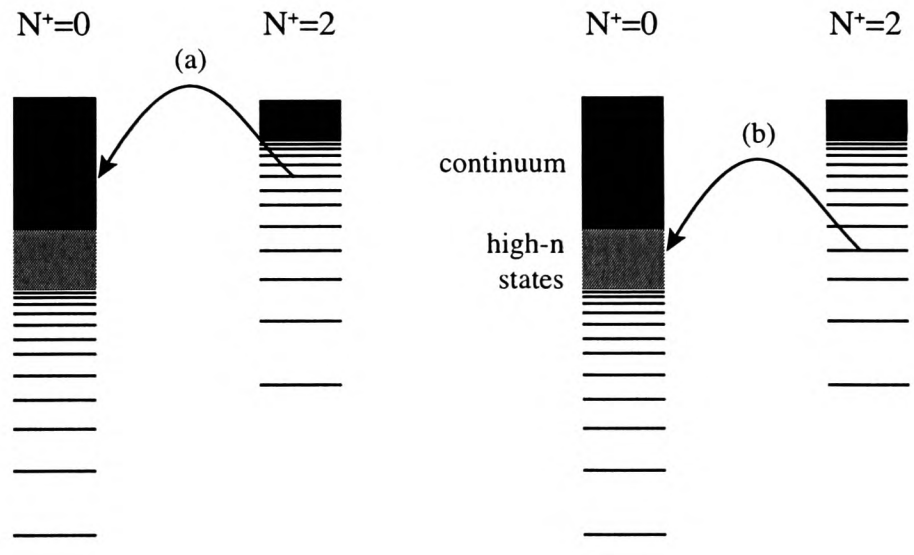

Figure 1.6: *Schematic representation of two non-radiative decay mechanisms facilitated by rotational channel interactions. (a) depicts autoionisation from a bound state into a continuum whereas (b) depicts pseudo-autoionisation from a bound state into a continuum arising due to the presence of a field.*

kinetic energy. In atomic systems the Rydberg electron can gain energy from the excited Rydberg core by the conversion of core electronic or spin-orbit energy (see for example [47]). In molecules, rotational and vibrational energy transfer may also occur. An example mechanism for rotational autoionisation is

$$\left|v^+ = 0, N^+ = 2, n\right\rangle \xrightarrow{\textit{rotational autoionisation}} \left|v^+ = 0, N^+ = 0\right\rangle + e^-. \qquad 1.12$$

The fact that autoionisation takes place is a consequence of the breakdown of the Born-Oppenheimer approximation, a result of which is that interactions between the electron and the core can occur [48]. Penetrating, low-l states are expected to undergo autoionisation most readily although high-l states may also autoionise. Similarly the lifetimes are expected to scale as n^3 as the time the electron spends in the core region is inversely proportional to the orbital period.

A comparable mechanism, variously described as field-induced or pseudo-autoionisation, may occur if the Rydberg state is coupled to high-n Rydberg states of another channel which themselves are sensitive to field ionisation. In the presence of an electric field it is feasible for these to become part of a real continuum at which point the coupled Rydberg state may undergo autoionisation. This is of particular importance in the experimental work detailed later (see Section 4.2.2) and is shown schematically in Figure 1.6(b).

Predissociation

While autoionisation is facilitated by energy transfer from the core to the electron, molecules may also undergo a transfer of energy from the Rydberg electron to the molecular core. This process of intramolecular energy redistribution may result in predissociation of the neutral molecule into electronically excited or ground state neutral fragments. This occurs when the Rydberg potential energy curve is crossed by a dissociative, often doubly excited, valence state as in Figure 1.7.

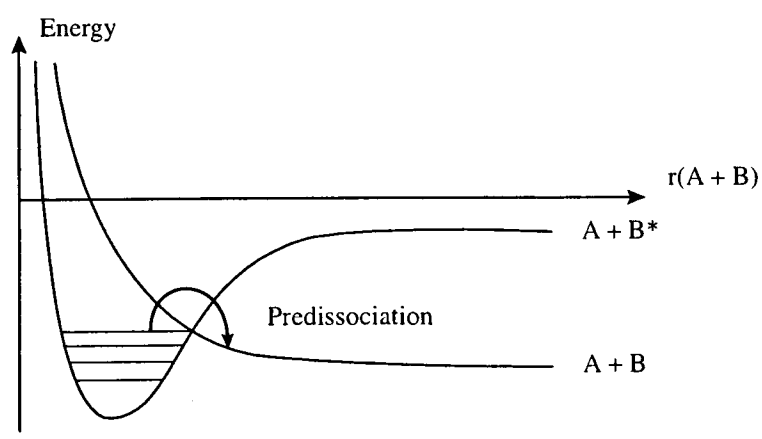

Figure 1.7: *Illustration of the predissociation mechanism.*

1.4 Rydberg molecules in electric fields

The properties of Rydberg molecules that are most useful in the experimental investigations presented later arise because of the sensitivity of the Rydberg electron to an external electric field. The presence of the field results in strong perturbations of the energy levels and even at low electric field strengths the high degeneracy of the levels is lifted. At higher fields the process of field ionisation occurs. As above, the behaviour of the Rydberg states is best explained by first analysing the hydrogenic case and then explaining the differences that arise in non-hydrogenic systems.

1.4.1 The Stark effect

In general the application of a homogeneous electric field, F, has the effect of partially lifting the n^2 electronic degeneracy of the Rydberg states. The Hamiltonian for an H atom in a homogeneous electric field is given, in polar coordinates, by

$$H = -\frac{1}{2}\nabla^2 - \frac{1}{r} + Fz. \tag{1.13}$$

If one expresses the matrix elements of the Stark Hamiltonian, given above, in the $|nlm\rangle$ basis of the zero field Hamiltonian they take the form

$$\langle n'l'm' \,|Fz|\, nlm\rangle . \tag{1.14}$$

Noting that $z = r\cos\theta$, Equation 1.14 can be separated into radial and angular parts such that

$$\langle n'l'm' \,|Fz|\, nlm\rangle = F \langle n'l' \,|r|\, nl\rangle \langle l'm' \,|\cos\theta|\, lm\rangle . \tag{1.15}$$

The exact form of the spherical harmonic functions [49] leads to the selection rules $\Delta m = 0$, $\Delta l = \pm 1$ and $\Delta n = 0, \pm 1, \pm 2, \ldots$ and the effect of the electric field is to couple states such that $m' = m$ and $l' = l \pm 1$.

The application of the field has the effect of reducing the spherically symmetric potential to a cylindrically symmetric potential about the applied field axis, z. As a consequence the orbital angular momentum $\mathbf{L}$ is no longer conserved but precesses around the field vector as shown in Figure 1.8. This symmetry reduction also means that a more useful approach to solving the Schrödinger equation is one using parabolic coordinates, defined as

$$\xi = r + z, \quad \eta = r - z, \quad \phi = \arctan\left(\frac{y}{x}\right). \tag{1.16}$$

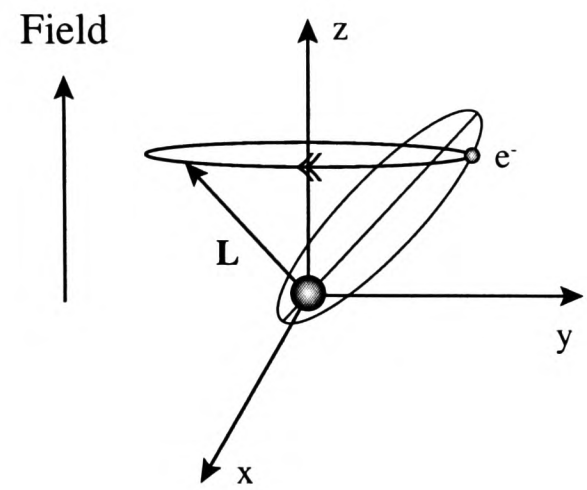

Figure 1.8: *Representation of the orbit of a Rydberg electron in the presence of an external electric field.*

Using such a coordinate system, the Schrödinger equation, in the case of the H atom, remains separable [45] and the wavefunctions are now defined by the quantum numbers n, m, n_1 and n_2 and may be written [44]

$$\Psi(\xi,\eta,\phi) = (2\pi\xi\eta)^{-\frac{1}{2}} f_{n_1 m}(\xi)\, g_{n_2 m}(\eta)\, e^{im\phi} \qquad 1.17$$

where f_{ij} and g_{ij} are the regular and irregular Stark functions respectively. The two new, parabolic quantum numbers, n_1 and n_2, which represent the number of nodes in the separate parts of the wavefunction, are related to n and m by

$$n = n_1 + n_2 + |m| + 1. \qquad 1.18$$

A further quantum number, k, may also be defined such that $k = n_1 - n_2$. For a given n and m, k takes values

$$k = -(n - |m| - 1), \ldots, (n - |m| - 1) \qquad 1.19$$

in steps of two giving a total of $(n - m)$ values of k for each set of zero-field states $|nm\rangle$. In fact k can be seen as a measure of the charge distribution along the field axis. It is found [44] that the highest k state is located with the electron density primarily along the $+z$ axis whilst the electron density of the lowest k state is located along the $-z$ axis. This variation in the Rydberg electron probability distribution manifests itself in the behaviour of the states in a field, most notably in their field ionisation characteristics (see Section 1.4.2).

The Schrödinger equation generated by the Hamiltonian in Equation 1.13 cannot be solved exactly except in the case of the H atom. More generally the energy levels may be calculated approximately using numerical methods which yield a series expansion for the energy of a Stark state in a given field [50]. To the first

order, in atomic units, the energy levels are given by [51]

$$E_{nkm} = -\frac{1}{2n^2} + \frac{3}{2}Fkn. \qquad 1.20$$

For modest field strengths the energy levels are adequately described by this first order approximation and as such the energy of Stark states corresponding to different values of k will exhibit different dependencies upon the external field strength. In fact in this first order approximation the perturbation leads to a linear splitting of the zero-field energy levels, the so-called linear Stark effect. An example of this is given in Figure 1.9 for states with principal quantum number $n = 4$.

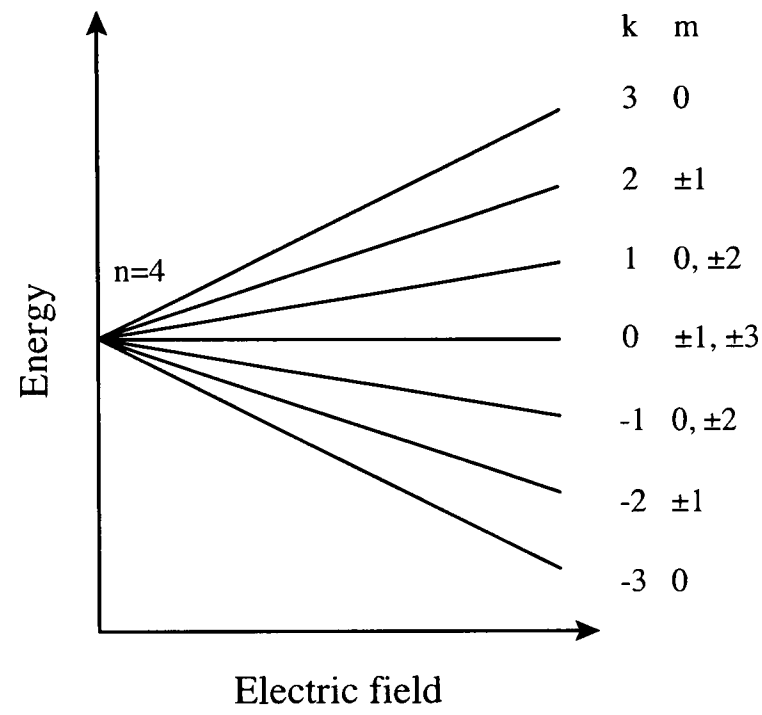

Figure 1.9: *Energy levels of the H atom in an electric field for $n = 4$. Each level is listed with its parabolic quantum number k, together with the degenerate m states.*

If the expansion is continued to include higher order terms as given by [50] then the energy may be calculated thus

$$\begin{aligned} E_{nkm} = & -\frac{1}{2n^2} + \frac{3}{2}Fkn \\ & -\frac{1}{16}n^4[17n^2 - 3k^2 - 9m^2 + 19]F^2 \\ & +\frac{3}{32}n^7k[23n^2 - k^2 + 11m^2 + 39]F^3 + \ldots\ldots \end{aligned} \qquad 1.21$$

At larger fields where these higher order corrections become significant the m degeneracy, which is still large at lower fields, is lifted.

So far the discussion has focused on a single Stark manifold of given principal quantum number, n, and has ignored the presence of other manifolds lying higher

or lower in energy. The situation when the energy of the states of neighbouring manifolds are in close proximity to one another is illustrated in Figure 1.10 where the energies of each member of the manifold is calculated using Equation 1.21. At sufficiently high field strengths the most blue-shifted energy level (highest k) associated with a given principal quantum number, n, crosses the most red-shifted (lowest k) associated with the $n+1$ manifold. This occurs at a field known as the Inglis-Teller field. Referring to Equation 1.20 the crossings occur, in atomic units, at

$$F_{IT} = \frac{1}{3n^5}. \tag{1.22}$$

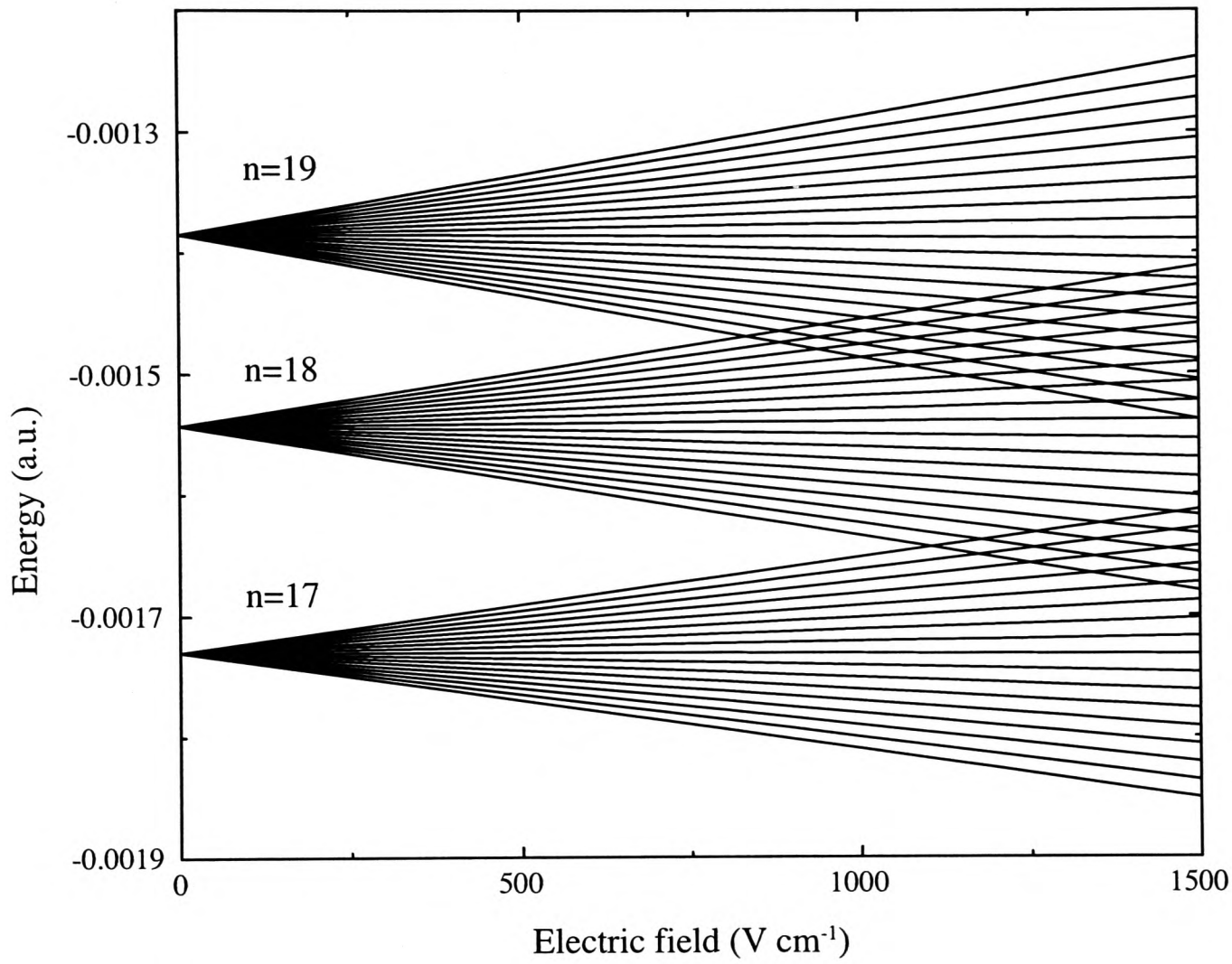

Figure 1.10: *Stark map for a hydrogenic system showing states populated with $n = 17 - 19$ and $m = 0$. The energies are calculated using Equation 1.21 including terms up to the third order.*

It is also worth mentioning that, in the case of the H-atom, this crossing is actually a real crossing with no interaction between the states. Alongside the projection of the orbital angular momentum along the field axis there is a second constant of motion for the H-atom in an electric field, the z-component of the Runge-Lenz vector [44, 52]. It is this additional symmetry, unique to the H-atom, that ensures that the Hamiltonian matrix remains diagonal in the field in

the parabolic basis. This allows the crossing of Stark states with the same m value, belonging to different n manifolds, to occur without any interaction.

1.4.2 Field ionisation

The phenomenon of field ionisation was first observed by Oppenheimer in 1928 [53], and today it is a widely used technique for the detection of Rydberg states [54]. In the presence of an electric field the potential energy of the Rydberg electron in the H atom is modified by the addition of a term, Fz, to the Coulombic potential as in the discussion of the field perturbed Hamiltonian (Equation 1.13). This has the effect of introducing a maximum along the z-axis as illustrated in Figure 1.11. In fact, in the full 3-dimensional potential this maximum represents a saddle point.

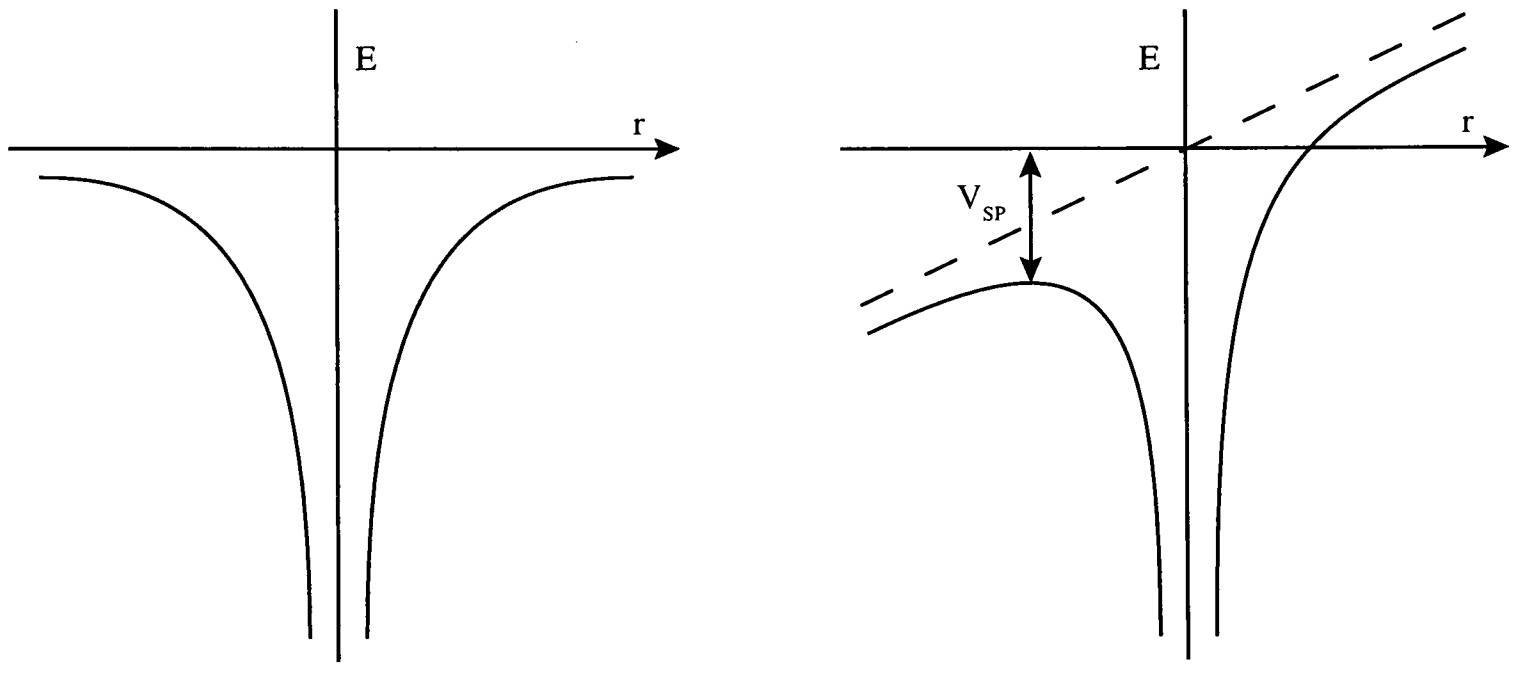

(a) V = -1/|r| (b) V = -1/|r| + Frcosθ

Figure 1.11: *Classical model of the potential of an electron in a hydrogen atom in the absence (a) and presence (b) of an electric field along the z-axis. (b) illustrates the presence of a barrier in the potential above which states can ionise.*

In a classical picture this maximum represents a field modified ionisation threshold, such that any states lying above this in energy will be ionised directly by the field. The potential of the electron in this field, in atomic units, is given by

$$V(z) = -\frac{1}{|z|} + Fz \qquad 1.23$$

and consequently the maximum is defined by the equation

$$\frac{\partial V(z)}{\partial z} = \text{sign}(z) \times \frac{1}{z^2} + F = 0 \qquad 1.24$$

giving

$$z = \frac{1}{\sqrt{F}}. \tag{1.25}$$

The electron potential at this point then takes the value

$$V_{SP} = -2\sqrt{F}. \tag{1.26}$$

As a result the field required for adiabatic ionisation, for a state of given principal quantum number, is

$$F = \frac{1}{16n^4}. \tag{1.27}$$

In laboratory units (wavenumbers) the modified ionisation potential, I, is more conveniently expressed [55] as a function of the applied electric field, F, in Vcm^{-1} by

$$I = I_0 - 6.12\sqrt{F} \tag{1.28}$$

where I_0 is the ionisation potential of the series in the absence of a field. Following this equation, the blue-shifted Stark states, whose energy rises in the field, will reach the energy of the classical ionisation threshold at relatively low field whereas Stark states with energies that decrease in the field, the so-called red-shifted states, will require a greater field to reach the classical threshold. This classical approach suggests that only states located above the maximum may ionise and this is an over simplification. Additionally, due to the finite width of the barrier, all states below the barrier are also susceptible to ionisation, as the electron may be lost via tunnelling through the barrier in the z direction. In reality, however, only those states located immediately below the barrier can ionise via this tunnelling pathway on the experimental timescale. For field ionisation to be detected experimentally it was assumed by Chupka [55] that it must occur at a rate of at least $10^9\ \mathrm{s}^{-1}$. In reality a rate of $10^7\ \mathrm{s}^{-1}$ is sufficient.

A truer picture takes into account the behaviour of the individual states in the presence of a field, as previously described above for the Stark effect. A useful formula for calculating the field ionisation rates of hydrogenic Rydberg states is presented by Damburg and Kolosov [50]. The rate, Γ, for a given quantum state defined by the quantum numbers n, n_1, n_2 and m, is determined as a function of the field, F, by

$$\begin{aligned}\Gamma &= \frac{(4R)^{2n_2+m+1}}{n^3 n_2!\,(n_2+m)!} \exp\left[-\frac{2}{3}R - \frac{1}{4}n^3F\right. \\ &\quad \left.\times\left(34n_2^2 + 34n_2m + 46n_2 + 7m^2 + 23m + \frac{53}{3}\right)\right]\end{aligned} \tag{1.29}$$

where $R = (-2E_{nkm})^{\frac{3}{2}}/F$. The value of E_{nkm} is the Stark energy (in wavenumbers) and can be calculated using the formula given in Equation 1.21.

Applying Equation 1.29 it is found that for blue-shifted Stark states the field needs to rise to $\sqrt{F} = E_0/3.1$ in order for the rate of ionisation to be measurable. The value E_0 represents the zero-field energy of the state below the ionisation threshold. In contrast, for red-shifted Stark states a value of $\sqrt{F} = E_0/4.6$ is sufficient. At first sight this seems to contradict the fact that the red-shifted states are energetically stabilised by the field compared to the blue-shifted states. However, the red-shifted states have wavefunctions which are localized near the barrier. Consequently they exhibit fast ionisation rates, ionizing as a soon as is energetically possible. Conversely, the wavefunctions of the blue-shifted states are located away from the region of the saddle point and they are relatively stable to ionisation, that is they have comparatively slow ionisation rates. These facts, together with the ionisation rate limit, serve to explain this apparently contradictory behaviour. This variation in ionisation behaviour from one edge of the manifold to the other is observed in the asymmetric line-shapes of ZEKE spectra [56].

Looking now at the ionisation behaviour of the entire manifold, then all states will be field ionised for $\sqrt{F} > E_0/3.1$ while the probability of ionisation decreases in the range $E_0/3.1 > \sqrt{F} > E_0/4.6$. Below this lower limit ionisation does not occur in any state at a rate experimentally measurable. Consequently it can be seen that the classical picture, whereby a state is either bound or unbound depending on its position relative to a new, field dependent ionisation threshold (Equation 1.28), is an inadequate description. This discussion is summarised in Figure 1.12 which depicts both the classical field ionisation limit as well as the fields required for field ionisation calculated using Equations 1.21 and 1.29.

1.4.3 Non-hydrogenic systems

The effects of electric fields on Rydberg states of non-hydrogenic systems differ from the situation previously presented for the H atom. This qualitative difference can be attributed to the fact that the core-electron interaction is no longer purely Coulombic at short range for the low-l states which exhibit a non-zero quantum defect. This departure manifests itself in two ways as illustrated in the artificial Stark map for H_2 molecules shown in Figure 1.13.

At zero field the low-l states are no longer degenerate with the high-l states and at low field strengths these low-l states are only weakly mixed with the high-

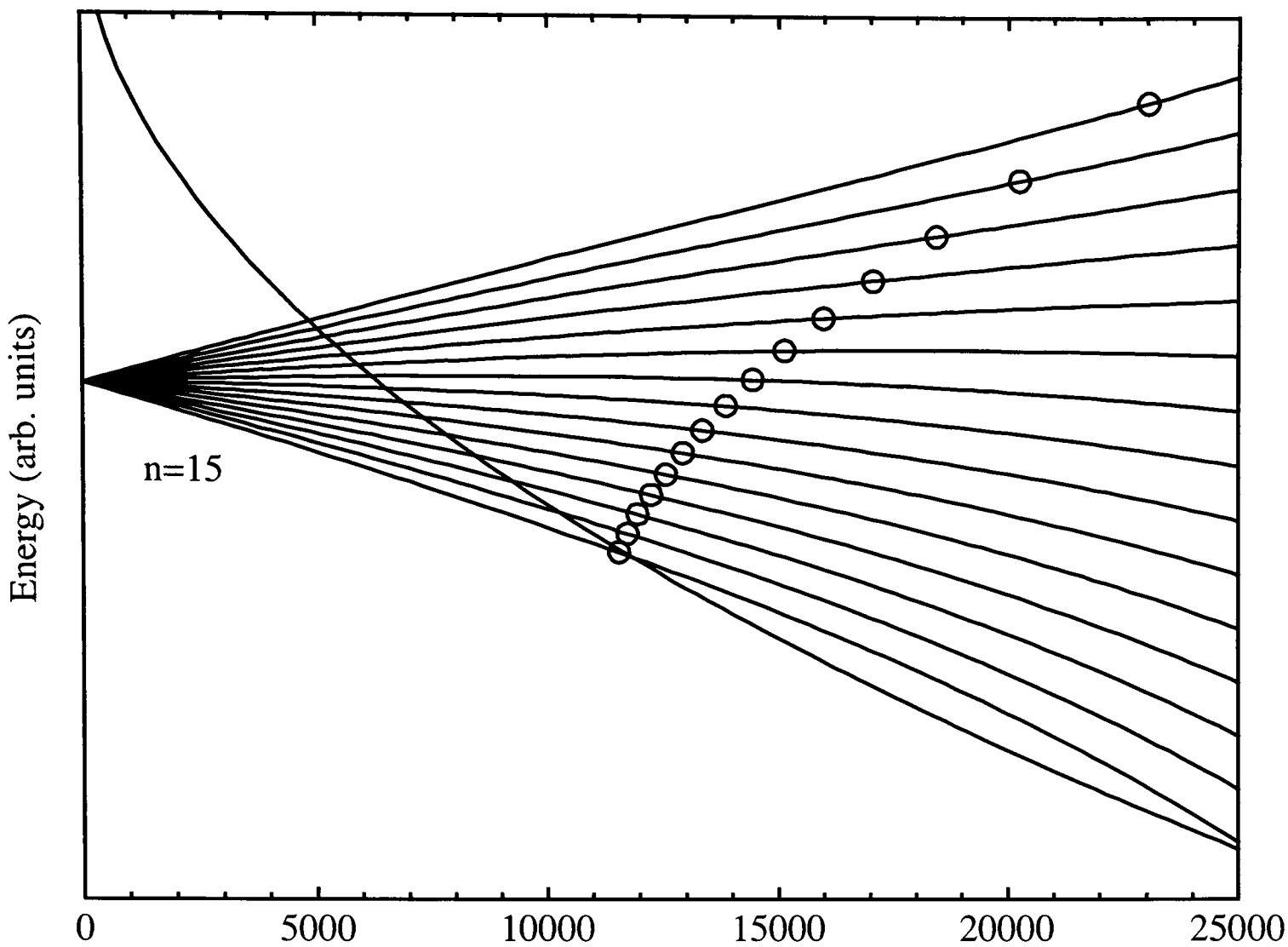

Figure 1.12: *Hydrogenic field ionisation in the $n = 15$, $m = 0$ manifold of states. The open circles represent the critical fields for hydrogenic field ionisation at a rate of $10^9\ s^{-1}$, calculated using Equations 1.21 and 1.29. The classical field limit for 100% ionisation of the states (see Equation 1.28) is indicated by the solid line. This figure is reproduced from [57].*

l states. The Stark shifts of these low-l states are well described at low field by a variation which is quadratic with the field. The high-l states, however, are non-penetrating and continue to follow hydrogenic behaviour even at low field strengths. As the field strength increases the low-l states are gradually mixed into the "hydrogenic manifold". If the quantum defect is regarded as a perturbation to the hydrogenic energy then its first order shift of the energy is given by δ_l/n^3, that is the energetic separation of the state from the hydrogenic manifold. The mixing of a low-l state with the high-l manifold becomes significant when the outermost member of the manifold approaches the position of the low-l state. Referring to Equation 1.20 above this shift occurs at a field given by $\Delta E = 3n^2F/2$. Consequently, in this first order approximation, the linear Stark effect is assumed to dominate for all l values when

$$\frac{3n^2F}{2} \geq \frac{\delta_l}{n^3}. \qquad 1.30$$

It is also prudent to remember the selection rule on l for Stark mixing given previously, $\Delta l = \pm 1$. This means that only the highest of the states exhibiting a quantum defect can mix with the manifold in this manner. Consequently for an s-state to mix with the manifold it must first mix with a p, then a d, and then an f-state.

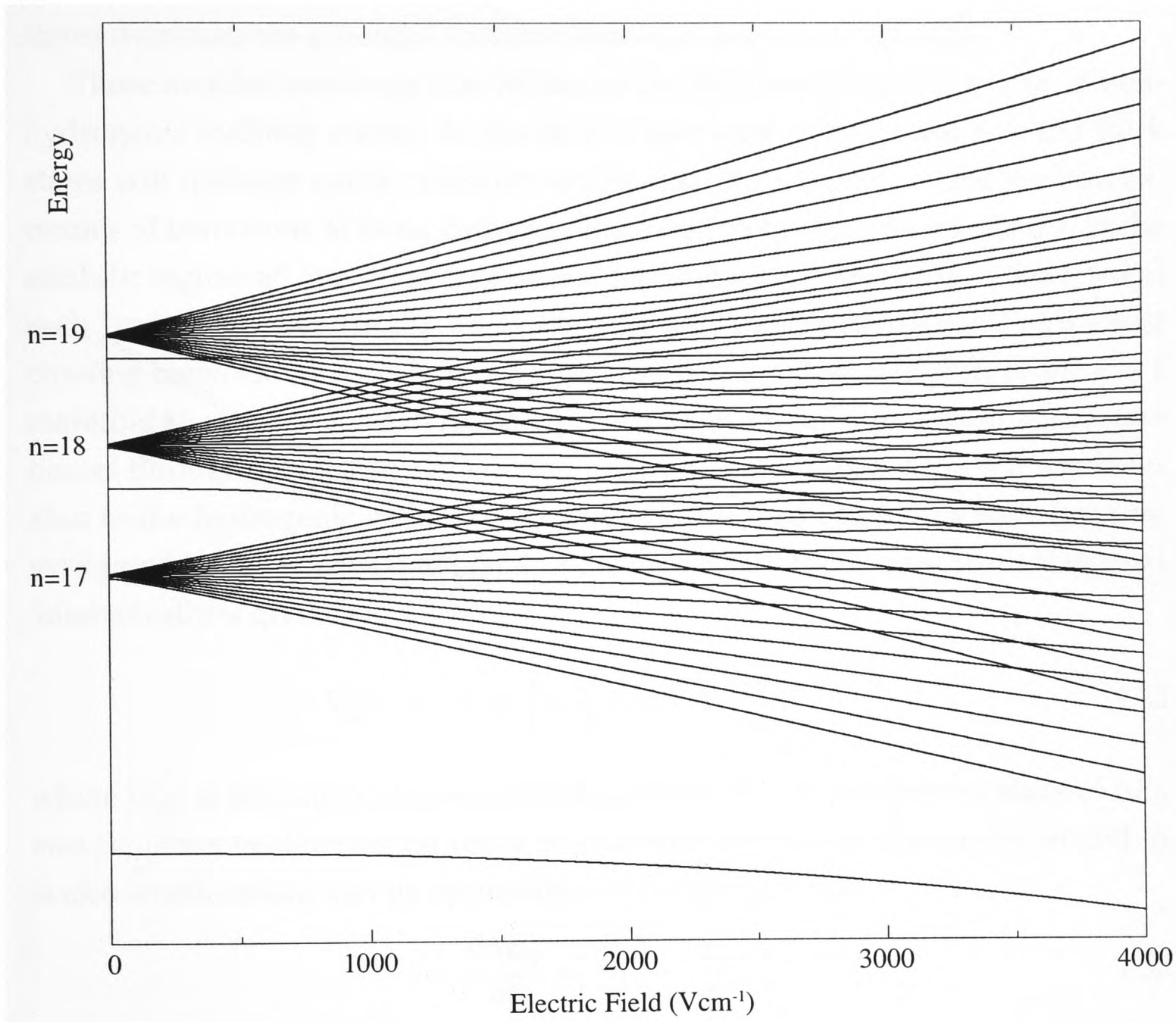

Figure 1.13: *Calculated Stark map of H_2 including only the $N^+ = 0$, $M_J = 0$ states associated with $n = 17 - 19$. It should be noted that states of other principal quantum number and also those exhibiting non-zero core rotational angular momentum would need to be included for a realistic calculation.*

The other behavioural difference exhibited by non-hydrogenic systems arises due to the fact that the additional symmetry provided by the z component of the Runge-Lenz vector in the H-atom case is not present here. This again is due to the deviation of the core-electron potential from a pure Coulombic form. As a result states with the same m quantum number interact and all crossings where $m = m'$ are now avoided. Quantum mechanically this is expressed by the fact that the

matrix element

$$\left|\langle nn_1n_2m|\, V\, |n'n_1'n_2'm'\rangle\right| \tag{1.31}$$

is non-zero in non-hydrogenic systems. In the case of low-m states these avoided crossings are quite distinct whereas at high-m they are too small to be observed. This is a consequence of the fact that as the low-l character of the Stark mixed states decreases the potential becomes more Coulombic in character.

These avoided crossings also influence the field ionisation behaviour of non-hydrogenic Rydberg states. As the field is increased it is feasible that the Stark states will undergo many crossings on the way to ionisation. There are two extremes of behaviour at these crossings that need to be considered. Firstly, in the *adiabatic* regime all crossings are avoided and the energy trajectory is deflected at each "crossing" point. In this adiabatic case field ionisation will occur at the first crossing between the state initially populated and a red-shifted state of the $n+1$ manifold to occur beyond the saddle point energy. On the other hand, if the state passes through each crossing *diabatically* then field ionisation occurs in a manner akin to the hydrogenic case. The dynamics at the crossing points have been investigated by Rubbmark *et al* [58] and the probability that a crossing is traversed adiabatically is given by

$$P_{ad}^{ij} = 1 - \exp\left[-\frac{2\pi}{\hbar}\left|V_{ij}\right|^2\left(\frac{d\Delta E_{ij}}{dt}\right)^{-1}\right] \tag{1.32}$$

where $\left|V_{ij}\right|$ is the matrix element from Equation 1.31. Approximate values of ΔE_{ij} and $\left|V_{ij}\right|$ may be determined using the formula derived by Komarov *et al* [59]. It is also worth noting that by application of the product rule

$$\frac{d\Delta E_{ij}}{dt} = \frac{d\Delta E_{ij}}{dF}\cdot\frac{dF}{dt}. \tag{1.33}$$

Thus taking Equations 1.31, 1.32 and 1.33 together it is clear that for fields that rise rapidly or for large values of m the probability of an adiabatic crossing is zero. Consequently the ionisation behaviour is well described using the hydrogenic model. However, if the field rises slowly or there is significant interaction between the states such that $\left|V_{ij}\right| > 0$, then $P_{ad}^{ij} \neq 0$ and the *adiabatic* description of field ionisation is more apt.

1.4.4 State accessibility and lifetimes

As mentioned previously the application of an external field has the effect of mixing together states according to the selection rule $\Delta l = \pm 1$. One major conse-

quence of this is the mixing of optically accessible l states with l states which are optically "dark" at zero field. The associated admixture of transition intensity means that high-l states may be directly populated in the field. Additionally, the mixing also results in a redistribution of zero-field lifetimes among the high field states. The diffuse nature of the high-l states effectively results in negligible Rydberg electron-core encounters and a dramatic increase of Rydberg state lifetimes, $\tau \propto n^4$ [55], compared to the n^3 zero-field scaling of lifetimes, is observed. Experimentally lifetimes of high-n atomic and molecular Rydberg states have been shown to scale as n^5 [60]. This even greater lifetime enhancement may be explained by the presence of inhomogeneous fields. In a homogeneous field the quantum number m is conserved. However, the presence of ions or other charged particles lifts this field homogeneity. Consequently there is, together with the admixture of l states, an admixture of m states. In the limit of complete mixing this is found to result in lifetimes that scale as n^5 [61, 62] for states with very high principal quantum number ($n > 100$).

1.5 Thesis outline

The work presented in this thesis focuses on the interaction of Rydberg molecules with metallic surfaces. It is hoped that, by utilising the properties of these molecules under the influence of even the smallest fields, it may be possible to gain an understanding of the ionisation processes occurring at the vacuum/surface interface. As with all new methods and investigations it is prudent to begin with the simplest scenario and progress to the more complex. The simplest of all molecules are the homonuclear diatomics and the work presented here focuses on the interaction of molecular hydrogen with both gold and aluminium surfaces.

In Chapter 2 the interaction of the hydrogen molecule with a metal surface is modelled using the hydrogen atom system and a potential associated with a jellium surface. Details of the complex scaling technique, and its application to the problem at hand, are presented, together with calculated values of the energies and linewidths of states with principal quantum number $n = 6 - 9$. The linewidths are then associated with the ionisation behaviour of the states in the presence of the metal surface, and a prediction of experimental behaviour of the higher-n states ($n = 17 - 22$) is presented by way of a scaling of the calculated lower-n information.

The experimental methodology and apparatus is detailed in Chapter 3 while

the experimental results are presented in Chapter 4. Here the first recorded observations of ionisation of Rydberg *molecules* at metal surfaces are presented and analysed. Investigations are carried out to determine whether the character of the initial state or the nature of the surface has any influence on the ionisation behaviour. The results are compared to those recorded previously for atoms [13] and explanations for the behaviour observed are presented.

CHAPTER

TWO

Theory and Simulation

When a molecule is placed outside a metal surface strong interactions lead to the hybridization of the molecular energy levels. Most importantly these molecular states become resonances, embedded in a continuum. That is they acquire an additional width, and the dominant contribution to these widths is electron transfer into the band structure of the metal [2, 63]. In general the greater the separation of the molecule from the surface the smaller the interaction and hence the higher and wider the tunnelling barrier becomes. Furthermore, the energy levels will shift as the potential around them is altered (see Section 1.1 for more detail).

Several previous theoretical studies have focused on the perturbation of an atom outside a metal surface. Early studies [64, 65] used perturbation theory to calculate the shifts and broadenings outside perfectly conducting metal surfaces using the asymptotic image potentials which diverge as the surface is approached. However, the widths and shifts are particularly sensitive to the exact nature of the potential (see Section 2.2.2), especially at small atom-surface separations, and so this method leads to inaccurate widths at short separations. It is also the case that perturbation theory breaks down at small separations due to the large number of atomic states that contribute. These issues were addressed in later studies [14, 66] which employed non-perturbative techniques and a model potential. Irrespective of the particular method employed the later studies agreed quantitatively with each other in behaviour. A more recent study involving the stabilization technique has also been reported [67] and, with the exception of very small atom-surface separations, this agrees quantitatively with the other non-perturbative methods.

In the following discussion the complex scaling technique, used by Nordlander and Dunning *et al* [14], is utilised to calculate both the energies and widths of the resonant states. The Rydberg states of the hydrogen molecule are modelled using the hydrogen atom system which acts as a good first approximation to a molecular state with a principal quantum number $n > 5$. An original Fortran program has been developed to implement the theory.

2.1 Complex scaling

The method of complex scaling, often referred to as dilatation analytic continuation or the complex coordinate method, has been used extensively in the calculation of atomic resonances in phenomena such as the Stark effect [68] or the calculation of photo-ionisation cross sections. The attraction of the complex scaling method is that by use of the transformation, $r \rightarrow re^{i\theta}$, the usually divergent resonance wavefunctions become convergent. An introduction to the workings of the method, as well as its implementation to the present problem of molecule-surface collisions, is outlined below. Detailed reviews [69, 70, 71] and worked examples [70] can be found in the literature.

2.1.1 The problem of resonances

The wavefunction of a resonance state is most simply described by

$$\Psi(t) = e^{(-i\omega t)}\Psi(t=0). \tag{2.1}$$

The required roots to this equation are associated with eigenstates that exhibit Siegert boundary conditions [72] and in the asymptotic region the radial wavefunction satisfies the boundary condition

$$\Psi(r) \rightarrow e^{ikr} \qquad \text{for } r \rightarrow \infty \tag{2.2}$$

where the complex wavenumber $k = k_R - ik_I$. The eigenenergy, $E = \hbar\omega$, in Equation 2.1 is related to this complex wave number by $\omega = -\frac{1}{2}(k_R - ik_I)^2$. The energy therefore becomes complex, $E = E_R - iE_I$, with the real part associated with the energy of the level and the imaginary part describing the half-width of the resonance, that is $E = E_R - i\Gamma/2$.

The resonance wavefunction given in Equation 2.2, expanded in terms of k, is

$$\lim_{r\rightarrow\infty} \Psi(r) \sim e^{\{ik_R r + k_I r\}}. \tag{2.3}$$

Unlike bound-state wavefunctions this resonance wavefunction does not vanish at the asymptotic limit, instead it diverges at complex resonance energies. As such, a direct approach to solving the Schrödinger equation is practically difficult as in reality finite basis sets must be used.

However, if a complex variable substitution is introduced in the radial coordinate the boundary conditions are changed. The substitution chosen is $r \rightarrow re^{i\theta}$, where θ is real and positive, and the asymptotic form of the radial wavefunction, $\Psi(r)$, now becomes

$$\begin{aligned} \lim_{r\to\infty} \Psi(r) &\sim e^{\{ikre^{i\theta}\}} \\ &= e^{\{ik_R\cos(\theta)+k_I\sin(\theta)\}r} e^{\{k_I\cos(\theta)-k_R\sin(\theta)\}r}. \end{aligned} \tag{2.4}$$

Under conditions where $\pi/2 > \theta > 0$ this wavefunction becomes asymptotically convergent (c.f. bound-state boundary conditions) and indeed vanishes asymptotically if the scaling angle, θ, is chosen such that

$$\theta > \arctan\left(\frac{k_R}{k_I}\right). \tag{2.5}$$

As a result it is now possible to obtain the resonance parameters (position and width) by using L^2 basis functions identical to those used to solve bound-state eigenvalue problems, negating the need to introduce complicated continuum wavefunctions.

2.1.2 The properties of the rotated Hamiltonian

In practice the radial coordinates of the Hamiltonian are transformed such that

$$H(r) \rightarrow H\left(re^{i\theta}\right) \tag{2.6}$$

and for systems with Coulombic interactions this simply yields

$$H\left(re^{i\theta}\right) = e^{-2i\theta}T(r) + e^{-i\theta}C(r) + V\left(re^{i\theta}\right) \tag{2.7}$$

where $T(r)$ and $C(r)$ are the usual kinetic and Coulombic parts of the Hamiltonian.

The mathematical basis for this method is given in work by Aguilar, Balslev and Combes [73, 74] and they have rigourously shown that under the transformation of the Hamiltonian given in Equation 2.6 the following statements hold:

- The bound-state eigenvalues, where they exist, are identical to those of the original unscaled Hamiltonian.

- The positions of the scattering thresholds remain unchanged by this transformation and the associated continua are rotated downward into the complex plane by an angle of 2θ, where θ is the scaling angle.
- Complex eigenvalues associated with resonances are "exposed" by the rotated continua once $\theta > \frac{1}{2}\arg(E)$. As stated above $E = E_R - iE_I$ and hence these resonance positions represent both the energy and the lifetime of the state simultaneously.

The spectrum associated with both the scaled and unscaled Hamiltonian in the energy plane is shown in Figure 2.1. This provides a graphical depiction of the three statements given above.

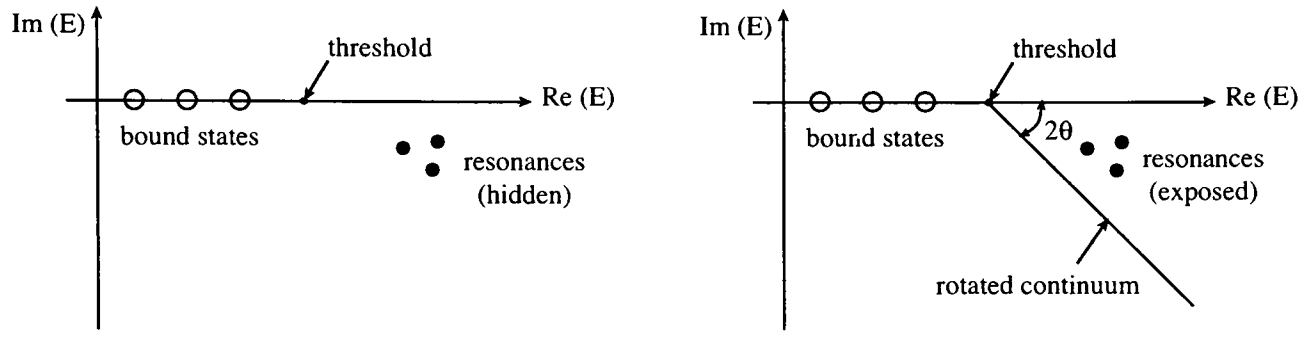

Figure 2.1: *The spectrum of $H(r)$ and $H(re^{i\theta})$ in the energy plane is shown in (a) and (b) respectively. Note that the resonances can only been seen as a result of the rotation and that the position of the bound states and the threshold remain invariant under the transformation.*

In summary, the method of complex scaling allows one to calculate both the position and the width of a resonant state simultaneously using only a single square integrable eigenfunction of the complex-scaled Hamiltonian. However, it should also be noted that, as Hermitian Hamiltonians can only produce real eigenvalues, a disadvantage of this method is that calculations must involve non-Hermitian Hamiltonians and the diagonalization of complex matrices.

2.2 Surface calculations

2.2.1 The Hamiltonian

In order to obtain resonances of the simple one-electron model used here it is necessary to solve the electronic Schrödinger equation:

$$H\psi = \left[-\frac{1}{2}\frac{d^2}{dr^2} + \frac{l(l+1)}{2r^2} - \frac{1}{r} + V_s(r,\alpha,\phi)\right]\psi = E\psi \qquad 2.8$$

where V_s is the potential associated with the surface.

Application of the coordinate rotation, $r \rightarrow re^{i\theta}$, as described above, leads to the rotated Hamiltonian:

$$H(\theta) = -e^{-2i\theta}\left\{\frac{1}{2}\frac{d^2}{dr^2} + \frac{l(l+1)}{2r^2}\right\} - \frac{e^{-i\theta}}{r} + V_s\left(re^{i\theta}, \alpha, \phi\right). \qquad 2.9$$

2.2.2 The form of the potential

The form of the potential V_s is an important consideration in the calculation of the resonances. The Rydberg atom is considered as a two particle system of electron and ion core. To a first approximation the potential may be considered as the interactions between these point charges and image point charges in the metal. The geometry and contributions to the potential arising from the presence of the surface using this approximation are shown in Figure 2.2. In Cartesian coordinates the position of the electron is denoted by the lower case letters (x, y, z) and, given the symmetry about the azimuthal angle, this can be further simplified to (ρ, z). The position of the ion core is donated by the upper case letter Z.

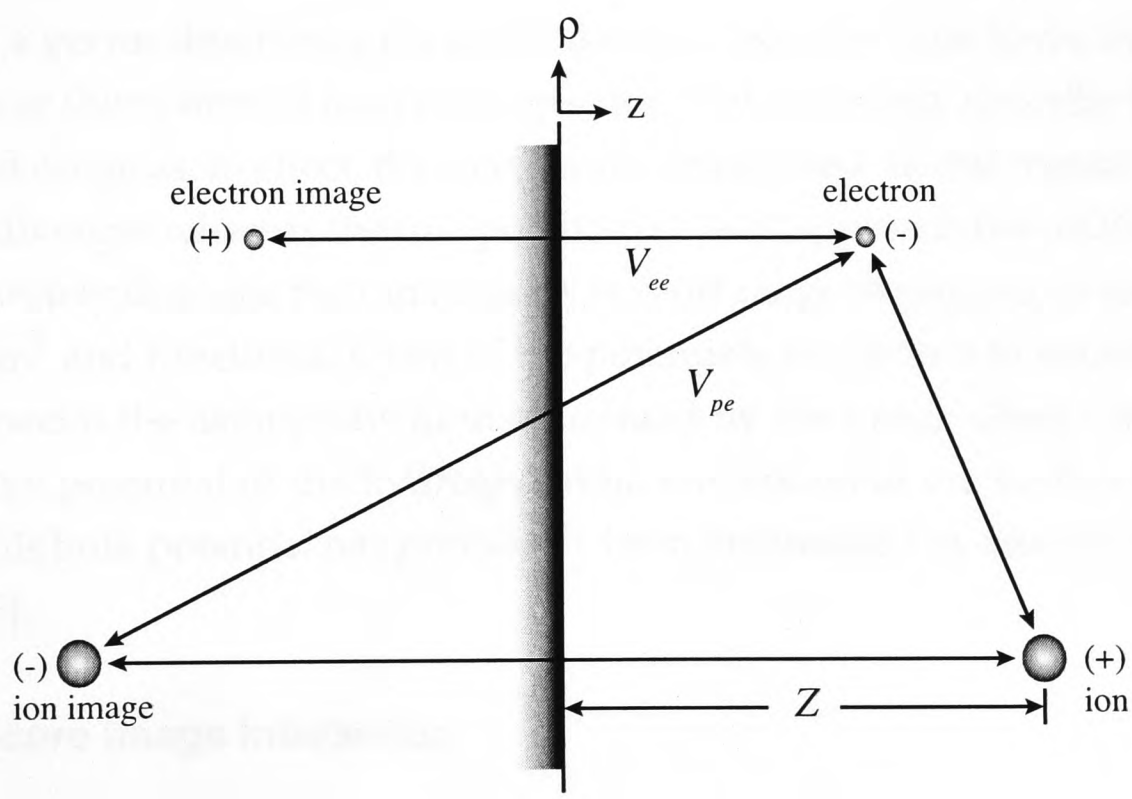

Figure 2.2: *Diagram of the geometry of the charges relative to the surface, and the contributions to the potential, V_s, as outlined in the text.*

It can be seen that V_s is dependent on two interactions, V_{pe} and V_{ee}. The first term describes the repulsive interaction of the electron and the image of the core induced within the surface, whereas the second, V_{ee}, describes the attractive in-

teraction of the electron with its own image. That is

$$V_{tot} = V_{pe} + V_{ee}. \tag{2.10}$$

It should also be noted that a third term exists which describes the effective interaction of the ion core with its own image. This has a Z-dependent effect on the total energy of the system, as well as contributing significantly to the projectile acceleration after ionisation. Consequently it should be included in any subsequent electrostatic ion-trajectory calculations. However it has no effect on the relative energies and widths of the states as it depends solely on the nuclear coordinate. As a result it is not included here in the resonance calculations.

At large particle/surface separations these potentials are adequately described using the system of point image charges. The asymptotic limits of V_{pe} and V_{ee} are given by

$$\lim_{Z,z\to\infty} V_{pe}(\mathbf{r}, Z) = \frac{1}{\sqrt{(z+Z)^2 + x^2}} \tag{2.11}$$

$$\lim_{z\to\infty} V_{ee}(z) = -\frac{1}{4z} \tag{2.12}$$

where $\mathbf{r}$ is a vector describing the radial distance from the core to the electron.

However the system of image charges does not accurately describe the potential at short range as, in effect, the charges are delocalised. In this region the image potential diverges whereas the true potential should approach that of the bulk. To more accurately describe the interactions at short range the surface is modelled to be a jellium[1] and functional forms of the potentials are chosen to smoothly interpolate between the asymptotic limits provided by the image charge system and the effective potential of the hydrogen atom embedded in the surface bulk. The value of this bulk potential has previously been determined by density-functional theory [75].

Electron-core image interaction

The full treatment of the core induced surface potential, $V_{pe}(\mathbf{r}, Z)$, consists of two terms, an electrostatic term (el) and an exchange-correlation term (xc):

$$V_{pe}(\mathbf{r}, Z) = V_{el} + V_{xc}. \tag{2.13}$$

[1]The Jellium model assumes that electrons interact with one another in the presence of a uniform background of positive charge. As such the system properties are only dependent upon the density of electrons.

These terms have been calculated in full in previous work [76]. However in the results that follow this potential has been treated using the image charge model outside the surface and an approximation to the bulk potential inside the surface. This treatment is summarised as

$$V_{pe}(\mathbf{r}, Z) = \begin{cases} \frac{1}{\sqrt{(z+Z)^2+x^2}} & \text{if } z > 0 \\ \frac{1}{\sqrt{(Z)^2+x^2}} & \text{otherwise.} \end{cases} \quad 2.14$$

Although this is a greatly simplified treatment of a complicated problem, the results obtained agree well with the literature values and as such this potential appears to provide a sufficient description of the true behaviour.

Electron-electron image potential

For the electron-electron image interaction the model potential proposed by Jennings, Jones and Weinhardt [77] is used:

$$V_{ee}(z) = \begin{cases} \frac{-1+exp[-\beta(z-z_0)]}{4(z-z_0)} & \text{if } z > z_0 \\ \frac{V_0}{Aexp[B(z-z_0)]+1} & \text{otherwise} \end{cases} \quad 2.15$$

where $A = -1 - 4V_0/\beta$ and $B = -2V_0/A$. In the limit $z \to \infty$ Equation 2.15 converges to the correct self-image limit for a jellium surface

$$\lim_{z\to\infty} V_{ee}(z) = -\frac{1}{4(z-z_0)}. \quad 2.16$$

The value of z_0 is dependent on the type of jellium surface under investigation and defines the position of the image plane. For aluminium, with a Weigner-Seitz radius[2] of $r_s = 2.07$, $z_0 = 0.7$. The two constants V_0 and β are chosen such that the potential matches that calculated using the local-density approximation of Lang and Kohn [75], for small z, and take the values -0.574 and 1.25 [77] respectively in the case of aluminium.

An example of the total potential given by Equations 2.10, 2.14 and 2.15 is shown in Figure 2.3 together with the potentials calculated using the simple image charge model.

For comparison, the potentials used in the work of Nordlander and Tully [76] are shown in Figure 2.4. It is clear that the potentials calculated in the present work agree quantitatively with those previously used.

[2]The Wigner-Seitz radius is defined as the radius of the sphere occupied by a single electron in the metal.

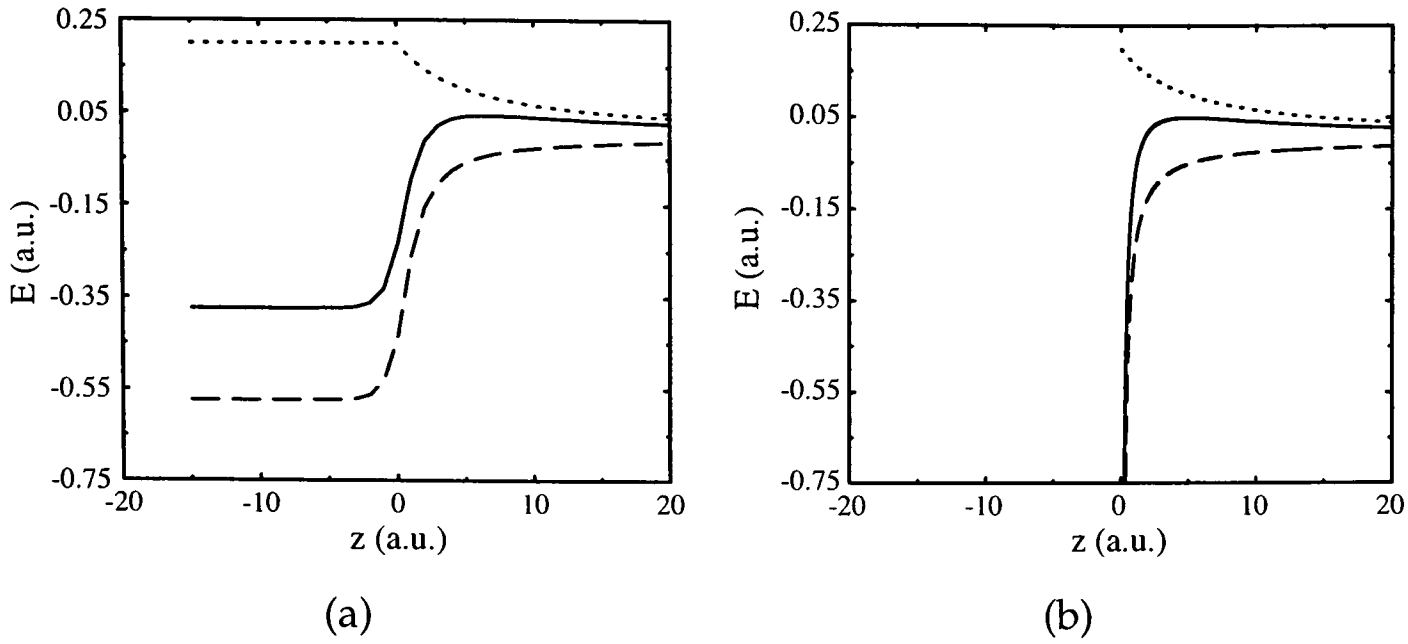

Figure 2.3: *The surface potentials outside a jellium surface are shown in (a). The dashed line is the bare surface electron potential ,V_{ee}, and the dotted line is V_{pe}, for a proton placed at $Z = 10$ a.u.. The total potential V_s is drawn with a solid line. For comparison the equivalent potentials calculated using a simple image-charge model are shown in (b).*

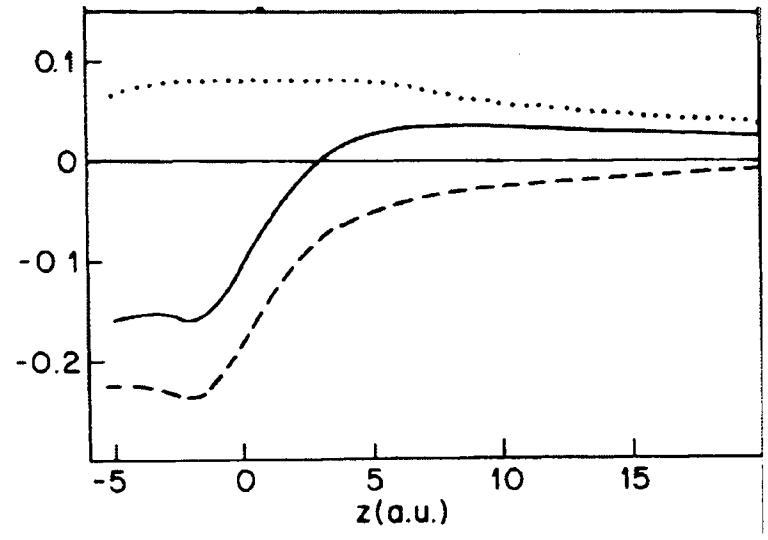

Figure 2.4: *The potentials used in previous work reproduced from reference [76]. The line styles represent the same potentials as in Figure 2.3.*

2.2.3 The basis functions

To obtain a solution to the Schrödinger equation with the Hamiltonian shown in Equation 2.9 for both bound and resonance states it is essential that the basis functions form a complete set. As a result the following basis functions are used [76]:

$$\begin{aligned} \Phi_{nlm} &= R_{nl}(r)\, Y_{lm}(\alpha,\phi) \\ &= C_{nl} exp\left[\frac{-\lambda r}{2}\right] r^{l+1} L_{n-1}^{2l+2}(\lambda r)\, Y_{lm}(\alpha,\phi) \end{aligned} \qquad 2.17$$

In this expression $L_{n-1}^{2l+2}(\lambda r)$ is a generalized Laguerre polynomial [78] and Y_{lm}

is a spherical harmonic. λ is a parameter that is varied to optimise the basis and in general takes the value $2/n$ where n is the principal quantum number of the state under investigation. C_{nl} is a coefficient defined such that the radial parts of the basis functions are normalised and takes the usual form:

$$C_{nl} = \frac{1}{\sqrt{\int_0^\infty dr \left[R_{nl}(r)\right]^2}}. \qquad 2.18$$

In practice it is not possible to use a complete basis set but accurate results can still be obtained if the basis is sufficiently large. In the calculations described below the basis set is specified by two parameters, l_{max} and N_l. The first of these denotes the maximum value of the angular momentum quantum number, l, used. The second indicates the number of radial functions included for each value of l. Consequently the basis set contains $N_l \times (l_{max}+1)$ basis functions. The explicit values of l_{max} and N_l are determined by convergence tests and it was found that in the case of states initially populated with $n = 2$, convergence could be guaranteed if $l_{max} = 9$ and $N_l = 10$. For calculations involving states of principal quantum number , $6 < n < 9$, up to 400 basis functions were required for sufficient accuracy (see Section 2.4).

2.2.4 Calculation of the matrix elements

The matrix elements can now be calculated in three distinct parts. The first two of these, the kinetic and Coulombic energy matrix elements, are constructed from a real and a complex part. Consequently evaluation can be performed for $\theta = 0$ and then the resulting integrals post-multiplied by the scaling factor to yield the rotated matrix elements.

Kinetic energy

$$\begin{aligned} T_{nlm;n'l'm'}(\theta) &= -\frac{e^{-2i\theta}}{2} C_{nl} C_{n'l'} \delta_{ll'} \delta_{mm'} \qquad 2.19 \\ &\times \int_0^\infty dr e^{-\frac{\lambda r}{2}} r^{l+1} L_{n-1}^{2l+2}(\lambda r) \left[\frac{d^2}{dr^2} - \frac{l(l+1)}{r^2}\right] r^{l'+1} e^{-\frac{\lambda r}{2}} L_{n'-1}^{2l'+2}(\lambda r) \end{aligned}$$

Coulombic energy

$$\begin{aligned} C_{nlm;n'l'm'}(\theta) &= -e^{-i\theta} C_{nl} C_{n'l'} \delta_{ll'} \delta_{mm'} \qquad 2.20 \\ &\times \int_0^\infty dr e^{-\lambda r} r^{l+l'+1} L_{n-1}^{2l+2}(\lambda r) L_{n'-1}^{2l'+2}(\lambda r) \end{aligned}$$

Surface potential

Calculation of the matrix elements associated with the surface potential is more challenging as the potential is dependent upon both the radial and angular coordinates of the electron.

$$\begin{aligned} V_{nlm;n'l'm'}(\theta) &= \int_0^\infty dr \int_0^\pi d\alpha \sin\alpha \int_0^{2\pi} d\phi \\ &\times C_{nl} C_{n'l'} e^{-\lambda r} r^{l+l'+2} L_{n-1}^{2l+2}(\lambda r)\, L_{n'-1}^{2l'+2}(\lambda r) \\ &\times Y_{lm}^* \left[V_s\left(re^{i\theta}, \alpha, \phi\right) \right] Y_{lm}. \end{aligned} \tag{2.21}$$

This integral cannot be separated into real and complex parts as in Equations 2.19 and 2.20 . A second problem arises as, due to the intricacies of complex arithmetic, the analytic continuation of the rotated potential is not known and so $V\left(re^{i\theta}\right)$ cannot be calculated. If instead, however, we make a variable substitution, $x = re^{i\theta}$, then it is possible to rewrite Equation 2.21 as follows:

$$\begin{aligned} V_{nlm;n'l'm'}(\theta) &= \int_0^\infty dx e^{-i\theta} \int_0^\pi d\alpha \sin\alpha \int_0^{2\pi} d\phi \\ &\times C_{nl} C_{n'l'} e^{-\lambda x e^{-i\theta}} \left(xe^{-i\theta}\right)^{l+l'+2} L_{n-1}^{2l+2}\left(\lambda x e^{-i\theta}\right) L_{n'-1}^{2l'+2}\left(\lambda x e^{-i\theta}\right) \\ &\times Y_{lm}^* \left[V_s(x, \alpha, \phi) \right] Y_{l'm'}. \end{aligned} \tag{2.22}$$

As a result the potential function, $V_s(x, \alpha, \phi)$, remains a real entity and although the basis functions are now complex, a solution is achievable.

All three of these matrix element types are efficiently calculated by use of Gauss-Laguerre quadrature routines, and diagonalization of the resulting complex general matrix leads to the eigenvalues of the resonances. Since the potential function has cylindrical symmetry, basis functions with different m do not interact and the final matrix has a block diagonal structure. The eigenvalue problem may, therefore, be represented by the secular equation,

$$\det\left(\mathbf{H}_m(\theta) - E(\theta)\,\mathbf{I}\right) = 0 \tag{2.23}$$

where $\mathbf{I}$ is the identity matrix. Numerically solving Equation 2.23 yields both the bound and resonant state energies and linewidths.

2.2.5 Location of the resonances

Although the above discussion of the complex scaling technique suggests that the accurate eigenvalues are readily calculable if the rotation angle θ is chosen such that Equation 2.5 holds, this is not in fact the case in practice. This is the formally exact result for the situation where the basis set is complete and, in this case alone, the resonance positions in the complex plane are independent of the value of θ (given the above condition). In reality the basis set is never complete. However, if the basis set is large enough the resonance positions will only vary slightly with the value of θ [73]. Accurate determination of the resonance positions therefore requires that the complex eigenvalues have converged with respect to both basis size and the value of θ. This point is illustrated in Figure 2.5 for the two $n = 2, m = 0$ resonances of a hydrogen atom placed 10 a.u. in front of an aluminium surface. The resonance positions for a range of values of θ are shown. The basis set was chosen such that the positions are converged relative to basis size and in this case contained 100 basis functions with $l_{max} = 9$ and $N_l = 10$.

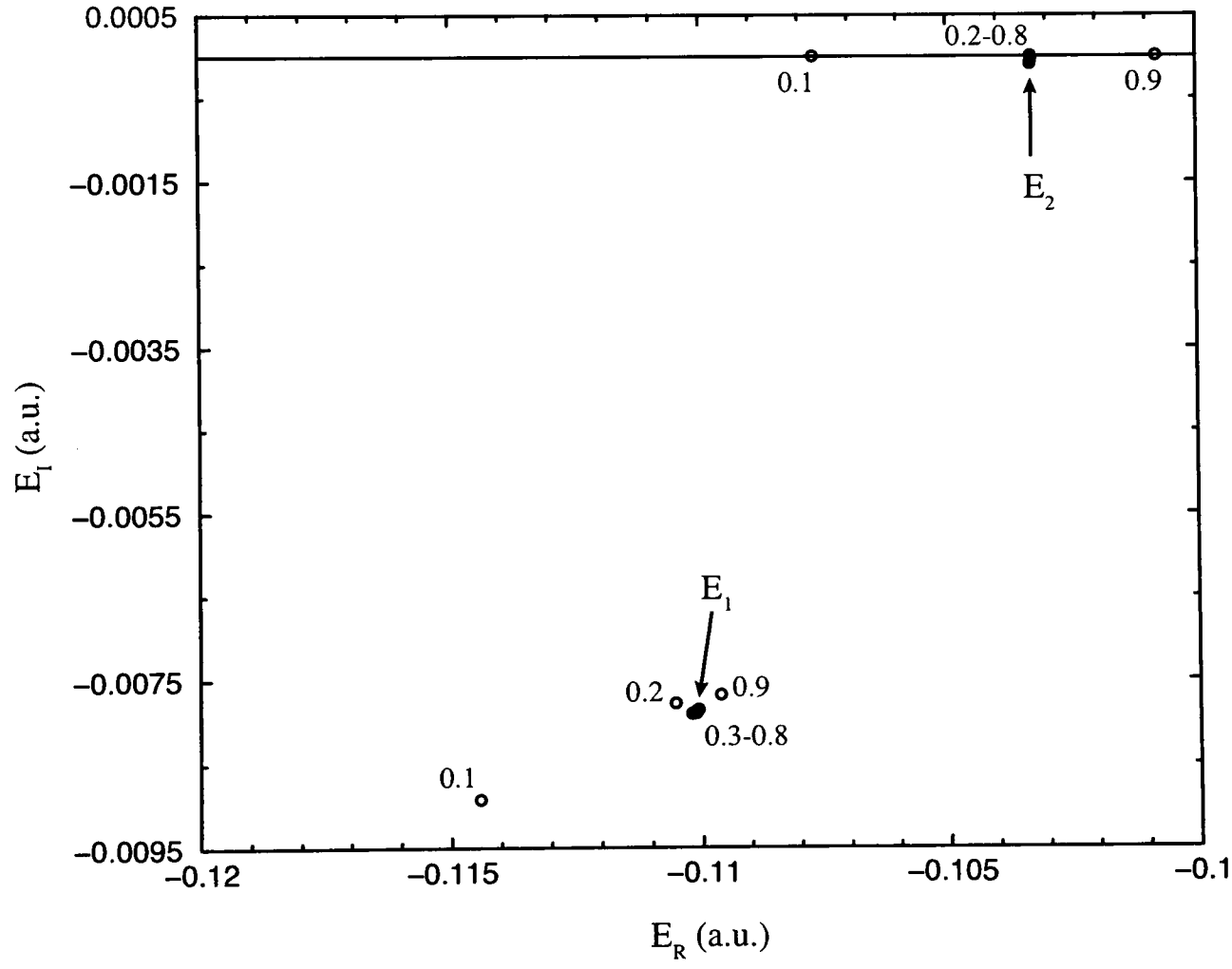

Figure 2.5: *The location of the two $n = 2, m = 0$ resonances, E_1 and E_2, for a core-surface separation $Z = 10$ a.u.. The numerical labels give the value of θ used in the scaling. The solid horizontal line depicts the position of $E_I = 0$.*

It is clear that the trajectory converges in two places, and these are indeed good approximations to the values of the resonances when compared to calculated values in the literature [67]. With the exception of small and large θ, the position is relatively independent of θ. The exact values can be found by locating the point at which the resonant position is least sensitive to the change of θ, that is the point at which the trajectory is most stabilized with respect to θ. Hence, θ_{opt} is defined as follows

$$\theta_{opt} = \theta \quad \text{when } \frac{dE}{d\theta} \text{ is a minimum.} \tag{2.24}$$

In the example shown here $\theta_{opt} = 0.4$ and the resonance positions were found to be $E_1 = -0.110 - 0.008i$ and $E_2 = -0.1033 - 8.3 \times 10^{-5}i$.

Once an optimum value for θ has been determined it is possible to calculate the shift in energies and the broadening of the states as the surface is approached by repeating the calculation for a range of atom-surface separations. It is important to note, however, that each resonance will have a slightly different value of θ_{opt} and this will change with Z. However, if the basis set is sufficiently large any slight variation of θ_{opt} can be ignored as the calculation will remain converged. The variation of the values E_R and E_I with the position of the core relative to the surface, Z, for the two $n = 2, m = 0$ states of atomic hydrogen are shown in Figure 2.6. Included in the left-hand figure, showing the energy of the levels, are all the "resonances" visible in that region. In order to distinguish between positions that are simulating the continuum and those which represent the actual states we are interested in it is necessary to perform a second trajectory calculation. If θ remains fixed but the basis optimisation parameter, λ, is varied then the states of interest shift only slightly. However, the other positions change rapidly. As a result, resonance positions are located precisely by first optimizing θ at a single value of Z and then varying λ and identifying localized positions for all Z. This procedure was used to identify the trends in energy shift shown in the left-hand figure. The half-widths shown in the right-hand figure are simply the imaginary parts of the complex eigenvalues. An alternative procedure, which was adopted later, involved tracking a state as the value of the separation, Z, was incrementally decreased. By finding the eigenvector at the new separation with the highest overlap with the eigenvector of the state at the previous separation, it was possible to monitor the *adiabatic* evolution of the state under investigation. Such a procedure was useful at higher n, where eigenvalues at a greater number of separations were required (see Section 2.4).

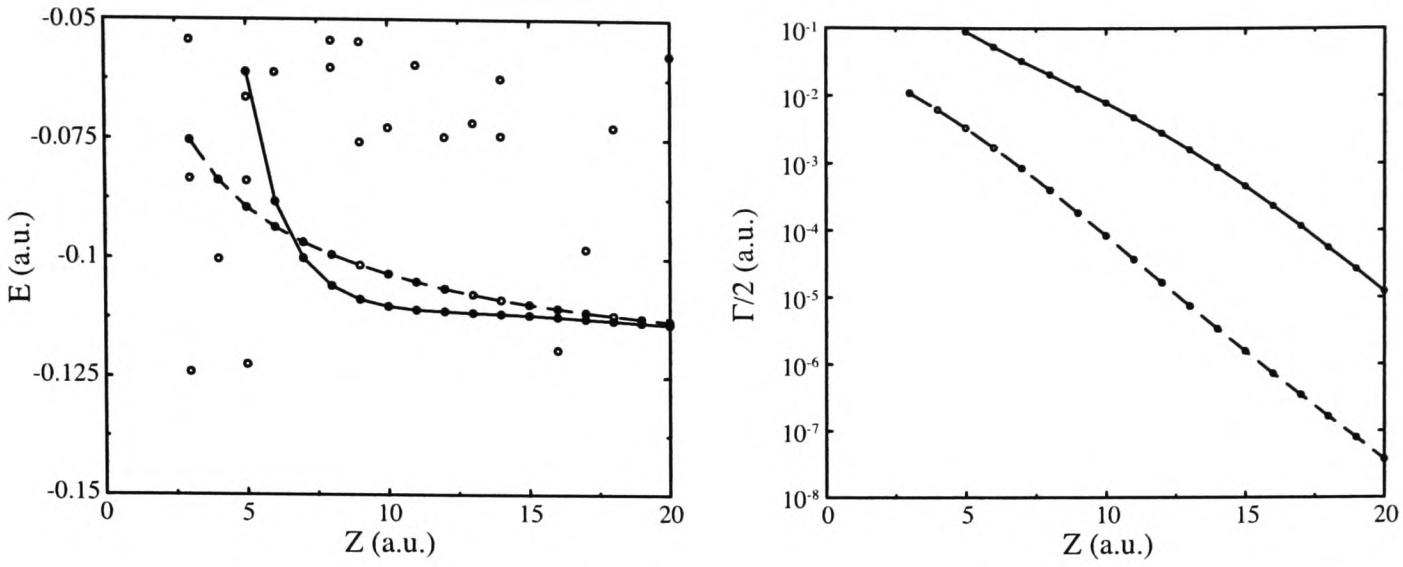

Figure 2.6: *Calculated energies (left) and associated half-widths (right) for the two $n = 2, m = 0$ hydrogen Rydberg states in front of a jellium (aluminium) surface. Z is the core-surface separation.*

Before extending the calculation to higher n it was necessary to ensure that there was good agreement between the results presented here, calculated using the potential described in Section 2.2.2, and those obtained by Nordlander *et al* [76] who employed a self consistent approach to the calculation of the potential. Their results are shown below in Figure 2.7. Excellent agreement is found (although it should be noted that the scale in Figure 2.7(b) is incorrectly labelled Γ where in fact it should read $\Gamma/2$ as in Figure 2.6).

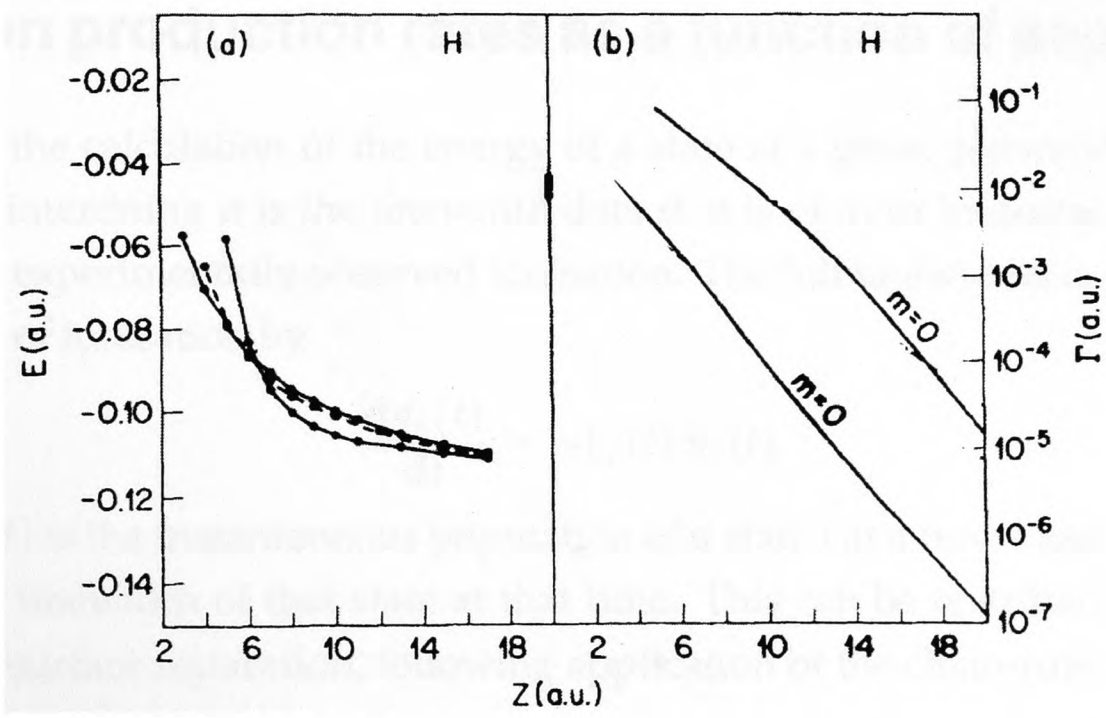

Figure 2.7: *The energies and linewidths of the two $n = 2$, $m = 0$ states calculated in previous work for a hydrogen atom (reproduced from reference [76]). Z is the core-surface separation. The dashed line in (a) represents the $n = 2, m = 1$ state.*

Similar agreement also exists for other low-n states presented in [76] and the results for $n = 1, 2$ and 3, calculated as above, are shown below in Figure 2.8.

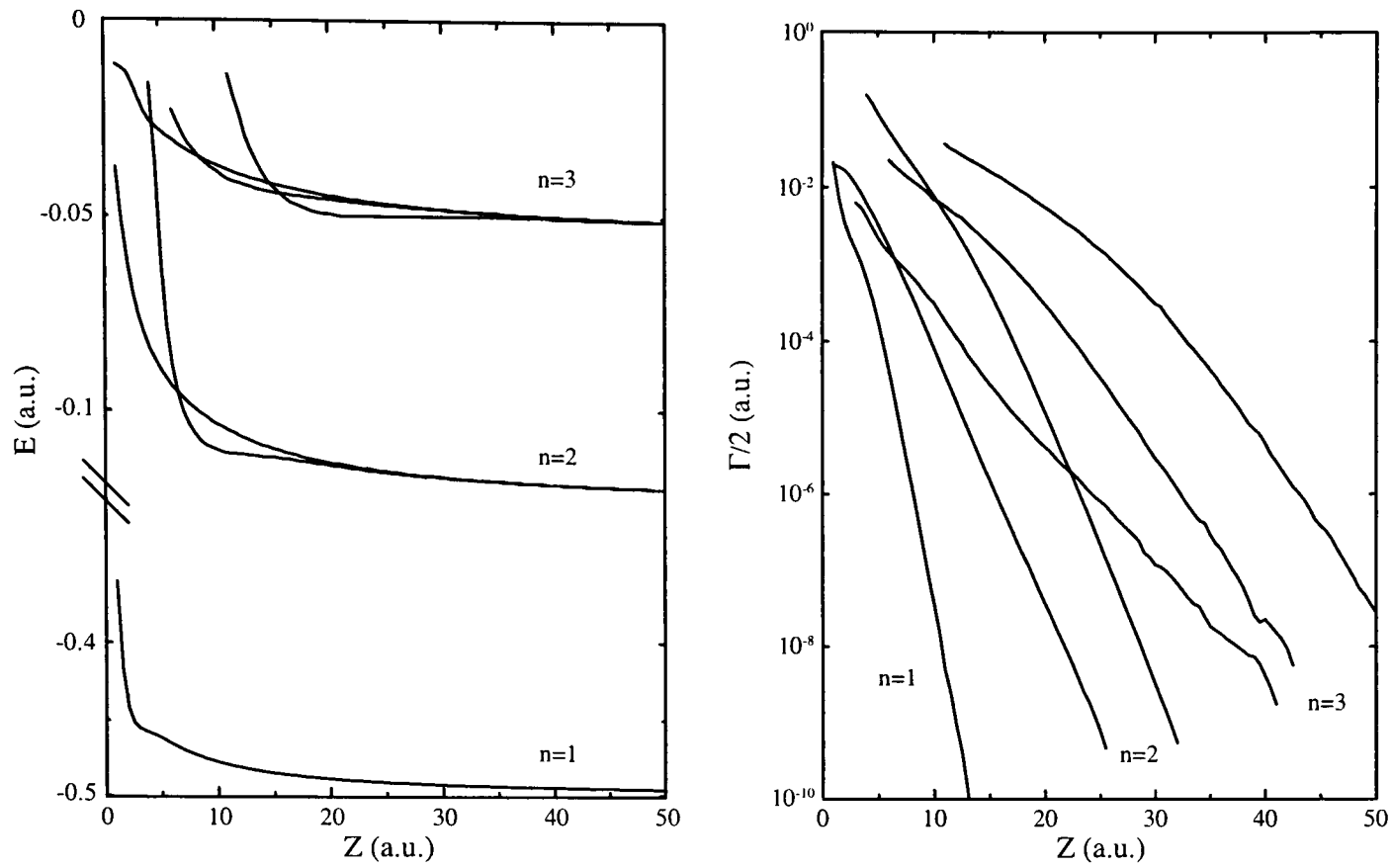

Figure 2.8: *Calculated energies (left) and associated half-widths (right) for the three $n = 3, m = 0$ hydrogen Rydberg states in front of a jellium (aluminium) surface. Z is the core-surface separation. Note some numerical instability is present in the $n = 3$ lifetime data.*

2.3 Ion production rates as a function of separation

Although the calculation of the energy of a state at a given separation from the surface is interesting it is the linewidth data that is of most importance in simulating any experimentally observed ionisation. The full linewidths can be related to the rate of ionisation by

$$\frac{\mathrm{d}n_i(t)}{\mathrm{d}t} = -\Gamma_i(t)\, n_i(t) \qquad 2.25$$

where $n_i(t)$ is the instantaneous population of a state i at a time t and $\Gamma_i(t)$ is the calculated linewidth of that state at that time. This can be rewritten in terms of molecule/surface separation, following application of the chain-rule, such that

$$\frac{\mathrm{d}}{\mathrm{d}Z} n_i(Z) = \frac{\Gamma_i(Z)}{v_\perp}\, n_i(Z)\,. \qquad 2.26$$

In this case, $\Gamma_i(Z)$, is the linewidth calculated as described in Section 2.2 while $v_\perp$ is the perpendicular velocity of the molecule. It follows that the rate of ion

production at a given molecule/surface separation, $P_i(Z)$ is given by

$$P_i(Z) = \frac{\Gamma_i(Z)}{v_\perp} \exp\left(\int_\infty^Z \frac{\Gamma_i(Z')}{v_\perp} dZ'\right). \qquad 2.27$$

Throughout this discussion a value of $v_\perp = 1.41217 \times 10^{-4}$ ms^{-1} will be used which represents a particle with a mean velocity 2535 ms^{-1} and incident on the surface at 7°. These values are typical of the molecule beam used in the experiment as detailed in Section 4.1.2. While it must be remembered that the Rydberg states are actually being modelled as a hydrogen atom, the inclusion here of a velocity characteristic of molecular hydrogen is crucial in relating the calculated linewidths to the experimental observations.

Applying Equation 2.27 to the linewidth data calculated for the two $n = 2$, $m = 0$ states in the range $Z = 2 - 50$ atomic units yields the profiles of ion production as a function of molecule/surface separation shown in Figure 2.9(a). It is evident that each state exhibits a different ionisation behaviour and this is associated with the very different widths exhibited by each of these $s - p$ hybridised states (see Figure 2.6). However, if the $n = 2$ states are excited at zero field there is likely to be branching between these initially degenerate states such that both levels in Figure 2.6(a) are populated. When extending to higher n, the total ion production rate across all n hybridized states is a more useful simulation. Integration of the total ion production rate information yields a curve which represents

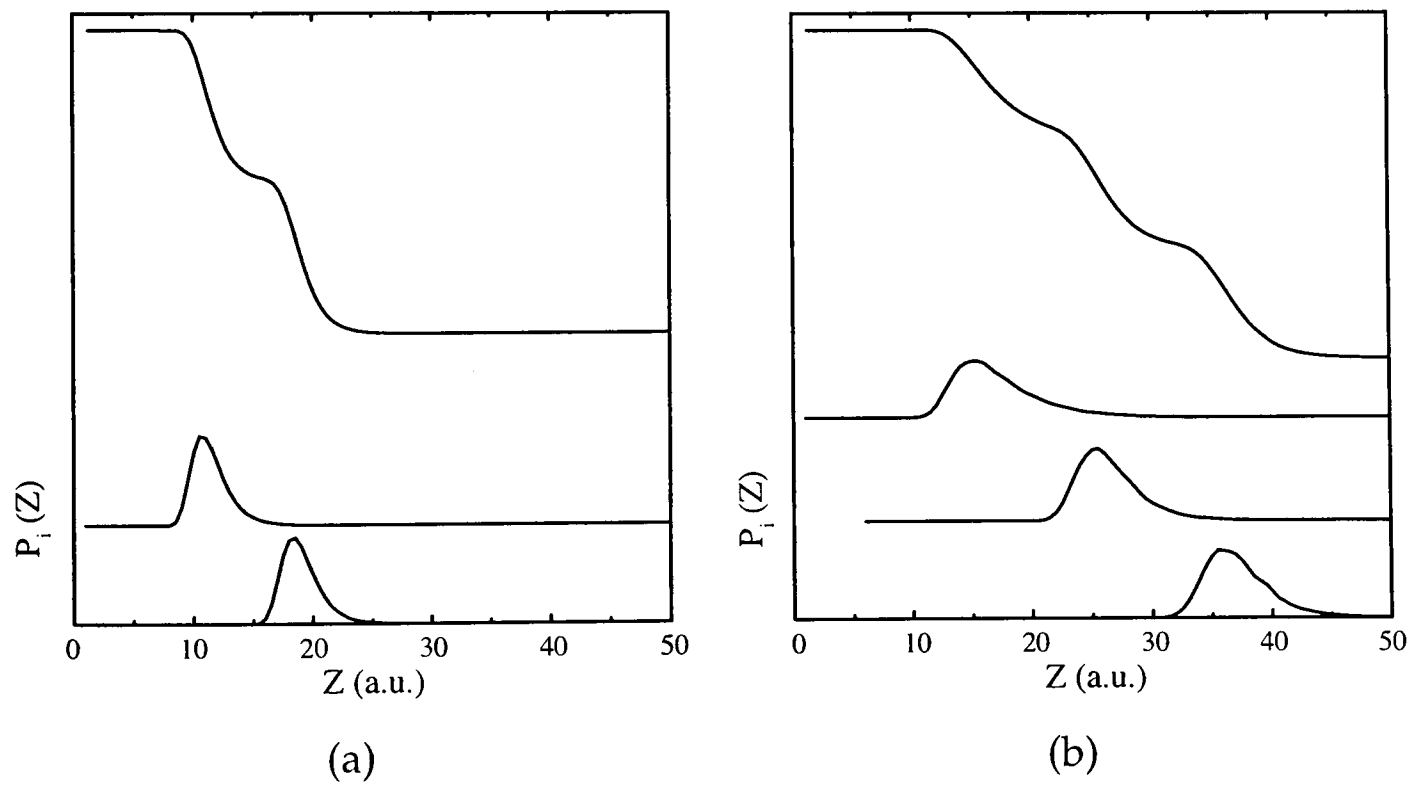

Figure 2.9: *Calculated ion production rates for (a) the two $n = 2$, $m = 0$ states and (b) the three $n = 3$, $m = 0$ states of hydrogen. The uppermost curve in both figures is the cumulative ion production as a function of molecule/surface separation.*

the proportion of the total population that has ionised by the time the molecular beam has reached a given distance from the surface.The uppermost curve in Figure 2.9(a) shows the Z dependence of this total ion production for a molecular beam in which each of the $m = 0, n = 2$ states are equally populated. An analogous set of results for the $n = 3$ states is also presented in Figure 2.9(b). A comparison of the two cumulative ion populations suggests that the molecule/surface separation at which ionisation will occur should be strongly dependent upon the principal quantum number, n. The nature of this relationship is discussed further in Section 2.4.3.

2.4 Extension of the model to states of higher n

2.4.1 Energies and linewidths

In principal the method of complex scaling can be used to calculate the energy and linewidth of any state required. In order to extend the model, however, it is important to include sufficient basis functions such that the position of a resonance for a given state is converged. The results shown so far for states with principal quantum number $n = 1, 2$ or 3 have all required at least 100 basis functions to be included in the calculation to ensure convergence of the eigenvalues. The calculation has been extended to states with $n = 6, 7, 8$ and 9. In these cases the basis set was constructed using the parameters $l_{max} = 19$ and $N_l = 20$ to ensure convergence, giving a total of 400 basis functions. While computationally more expensive than the calculations at lower n, the eigenvalues associated with such states are still readily calculable and the results are presented in Figure 2.10.

However, for the calculation of the energies and linewidths for states with principal quantum number greater than $n = 10$ a significant increase in the number of basis functions is required to adequately represent the form of the wavefunction and to ensure convergence of the eigenvalues. The problems associated with this are discussed in Section 2.4.3.

At this point a discussion of the nature of the energy shifts seems appropriate as several interesting features are visible in Figure 2.10, although it is important to remember that these are relative shifts as the attractive interaction between the ion core and its image charge is ignored in the calculation of the potential function (see Section 2.2.2). As the surface is approached the degeneracy of the states associated with a given principal quantum number is lifted. As stated in Section 2.2.4 the matrix which yields the eigenvalues is diagonal with respect to the azimuthal

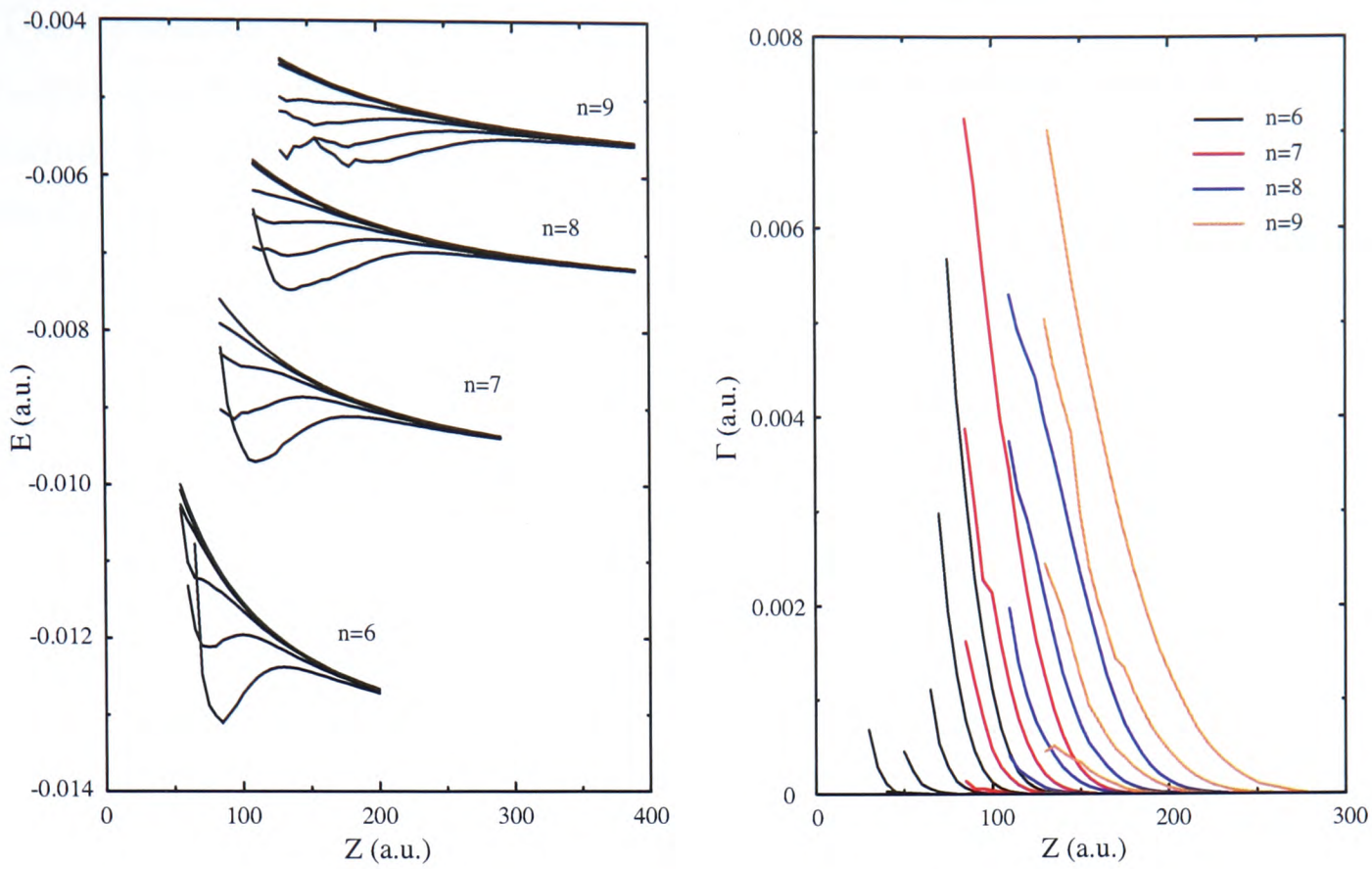

Figure 2.10: *Calculated energies (left) and associated half-widths (right) for hydrogen Rydberg states with $n = 6 - 9$, as labelled in the figure, in front of a jellium (aluminium) surface. Z is the core-surface separation.*

quantum number m. Therefore, for each m and n there are $n - |m|$ degenerate orbitals that may hybridize with each other. At large separations, where the electron-core image interaction dominates, the surface potential is repulsive (see Figure 2.3) and all states shift upward with decreasing Z. However, when the wavefunction extends into the region where the potential is attractive, that is where the electron-electron image interaction dominates, a downward shift in energy is observed. This effect is seen at a greater separation for those states whose wavefunctions are oriented toward the surface (the red-shifted states). Finally, at sufficiently small separations all states shift upward. This is due to the fact that the electron-core image potential once again dominates at small values of Z, a consequence of the fact that the electron-core image potential is dependent upon both the nuclear (Z) and the electron (z) coordinate whilst the electron-electron image is dependent solely on the electron coordinate. Another point worth noting is that as the value of n increases so too the energy separation between adjacent manifolds of states decreases. Consequently, at sufficiently high principal quantum number energy levels associated with states of different principal quantum number will interact. For non-hydrogenic systems these interactions would be manifested as avoided crossings.

The variations in linewidths exhibited by the states associated with the same principal quantum number can also be understood in terms of the electron distribution. For a hybridised state whose electron distribution is largely oriented towards the surface (the red-shifted states), interaction with the surface electron density begins to occur at a greater molecule/surface separation. The opposite is true for the blue-shifted states which have an electron distribution oriented towards the vacuum. Consequently the red-shifted states exhibit much greater broadenings than their blue-shifted counterparts. The fact that the interaction with the surface begins at a different separation as the principal quantum number is varied can be understood by considering the spatial characteristics of the Rydberg state. For higher principal quantum numbers the extent of the radial wavefunction increases and so it is expected that interaction with the surface will occur at a great separation. This is clearly shown in Figure 2.10.

2.4.2 Ion production rates

As described in Section 2.3 it is feasible to use the calculated linewidth data to simulate the cumulative ion production as a beam of molecules approaches the surface. Using the data presented in Figure 2.10 the ion production profiles for states with principal quantum number $n = 6 - 9$ have been calculated. They are shown in Figure 2.11. Once again it is clear that the separation at which ionisation begins, that is the maximum molecule/surface separation at which ion production is feasible, is dependent on the principal quantum number of the state.

2.4.3 Scaling to considerably higher *n*

To this point the method first described by Nordlander *et al* has been utilised, in conjunction with the model potential detailed in Section 2.2.2, to provide accurate values of the energy shifts and linewidths of states with principal quantum number $n < 10$. Ion production rates, calculated using a velocity representative of a beam of hydrogen molecules, have also been presented. It is important, however, to calculate predictions of the outcome of the experiments performed.

The experimental investigations presented in Chapter 4 involve Rydberg molecules initially excited to states with principal quantum numbers in the range $n = 17 - 22$ (for the $N^+ = 2$ states) and $n = 41 - 45$ (for the $N^+ = 0$ states). Consequently it would be advantageous to extend the model to produce ionisation simulations for these states. However, such an extension would require a

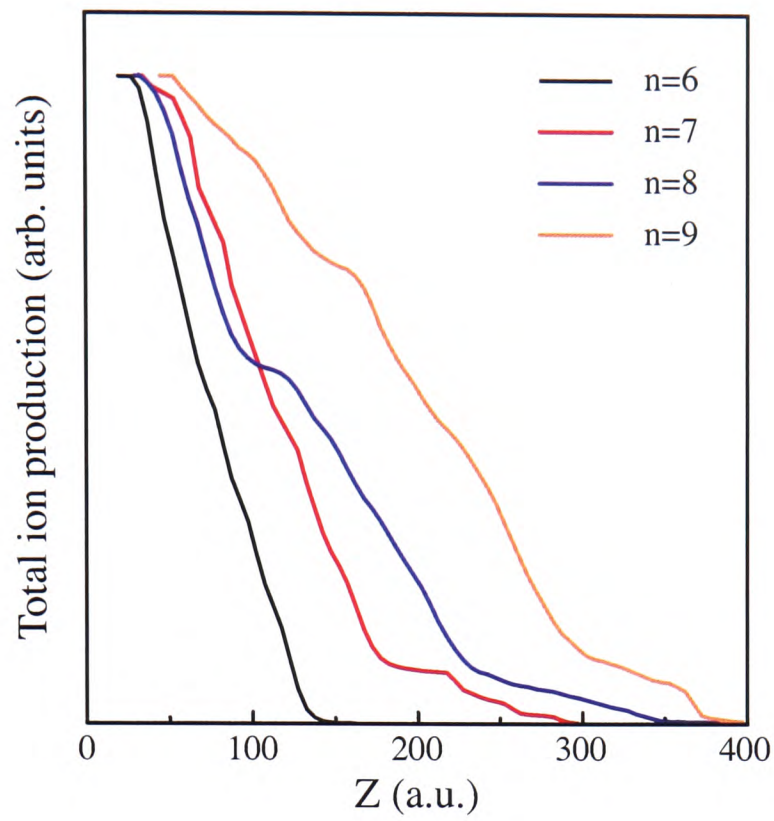

Figure 2.11: *Calculated total ion production as a function of surface separation for principal quantum numbers $n = 6 - 9$, using the hydrogenic model.*

dramatic increase in the number of basis functions as alluded to in Section 2.4.1. This arises from the need to include a greater number of energy levels in the calculation to ensure convergence of the complex eigenvalue problem. As such, we are presented with two major problems. Firstly, as the number of basis functions increases so too does the size of the matrix that must be diagonalized. While matrices of dimension 400 are easily handled, the diagonalization of a 4000×4000 complex matrix, a size that is appropriate for calculations of $n = 17 - 22$ eigenvalues, is computationally very expensive. Secondly, the individual matrix elements are calculated efficiently by way of Gaussian quadrature. As the value of the principal quantum number increases so too does the number of nodes in the radial wavefunction. Similarly the number of nodes in the angular wavefunction increases with the angular momentum quantum number l. Consequently a denser grid is required to accurately integrate the wavefunctions and again this is computationally expensive.

An alternative route, which provides an estimate of the ionisation profiles, can be pursued by scaling the low n data already calculated. While this does not provide a complete set of energies and linewidths for the individual states it does provide the necessary information to generate a simulation of the experimental output. If the simulated data shown in Figure 2.11 is scaled by a factor of $1/n^2$ then the ionisation curves associated with different principal quantum

numbers all appear to behave in a broadly similar way. The result of the scaling is shown in Figure 2.12. It can be seen that the onset of ionisation occurs at a molecule/surface separation, Z, of approximately $4n^2a_0$ which is in good agreement with the previously determined value of $3.8n^2a_0$ reported in [13]. It is also apparent that the profiles for $n = 7, 8$ and 9 exhibit a shallow tail at large separations. Such a feature indicates that at these larger separations some states are already, albeit to a smaller degree, susceptible to ionisation. Why it is not present in the $n = 6$ simulation is not known at this time.

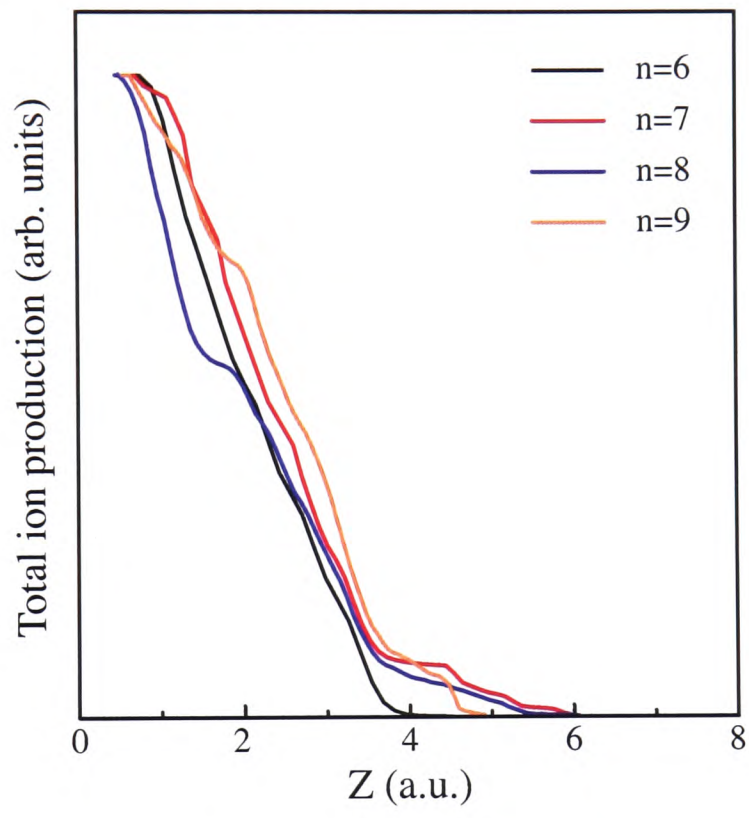

Figure 2.12: *Calculated total ion production as a function of surface separation for principal quantum numbers $n = 6 - 9$, scaled by a factor $1/n^2$.*

Therefore, taking the profile for the $n = 6$ data, which represents an average of the scaled profiles (ignoring the tails), and scaling it by a factor n^2, it is possible to generate a series of predicted profiles for high n states. The result is shown in Figure 2.13(a) for $n = 17 - 22$. It is important at this point to remember that these profiles are dependent on the perpendicular velocity of the molecules as detailed in Equation 2.27. It is also possible to calculate total ion production curves for any given spread of the population amongst the hybridised states. As expect this alters the shape of the ion production profiles generated. An example of a series of profiles for $n = 17 - 22$, assuming the population exists solely in the most red-shifted state, is given in Figure 2.13(b).

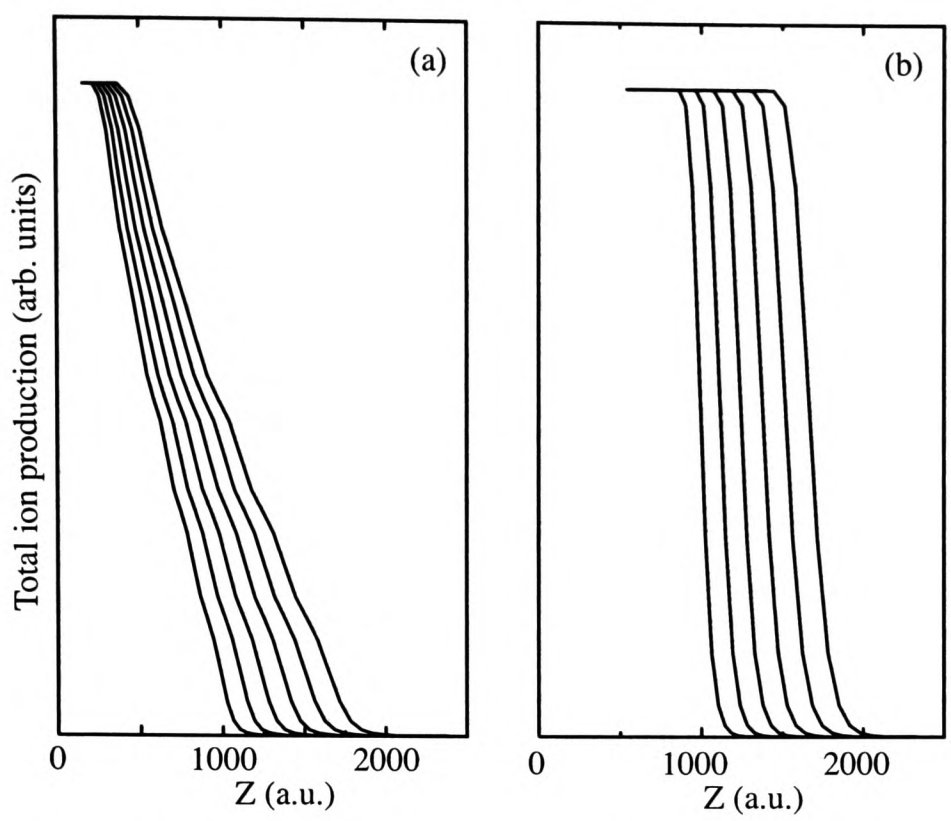

Figure 2.13: *Predicted ion production as a function of molecule/surface separation. (a) calculated assuming a population evenly spread amongst all n hybridised states. (b) calculated assuming all the population exists in the most red-shifted state. The individual curves in each figure, from left to right, represent states with principal quantum number* $n = 17 - 22$ *respectively.*

2.5 Conclusions

The work presented in this chapter illustrates that the method of complex scaling can successfully be applied to the problem of calculating energies and linewidths for particles interacting with metal surfaces. While it is clear that the calculations could be extended, with an appropriate increase in basis size, to include states with principal quantum numbers in the range $n = 17 - 22$ and $n = 41 - 45$, and therefore provide information about the energies and widths of the states investigated experimentally, such calculations have not been performed. The reasons for this are two fold. On the one hand, the simulation of the experimentally observed ionisation behaviour required solely a knowledge of the cumulative ion production as a function of molecule/surface separation. Such profiles were obtained using the scaling described above, negating the need to perform intensive calculations. On the other hand, initial experimental results suggested that molecular effects, particularly the rotation of the ionic core, had a direct influence on the ionisation behaviour. As such, the model presented here would be insufficient although it could be extended to incorporate such phenomenon. This fact is discussed in more detail in Section 4.2.9.

CHAPTER

THREE

Experimental methods

Although the interaction and ionisation of Rydberg atoms with metallic surfaces has been the subject of many previous experimental studies [9, 11, 12, 13, 15] there are no reported investigations involving Rydberg molecules. The interaction of a molecule with a surface presents new aspects to the physical problem as the molecular ion core possesses vibrational and rotational degrees of freedom and the question arises as to how these might contribute to the interaction with the surface. The details of the first observations of molecular Rydberg states interacting with metal surfaces are presented in full in Chapter 4. In the following sections a description of the experimental apparatus and detection techniques used in this investigation is given. In the latter parts of this chapter some preliminary observations are presented as well as some experimental spectra.

3.1 Excitation scheme

3.1.1 *B*-state excitation

The work presented here focuses on Rydberg states of H_2 with no core vibrational motion ($v^+ = 0$) which were accessed using the two-colour excitation scheme in Figure 3.1. Excitation of the B-state intermediate proceeds via the one-photon transition, $R\,(0)\ B\,^1\Sigma_u^+\ (v' = 0) \leftarrow X\,^1\Sigma_g^+\ (v'' = 0)$, at an energy of $90\,242.33\,\mathrm{cm}^{-1}$ [79]. This corresponds to the $R(0)$ transition which populates the intermediate $B\,^1\Sigma_u^+\ (v' = 0, J' = 1)$ level. The vacuum ultraviolet (VUV) excitation of this transition has been reported in detail elsewhere [80].

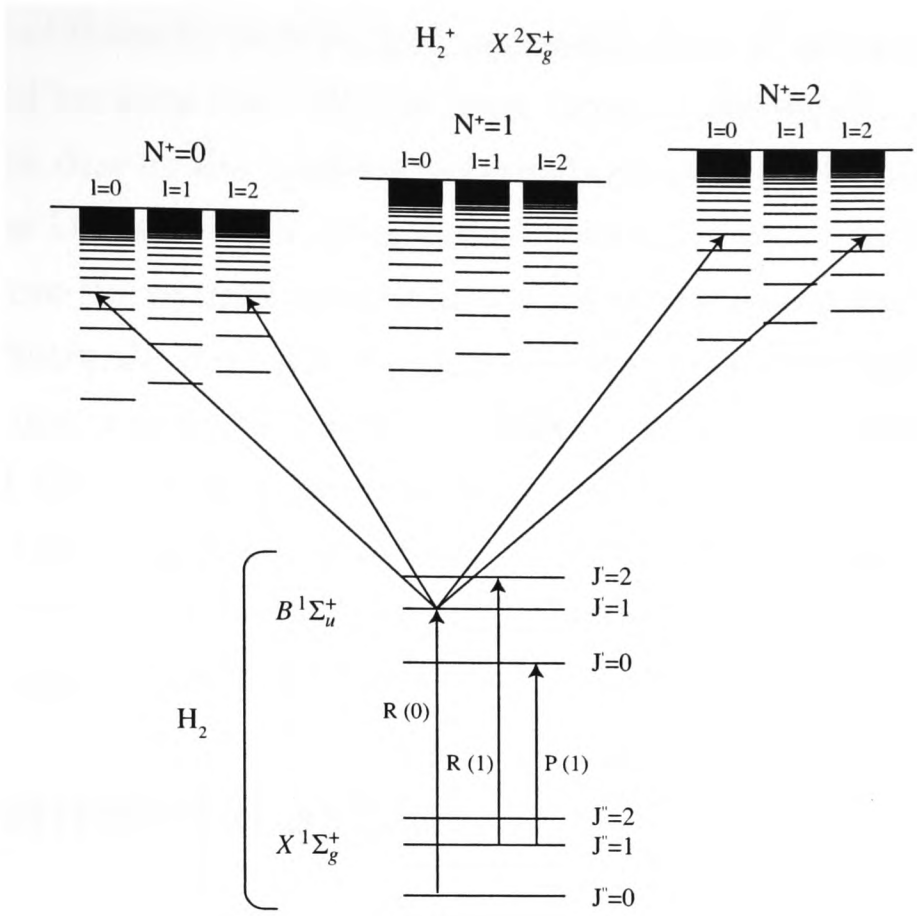

Figure 3.1: *VUV + UV doubly resonant two photon excitation scheme to excite ns/nd Rydberg states of H_2. The other, allowed, one photon transitions from the ground state to the intermediate are also shown.*

3.1.2 Rydberg state excitation

As the selected VUV wavelength leads to the population of the $J' = 1$ level of the $B\,^1\Sigma_u^+$ $(v' = 0)$ intermediate state, the process corresponds to excitation of *para*-hydrogen. Rydberg states can now be accessed by excitation from this intermediate with a single UV photon. This transition populates Rydberg series converging on the ionisation thresholds associated with the rovibrational levels $v^+ = 0, N^+ = 0$ and 2 of the $X\,^2\Sigma_g^+$ ground ionic state. The total energy of the two transitions is approximately $124\,000\,\mathrm{cm}^{-1}$ with the lowest ionisation threshold, corresponding to the $N^+ = 0$ series, located at an energy of $124\,417.507\,(18)\,\mathrm{cm}^{-1}$ [81] above the ground state. Due to the restrictions of parity in the UV transition the final states must have overall *gerade* symmetry and given the electronic symmetry of the H_2^+ ion-core is $^2\Sigma_g^+$, only the even-l Rydberg series are accessible in the UV excitation step. In reality it is primarily the *ns* and *nd* states that are populated. The $\Delta J = 0, \pm 1$ selection rule further restricts the states accessible from the $J' = 1$ level of the intermediate, allowing excitation only to states with total angular momentum $J = 0$, 1 or 2. As a result there are seven series accessible from the intermediate level populated, $B\,^1\Sigma_u^+$ $(v' = 0,\ J' = 1)$. Using Hund's case (d) notation these are $(ns0)_0$, $(ns2)_2$, $(nd0)_2$, $(nd2)_0$, $(nd2)_1$, $(nd2)_2$ and $(nd4)_2$. Al-

though the last of these is, in principle, accessible the transition intensity for such a process would be very low. Of the other series theoretically accessible further restrictions arise due to the relative polarisations of the two laser beams. In the experiments the UV and VUV laser polarisations are set to be mutually perpendicular. Therefore the overall selection rule for the two-step excitation must have $\Delta M_J = \pm 1$, arbitrarily defining the quantisation axis with respect to one of the laser polarisations, a definition which is valid at zero field. Given the initial state has $J'' = 0$ and $M_J'' = 0$, then the final states must have $M_J = \pm 1$. Consequently the final-state total angular momentum must be greater than zero, i.e. $J > 0$. Hence transitions to the $(ns0)_0$ and $(nd2)_0$ states are forbidden. The excitation spectra are discussed further in Section 3.3.

3.2 Experimental setup

A schematic diagram of the laser system and molecular beam apparatus is provided in Figure 3.2. A more detailed diagram, depicting the geometry of the surface and detection system, is shown in Figure 3.3.

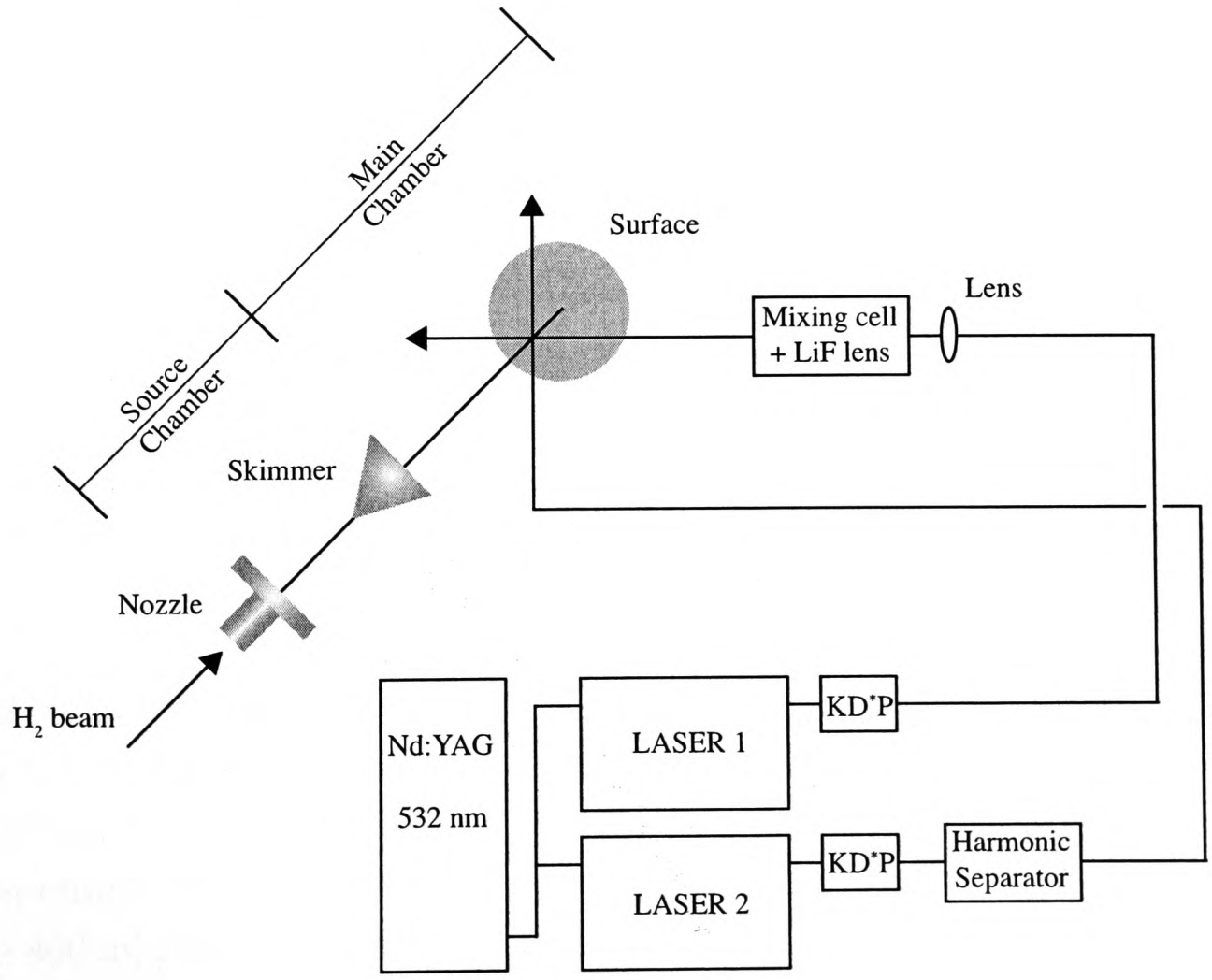

Figure 3.2: *Schematic diagram of the laser system and vacuum apparatus.*

3.2.1 Vacuum and molecular beam apparatus

The vacuum apparatus consists of a two-stage differentially pumped vacuum system used to produce a well collimated supersonic molecular beam of ~ 200 μs duration. Hydrogen gas (BOC 99.99%) at a backing pressure of 2 bar was introduced into the source chamber through a pulsed valve (General Valve Series 99) operating at 10 Hz. The pulsed valve was triggered such that it opened $\sim$ 210 μs before the laser fired to ensure that the excitation volume was in the front portion of the gas pulse. The vacuum in the source chamber was maintained at $\sim 8 \times 10^{-5}$ mbar throughout operation by a turbomolecular pump (Leybold 620 ls^{-1}) backed by a rotary pump (Edwards EM series). The central part of the molecular beam then passed into the main chamber through a skimmer (Beam Dynamics Inc.) of 1 mm diameter located 3 cm from the opening of the pulsed valve. Both the pulsed valve and the skimmer were mounted such that the resulting, collimated beam was incident on the horizontally mounted metal surface at an angle of $\sim 7°$. The molecular beam was then intersected by two laser beams in the centre of the main chamber 170 mm from the skimmer face. The base pressure in the main chamber was $\sim 8 \times 10^{-8}$ mbar rising to $\sim 1 \times 10^{-6}$ mbar during operation of the pulsed valve. This was achieved using a second rotary/turbomolecular pump system (Leybold 600 ls^{-1}/Edwards EM series).

3.2.2 Laser system

Excitation to the Rydberg states of interest required the use of two different laser beams in a VUV-UV doubly resonant excitation process. The laser beam which facilitated the single photon $B\,^1\Sigma_u^+ \leftarrow X\,^1\Sigma_g^+$ transition ($\lambda = 110.81$ nm) was generated by non-resonant frequency tripling of UV laser radiation in a mixture of krypton and argon gases (BOC special gases 99.9%). The UV radiation was provided by frequency doubling the fundamental output of a dye laser (laser 1). This dye laser (Spectra Physics PDL-3) was operated using a mixture of DCM and LDS 698 laser dyes in the ratio 10:1, in the oscillator and preamplifier cells, and pure DCM in the amplifier. It was pumped using the second harmonic output of an Nd:YAG laser (Spectra Physics GCR 290) which provided $\sim$ 800 mJ per pulse at a repetition rate of 10 Hz and pulse length of 9 ns. The output was split such that $\sim$ 400 mJ pumped both laser 1 and laser 2 (see below). The output of the dye laser was then frequency doubled by passing it through a KD^*P crystal and the residual fundamental separated using a Pellin-Broca prism. In optimal conditions

$\sim$ 6 mJ per pulse of UV radiation ($\lambda = 332.42$ nm) was produced by this process. Frequency tripling was achieved via a non-linear process in which the UV laser beam was focused, using a 200 mm focal length lens, into a stainless steel cell containing the Kr/Ar gas mixture. The VUV radiation generated in the focus was subsequently refocused into the main chamber by a lithium fluoride (LiF) lens ($f = 70$ mm at 110 nm). The intensity of the third harmonic wave is dependent on the ratio of the gases in the mixture and previous work [57] together with trial and error suggested that a mixture consisting of argon and krypton in the ratio 200:1080 mbar resulted in the greatest conversion for the wavelength required. It should also be noted that, although there was no way to separate the residual UV from the VUV in this experiment, the refractive index of the LiF lens meant that the VUV was focused at the excitation point whereas the UV was not.

Further excitation from the $B\,^1\Sigma_u^+$ state to the Rydberg states was achieved using the frequency doubled output of another dye laser (Spectra Physics PDL-3) which was pumped using the output of the same Nd:YAG laser that was used to pump laser 1. This dye laser (laser 2) was operated using Rhodamine 610 dye and the fundamental radiation was doubled using a KD*P crystal. Any residual fundamental radiation was separated using an harmonic separator (Inrad). The resulting UV radiation ($\sim$ 7 mJ per pulse), tunable in the range 291–296 nm, entered the main chamber horizontally and perpendicularly to laser 1. This beam was not focused. It was necessary at times to scan laser 2 during the course of the experiment and in this case the optimum angle of the KD*P crystal was maintained using an auto-tracker (Inrad Auto-tracker II). By using the same pump laser for both dye lasers and adjusting the individual path lengths of the laser beams it was possible to achieve temporal synchronisation between the VUV and UV pulses which was essential for efficient population of the Rydberg states due to the short lifetime of the $B\,^1\Sigma_u^+$ intermediate.

3.2.3 The excitation region

The configuration of the apparatus within the main chamber and the alignment of the laser beams, with respect to each other and the molecular beam, is shown in figure Figure 3.3. The arrangement is such that excitation from the ground state to the Rydberg states occurred above the sample surface. Both laser beams entered the chamber at right angles to one another and intersected the molecular beam at 45° in a region of spatially homogeneous electric field between the metal surface and a mesh grid electrode (81% transmitting Ni mesh, 90 lines per inch).

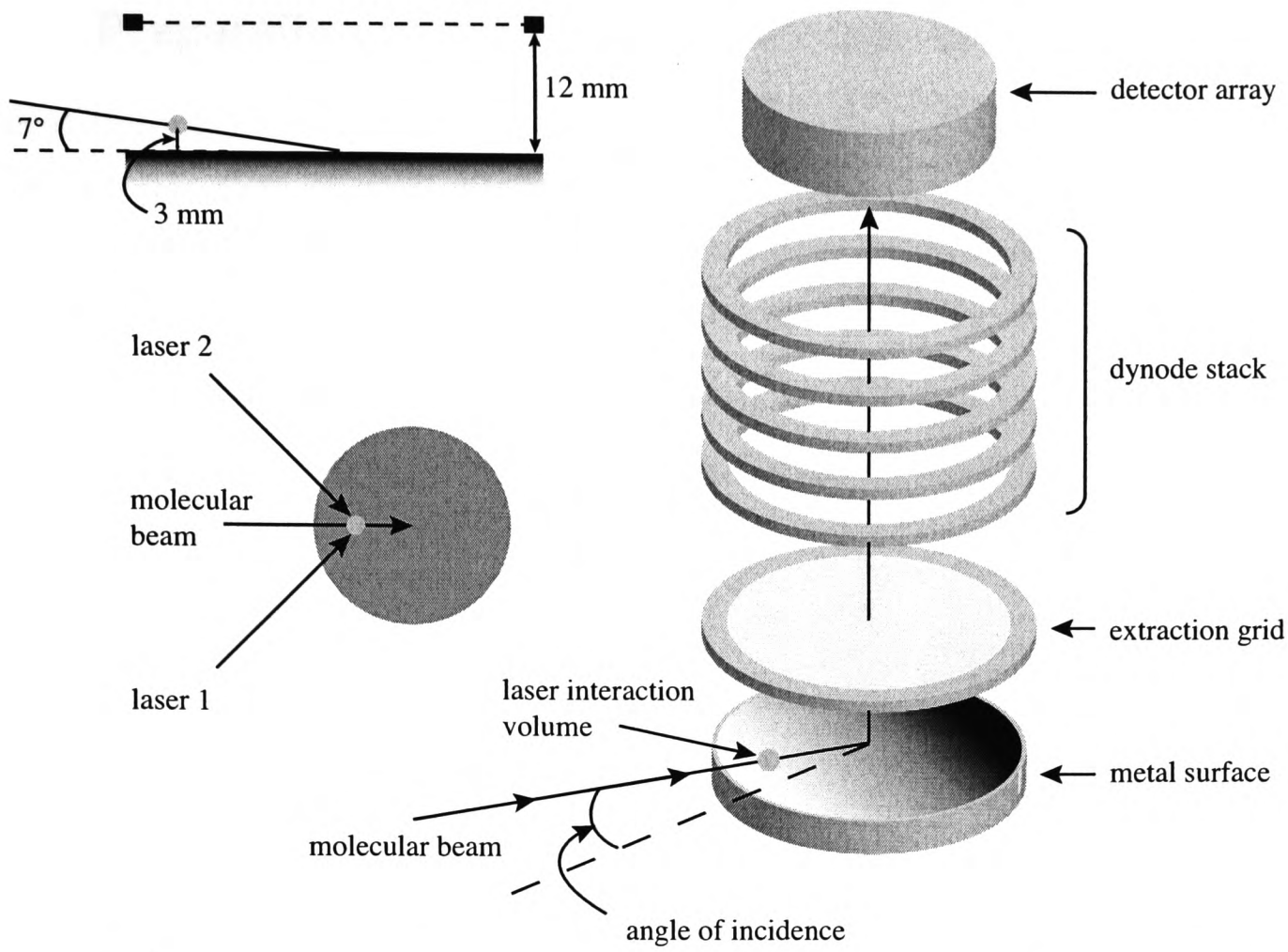

Figure 3.3: *Schematic diagram of the experimental apparatus showing the geometry of molecular beam and laser beam intersection in the region between the surface and the extraction grid. The measurements shown represent the normal position of the components.*

The surface itself was mounted on a precision translation stage (National Aperture Inc, model MM-3M-ST) allowing micro adjustment of its vertical position to a resolution of 0.124 μm. Typically this was chosen so that excitation occurred 3 mm above the surface and the surface/mesh separation was 12 mm. As mentioned previously, the excitation point is approximately 170 mm from the skimmer orifice. In all the experiments described here pure H_2 was used (backing pressure 2 bar) resulting in a molecular beam travelling with a mean velocity of 2535 ms^{-1} [82]. Consequently it was expected that the central portion of the beam would collide with the surface $\sim$ 11 μs after passing through the excitation region.

In the majority of the experiments reported here excitation occurred in near zero field conditions although a small negative bias voltage (-10 V) was applied to the mesh electrode to remove any ions formed directly during the excitation process. In the case of investigating the behaviour of a population of the Stark energy levels it was possible to apply a large negative voltage, typically -500 V, to the mesh electrode such that excitation occurred in the presence of a field.

3.2.4 Preparation of the surface

Three different metal surfaces were used in the experiments. The specific details for the preparation of each surface are given below together with some topographical analysis using atomic force microscopy (AFM) which highlights the nature of the individual surfaces. In the discussion of the surface analysis the following three parameters are assigned:

- RMS(Rq), the root mean square average of height deviations taken from the mean data plane calculated using

$$\sqrt{\frac{\sum Z_i^2}{N}}. \tag{3.1}$$

- Ra, the arithmetic average of the absolute values of the surface height deviations measured from the mean plane

$$\frac{1}{N}\sum_{j=1}^{N}|Z_j|. \tag{3.2}$$

- Rmax, the maximum vertical distance between the highest and lowest data points in the image.

Surface	RMS(Rq)	Ra	Rmax
Blank Si	0.131	0.081	1.92
Al^1 (200)	1.857	1.468	10.486
Al^1 (500)	1.819	1.418	12.9
Au (200)	0.420	0.336	2.778
Au (500)	0.620	0.597	4.155
Au (1000)	1.390	0.768	19.072
Al^2 (black)	608.8	280.4	8473.4
Al^2 (red)	290.3	231.9	1752.3
Al^2 (blue)	272.3	219.1	1734.9

Table 3.1: *Surface parameters obtained by analysis of the AFM images, for all three surfaces, the deposited gold* Au, *and aluminium* Al^1, *and the machined aluminium* Al^2. *All values are in nm. The numbers in brackets refer to the sample size analysed while the colours relate to the profiles in Figure 3.8.*

Deposited aluminium disc

This was prepared on a three inch polished Si (100) wafer (Compart technologies) by metal vapour deposition in a BOC Edwards Auto 306 vacuum coater with Cryo-pumping system (giving a base pressure of 2×10^{-7} mbar). The wafer was cleaned prior to the deposition, in-situ, using an oxygen discharge for 10 minutes. Parameters from AFM analysis of this clean wafer are given in Table 3.1 and the AFM image is shown in Figure 3.4. The aluminium (99.999%, Advent Research Materials Ltd.) was then evaporated from an alumina coated molybdenum boat (R. D. Mathis, Long Beach, CA), using a 3.2 V 300 A power supply. The current was controlled so that the rate of deposition on the sample was maintained at $\sim$ 1 nm/s, monitored using a quartz crystal microbalance (FTM5 thickness monitor, BOC Edwards) which was mounted adjacent to the wafer, both 120 mm from the aluminum source. During the evaporation the wafer was rotated at approximately 5 rpm and the pressure was kept below 1×10^{-6} mbar at all times. The evaporation was stopped once the film thickness had reached 100 nm, again monitored using the quartz microbalance, and then the system was allowed to cool to room temperature before venting and removing the coated wafer. Owing to the reactivity of aluminium, an oxide layer forms immediately on venting. It is thought this layer will be in the region of $1 - 2$ nm thick.

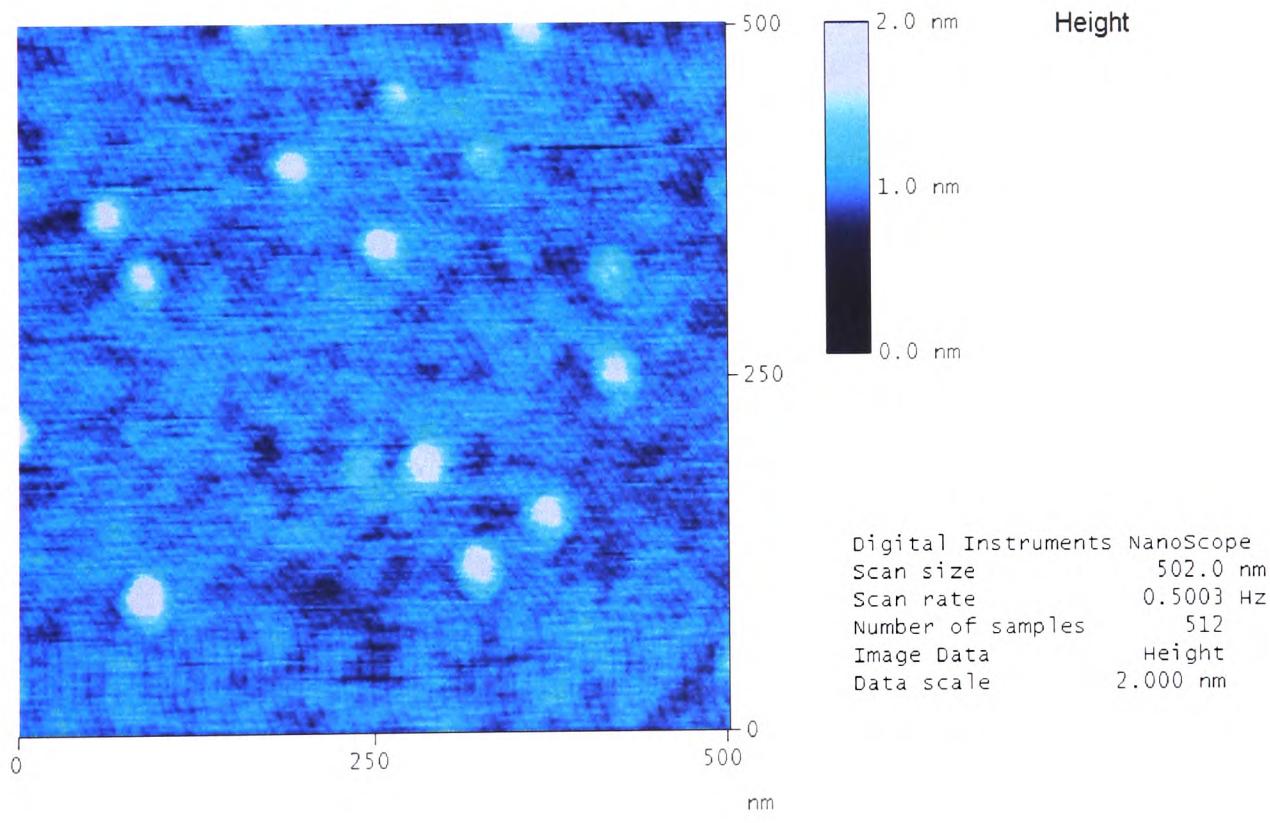

Figure 3.4: *An image of the clean Si(100) wafer recorded, for a 500 nm sample, using AFM techniques as described in the text.*

The surface topography was characterized by using an atomic force microscope (Digital Instruments, Multimode SPM) operated in tapping mode using a NST-NCHF-R silicon probe (Nascatec Technologies GmbH) and an 'E' scanner. Surface images were recorded for samples of dimension 200 nm and 500 nm. Both the 3D and flattened images for the 500 nm sample are shown in Figure 3.5 while Table 3.1 lists the parameters extracted by analysis of the images from both of these sample sizes. Very similar results are obtained in each case. It is immediately obvious that the variation of surface height is significantly smaller than the Rydberg molecule radius (20 nm for $n = 20$ Rydberg states).

Deposited gold disc

In a similar fashion to the aluminium disc, this was prepared on a three inch polished silicon wafer. However, in order to give good adhesion for the gold layer, an initial 5 nm thick layer of chromium was deposited onto the silicon wafer. This was sublimed from a chrome plated tungsten rod (R. D. Mathis, Long Beach, CA) using a 10 V, 90 A power supply. The gold (99.99%, Alfa) was then deposited in an identical manner to the aluminium.

The surface topography was again characterized using AFM techniques as above for the aluminium. The recorded images for samples sizes of 200 nm and 500 nm are shown in Figure 3.6. A third sample of 1 μm was also recorded and both flattened and 3D images are shown for this sample in Figure 3.7. The parameters obtained by analysis of these images are listed in Table 3.1. The final data set, for the 1 μm image, shows a significantly increased roughness and this can be attributed to a surface defect which is evident in the 3D image (see Figure 3.7). However even including this data set the mean surface roughness, Ra, is less than 1 nm and the gold surface can be regarded as smooth as "seen" by the Rydberg molecule.

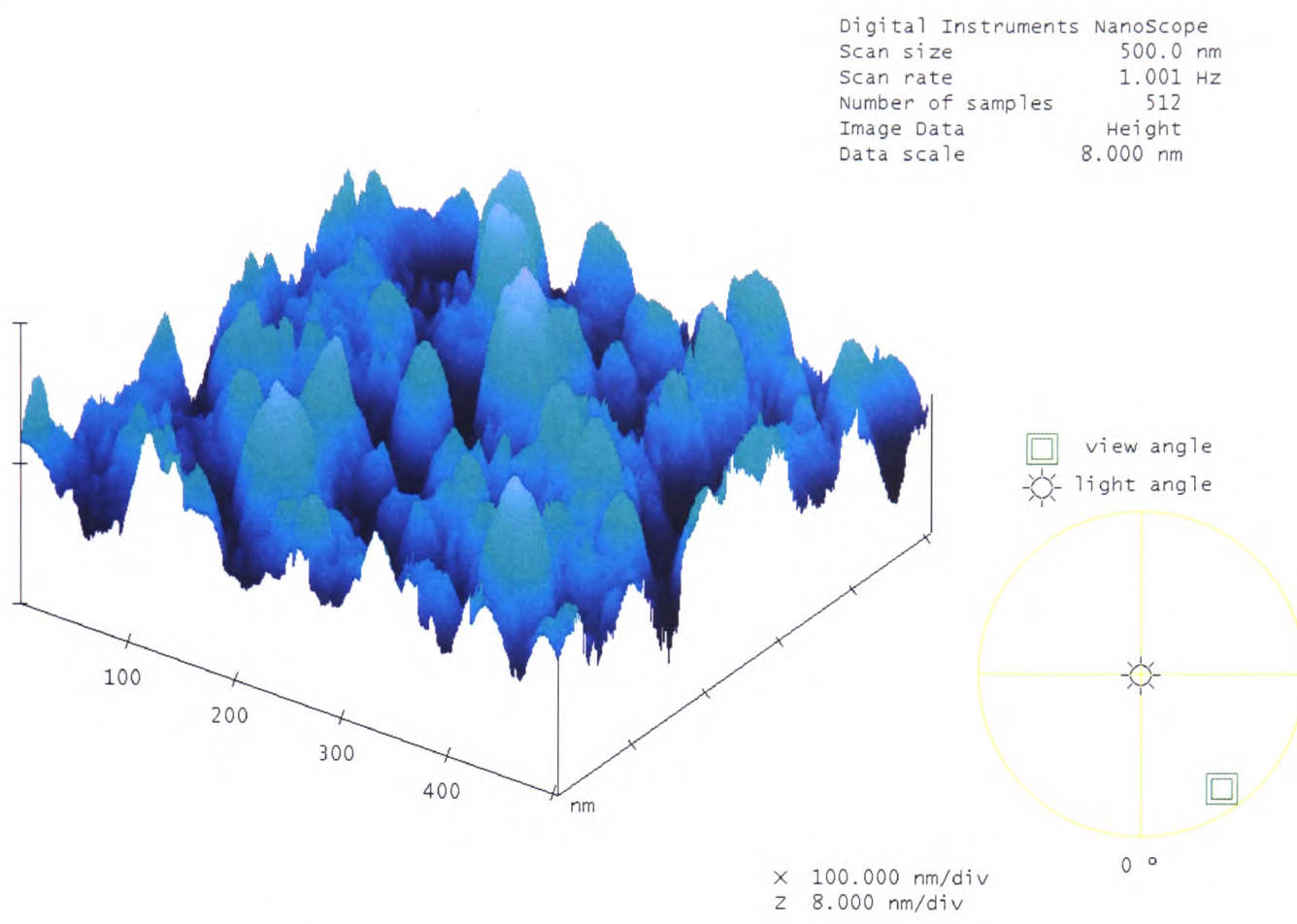

(a) 3D AFM image of the 500 nm deposited aluminium sample.

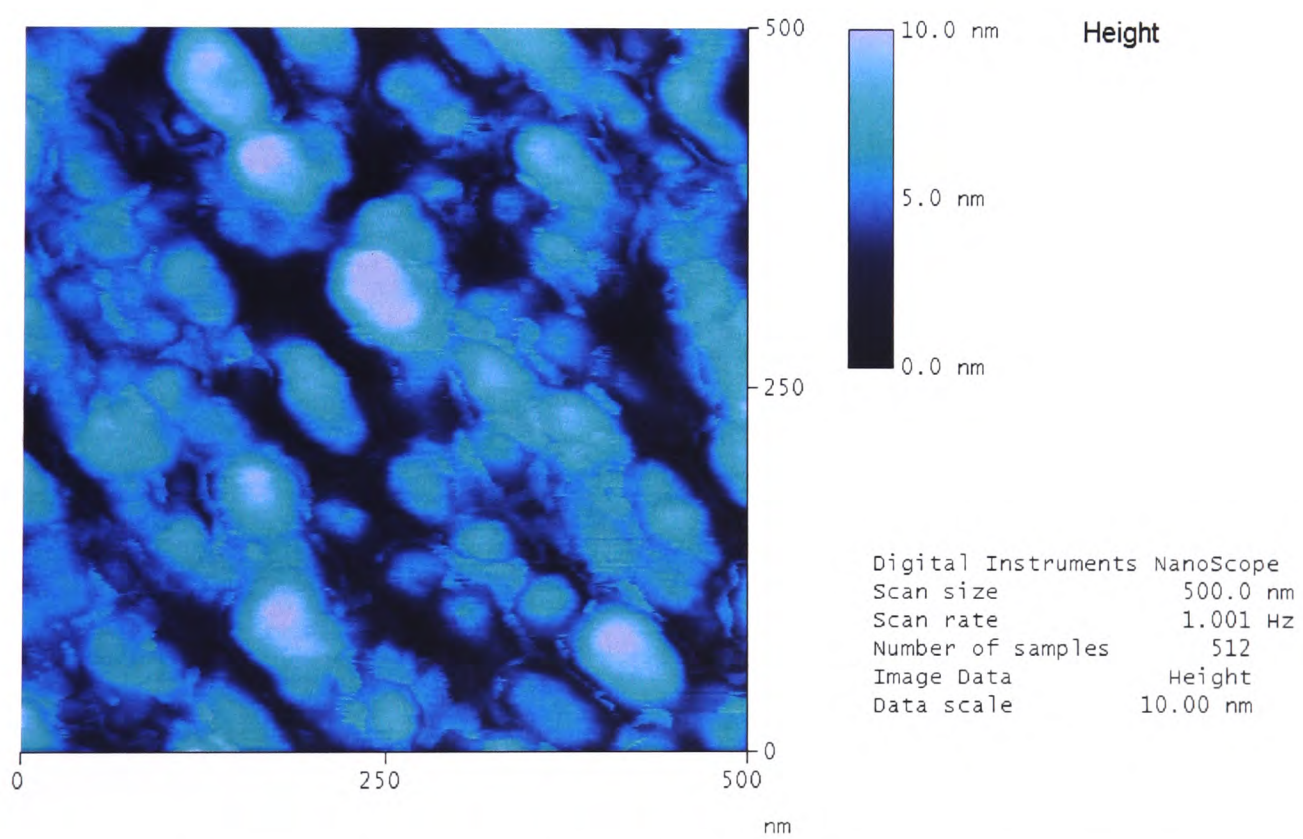

(b) Flattened AFM image of the 500 nm deposited aluminium sample.

Figure 3.5: *Surface images recorded for the deposited aluminium disc showing both the 3D image (a) and the corresponding 2D representation (b).*

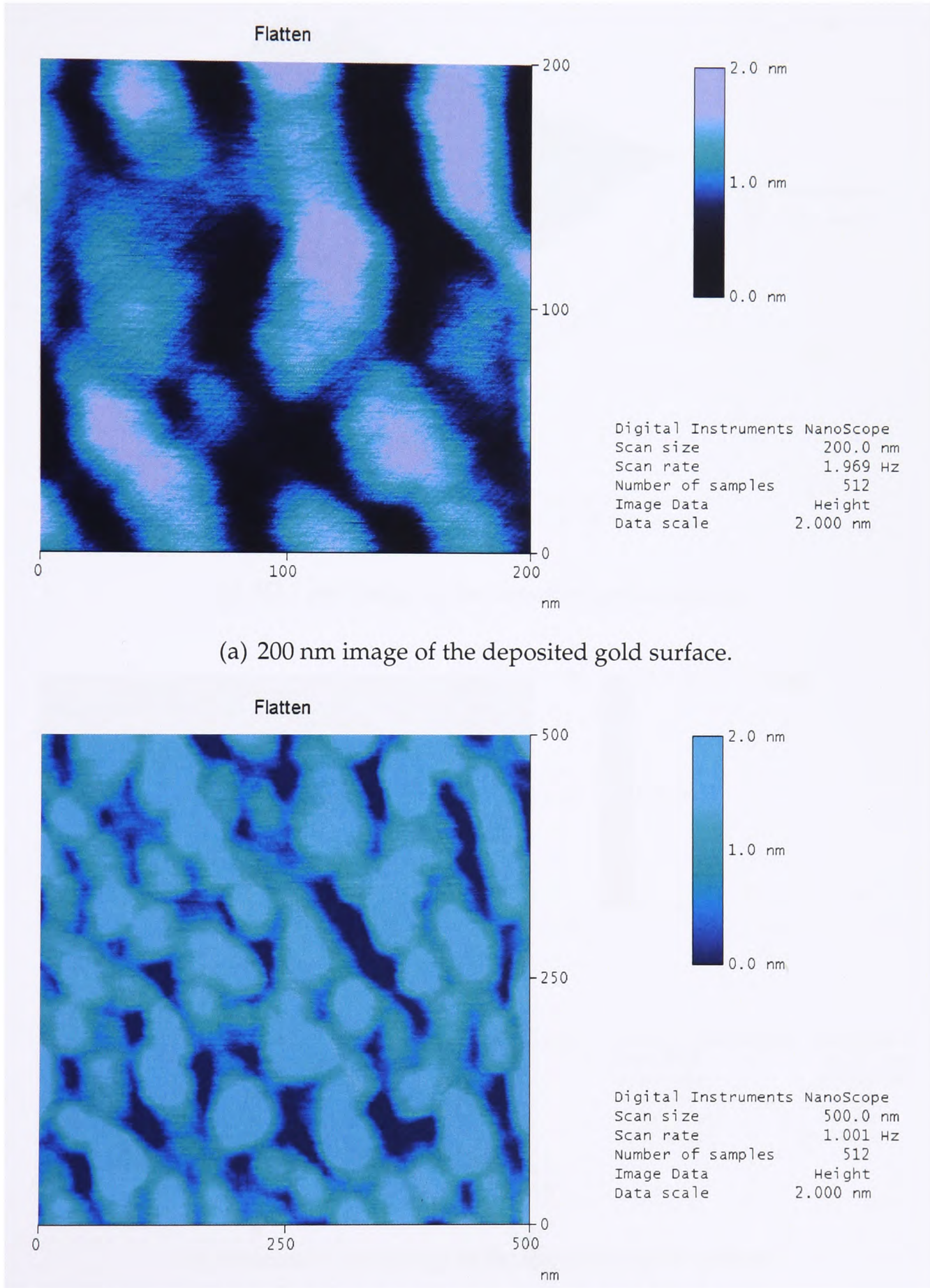

(a) 200 nm image of the deposited gold surface.

(b) 500 nm image of the deposited gold surface.

Figure 3.6: *200 nm (a) and 500 nm (b) sample scans of the deposited gold surface.*

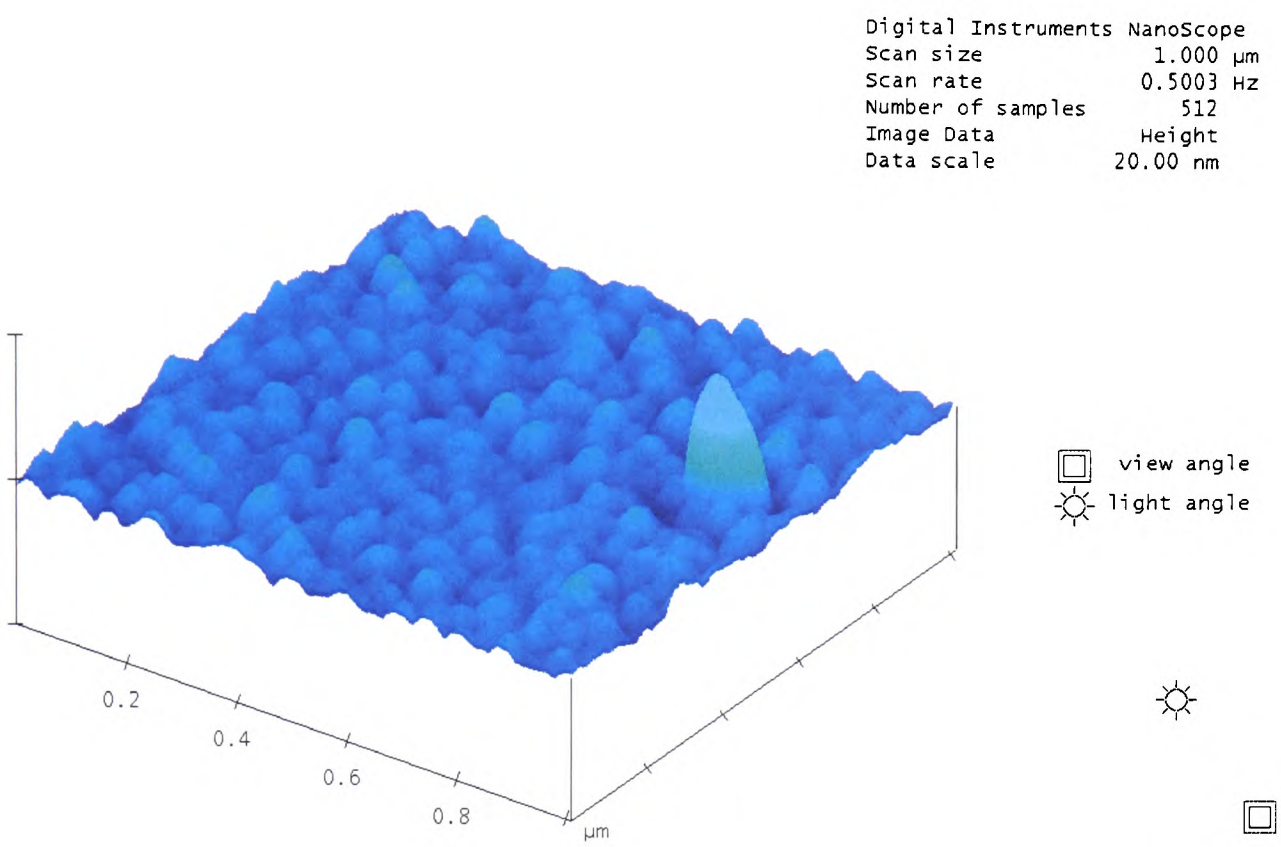

(a) 3D 1 μm image of the deposited gold surface.

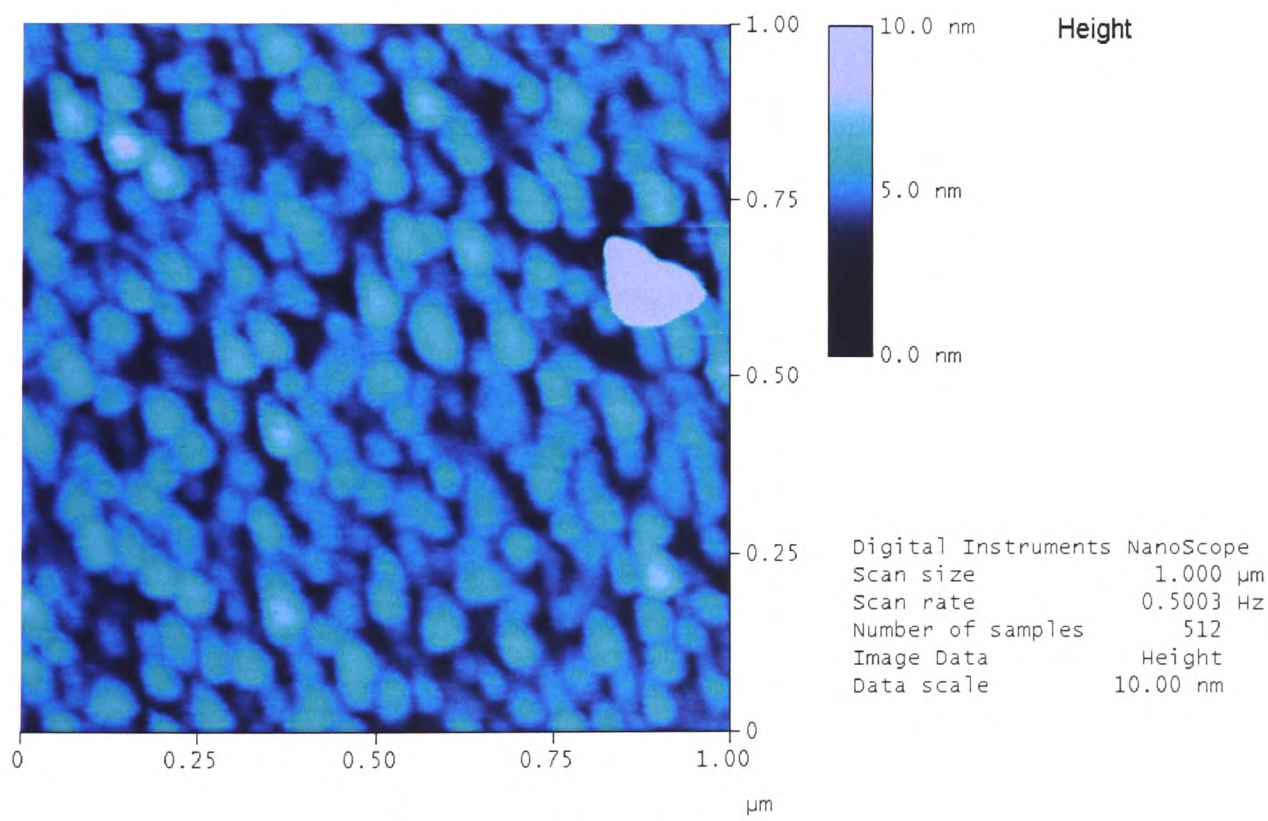

(b) Flattened 1 μm image of the deposited gold surface.

Figure 3.7: *Surface images recorded for the deposited gold disc showing both the 3D image (a) and the corresponding 2D representation (b). A large defect is clearly visible in both images.*

Machined aluminium disc

This disc, with a diameter of 50 mm, was machined from an aluminium block and polished on a lathe. The surface topography is summarised in the line profiles shown in Figure 3.8. Each profile is offset for clarity while the vertical scale indicates the extent of the deviations from the mean plane. Analysis of these profiles yields the parameters listed in Table 3.1. It is evident that the large deviation in scan 1 has had a great effect on the calculated values of both RMS(Rq) and Rmax in this instance and as such Ra is probably the best measure. In conclusion, it is sufficient to state that the Ra of the disc is approximately 230 nm but cannot be well defined due to the large, micron sized, objects present on the surface. Consequently the deviation of surface heights is significant on the scale of the molecular Rydberg radius and the surface can be regarded as rough as "seen" by the Rydberg molecule.

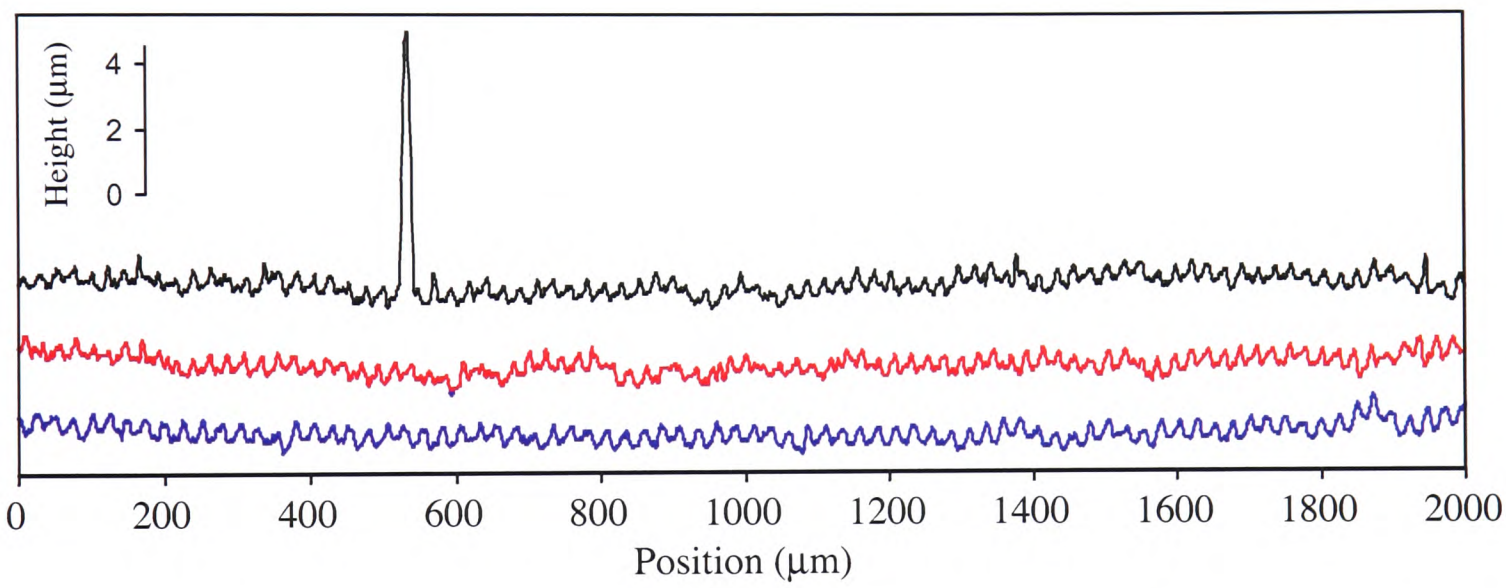

Figure 3.8: *Lines profiles recorded for the machined aluminium disc illustrating the degree of surface roughness and also the presence of significant objects on the surface. The profiles are coloured in accord with the data labels in Table 3.1 and are offset for clarity. The vertical scale is shown.*

3.2.5 Detection of H_2^+ ions

Any ions formed by tunnelling ionisation near the surface would collide with it, due to the velocity of the molecular beam, unless a field of sufficient magnitude was applied in this region to pull them away. Consequently, in order to observe any H_2^+ ions formed at the surface a large, positive, variable potential up to 5000 V was applied to the surface 800 ns after excitation. The homogeneous field generated by this potential (added to the bias on the mesh electrode) was determined

by the separation of the surface and the mesh electrode. Typically this separation was 12 mm and so the applied potentials generated fields of between $8\,\mathrm{Vcm}^{-1}$ and $4125\,\mathrm{Vcm}^{-1}$. Above a certain threshold field the H_2^+ ions were accelerated perpendicularly away from the surface through the mesh electrode. They then travelled through a flight region formed by a series of ring electrodes (dynode stack), all held at the same potential as the mesh electrode, spaced 10 mm apart. Upon leaving this region the ions reached the detector assembly. This comprised a pair of 40 mm diameter multi-channel plates (Galileo, Chevron configuration) coupled to a phosphor screen. Potentials of −1300 V, 0 V and +3500 V were applied to the front and back MCPs and to the phosphor screen respectively. The fluorescence emitted by the phosphor screen could be viewed by either a photomultiplier tube to record the total ion signal or a CCD-camera (Photonic Science, 768 × 576 pixels). By connecting the amplified output of the PMT to a digital oscilloscope, itself connected to a PC, a time-of-flight spectrum could be recorded. The image from the camera was used to record 2D spatial information via a link to PC-based image acquisition software (Photolite 3).

At high field strengths, ions were also formed in the region between the surface and the grid by a field ionisation process and not via a tunnelling mechanism. In the case of the $N^+ = 0$ states this process is direct field ionisation while in the case of the $N^+ = 2$ states the process proceeds via a field-induced autoionisation mechanism (see Section 1.4.2). From now on both these processes are refered to as direct ionisation but the it is important to remember that the actual mechanism is dependent upon the nature of the initial Rydberg state population. Although these ions reached the detector, their arrival time was significantly earlier than that of the ions formed at the surface. As a result ions produced from either process could be easily distinguished in the time-of-flight profiles. (Examples of both time-of-flight profiles and images from the camera are shown in Figure 3.9). In fact these two processes compete and, above a certain threshold field, all molecules in the region were ionised directly by the applied field. This is the case in profile (a) of Figure 3.9. Conducting the experiment in the presence of a smaller extraction field resulted in a greater proportion of molecules surviving long enough (that is not being directly ionised by the field) to reach the region where surface induced ionisation occurs. This is demonstrated by case (e) in Figure 3.9 where the majority of the ions produced were being formed by surface dependent processes. The balance between these two processes, and the conditions required to facilitate them, will be discussed in more detail in Chapter 4.

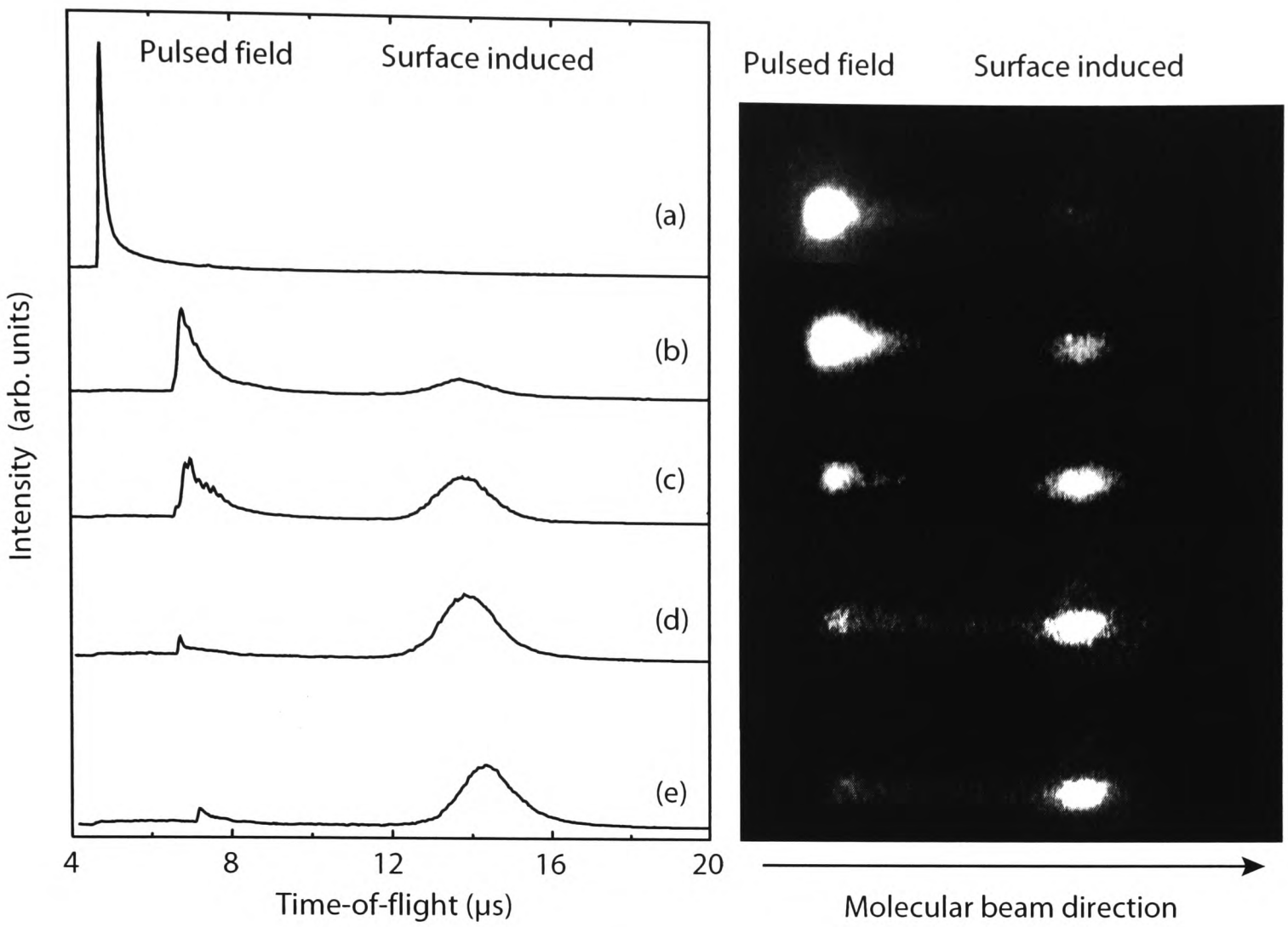

Figure 3.9: *Time-of-flight profiles and associated images showing the two distinct ion signals detectable in the experiment. The labels (a)-(e) refer to extraction fields (V cm^{-1}) of 396, 388, 379, 371 and 363 respectively. The data shown is for hydrogen Rydberg molecules initially populated in a $(20d2)_1$ state.*

3.3 Experimental spectra

3.3.1 Field-free spectra

The spectrum shown in Figure 3.10 was obtained by tuning the VUV laser wavelength to the transition to the $v' = 0, J' = 1$ B-state intermediate as described in Section 3.1. Laser 2 was scanned across the range 292.8–296 nm. Any Rydberg states populated in the excitation region were then detected through pulsed-field ionisation after a delay of 800 ns by the application of a +4000 V potential to the metal surface. The small bias voltage applied to the mesh electrode (−10 V) and the separation of the surface and the electrode (12 mm) meant that this potential generated a field of $\sim 3342\,\mathrm{Vcm}^{-1}$.

Two principal series are visible in the spectrum associated with nd states that converge to either the $N^+ = 0$ or $N^+ = 2$ thresholds of the ionic ground state. These series are labelled in Figure 3.10. The ionisation threshold for the $N^+ = 0$

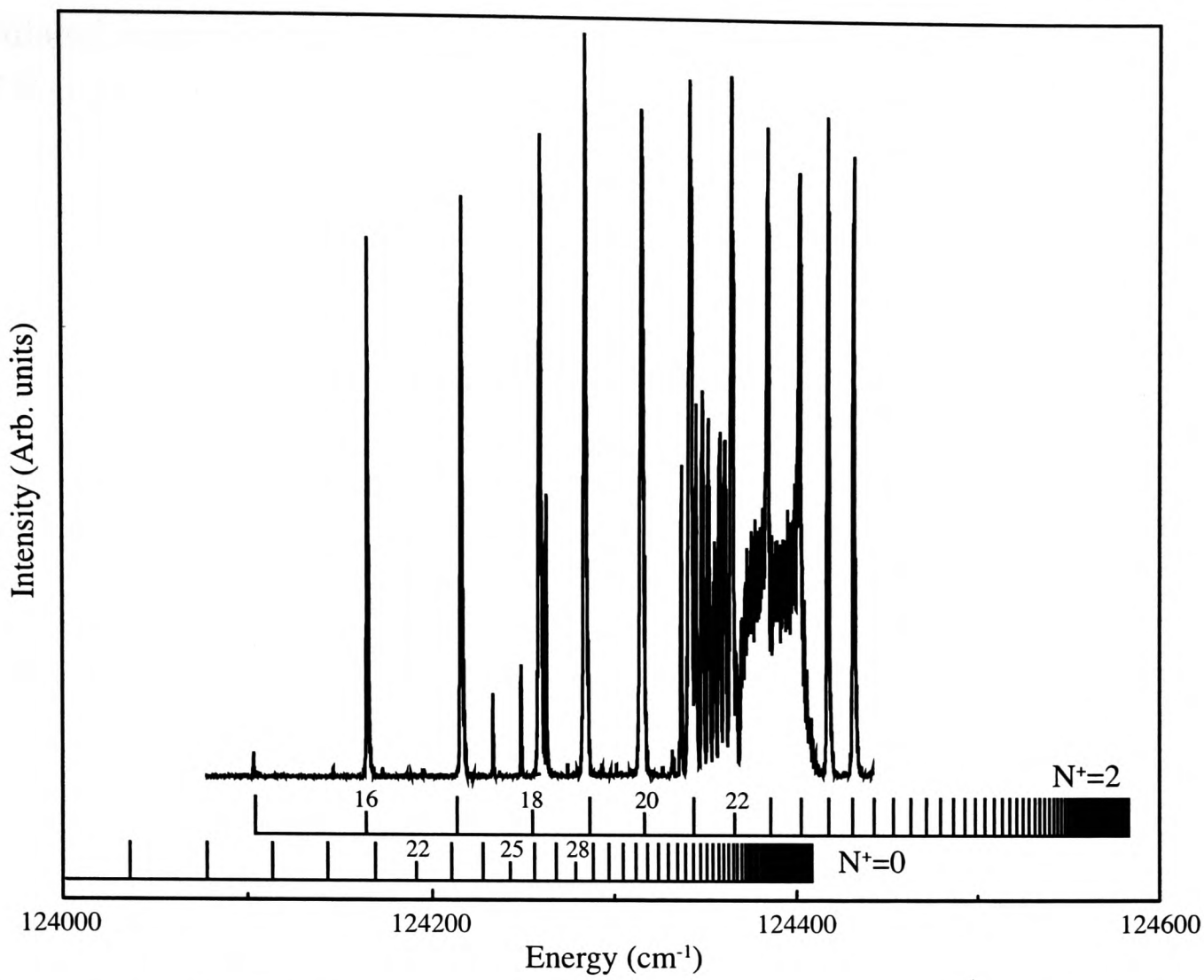

Figure 3.10: *A zero-field spectrum of H_2 Rydberg states recorded via the $v' = 0, J' = 1$ B-state intermediate. Two series are visible, one associated with states converging to the $N^+ = 0$ threshold, and the other with states converging to the $N^+ = 2$ threshold. The horizontal scale shows the total energy of the photons for laser 1 and laser 2.*

series lies at 124417.507(18) cm^{-1} above the ground state while the threshold for the $N^+ = 2$ series lies at 124592.751 cm^{-1} [81]. Previous studies [80, 83] have shown that there is a fast predissociation of the $(nd0)_2$, $(nd2)_2$ and $(ns2)_2$ series in the region ~ 124000 cm^{-1} and as a result the main peaks observed in this region are associated with the $(nd2)_1$ series and are not the $(nd0)_2$ series converging to that threshold. However the $(nd0)_2$ series can be seen to extend down to about $n = 30$.

3.3.2 Stark spectra

By applying a large negative potential (-400 V in the example shown in Figure 3.11) to the mesh electrode it was possible to carry out excitation in the presence of a homogeneous electric field. This resulted in the population of Stark energy levels of the H_2 molecules. Laser 2 was scanned from 293.8–295 nm corresponding to the excitation of the $(16 - 18d2)_1$ zero-field states. As above, the Rydberg states

populated were detected by pulsed-field ionisation after 800 ns.

The spectrum recorded in this manner is shown in Figure 3.11 and it can be seen that the zero-field states split into hydrogenic Stark manifolds arising from the admixture of the *nd* states into the $N^+ = 2$ high-l states of the same principal quantum number n which consequently gain intensity. For a more detailed discussion of the Stark affect in atomic and molecular systems see, for example, [30, 84, 85].

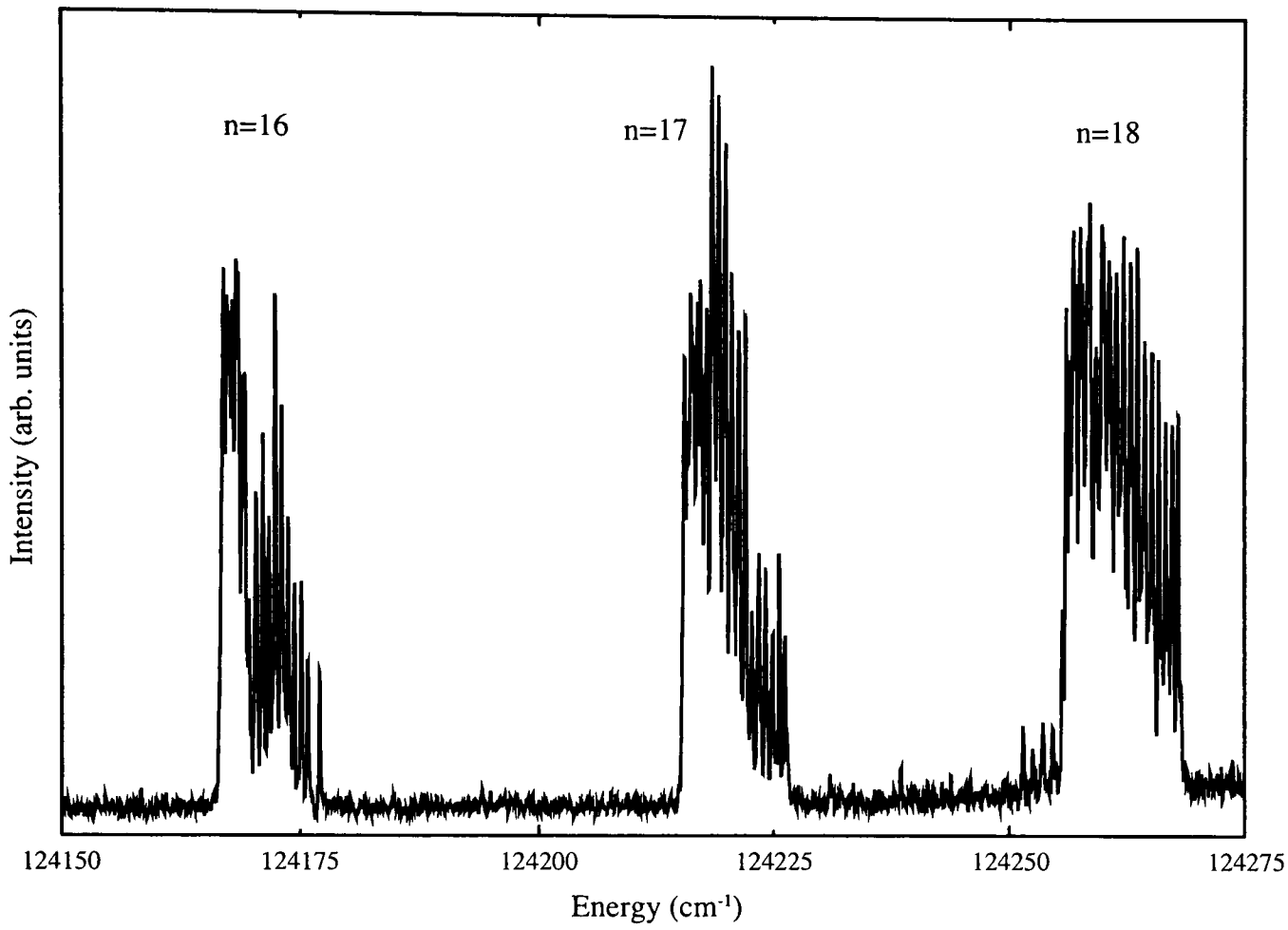

Figure 3.11: *Stark spectrum of H_2 recorded following excitation in the presence of a 340 Vcm^{-1} homogeneous electric field. The energy levels shown correspond to the excitation of the $(16 - 18d2)_1$ zero-field states. The horizontal scale is total excitation energy.*

3.4 Summary

The content of this chapter details the experimental methods used in the investigations presented in the Chapter 4. It is clear that the techniques detailed above enable the production of hydrogen Rydberg molecules in a range of initial states allowing a thorough investigation of the ionisation behaviour exhibited. The data collected is presented in full in Chapter 4 together with a discussion of the experimental observations.

CHAPTER

FOUR

Analysis of experimental data

In Chapter 3 the experimental setup was discussed and some preliminary spectra and time-of-flight profiles were presented, demonstrating the ability to selectively excite H_2 to a given quantum state and also to distinguish between the separate ion production mechanisms. The content of the following sections extends the discussion to include the detection and characterisation of surface induced ionisation.

4.1 Time-of-flight profiles

As alluded to in Section 3.2.5, by recording the time-of-flight profiles of the H_2^+ ion signal it is possible to discriminate between ions generated by direct field ionisation in the gas phase and ions formed via ionisation processes due to the presence of the surface, that is tunnelling ionisation. It is however important to be confident that the two signals identified are assigned correctly, and by analysis of the time-of-flight profiles, under a range of experimental conditions, such an assignment is possible. It is also possible to determine an estimate of the incident beam angle (see Section 4.1.2). Knowledge of this angle is crucial for the discussions which follow.

4.1.1 Assignment of the ion signals

In the previous chapter, Figure 3.9 clearly shows two distinct ion signals which have been assigned to direct field ionisation and surface induced ionisation (see also Figure 4.1). The assignment of the first signal, as that arising from direct

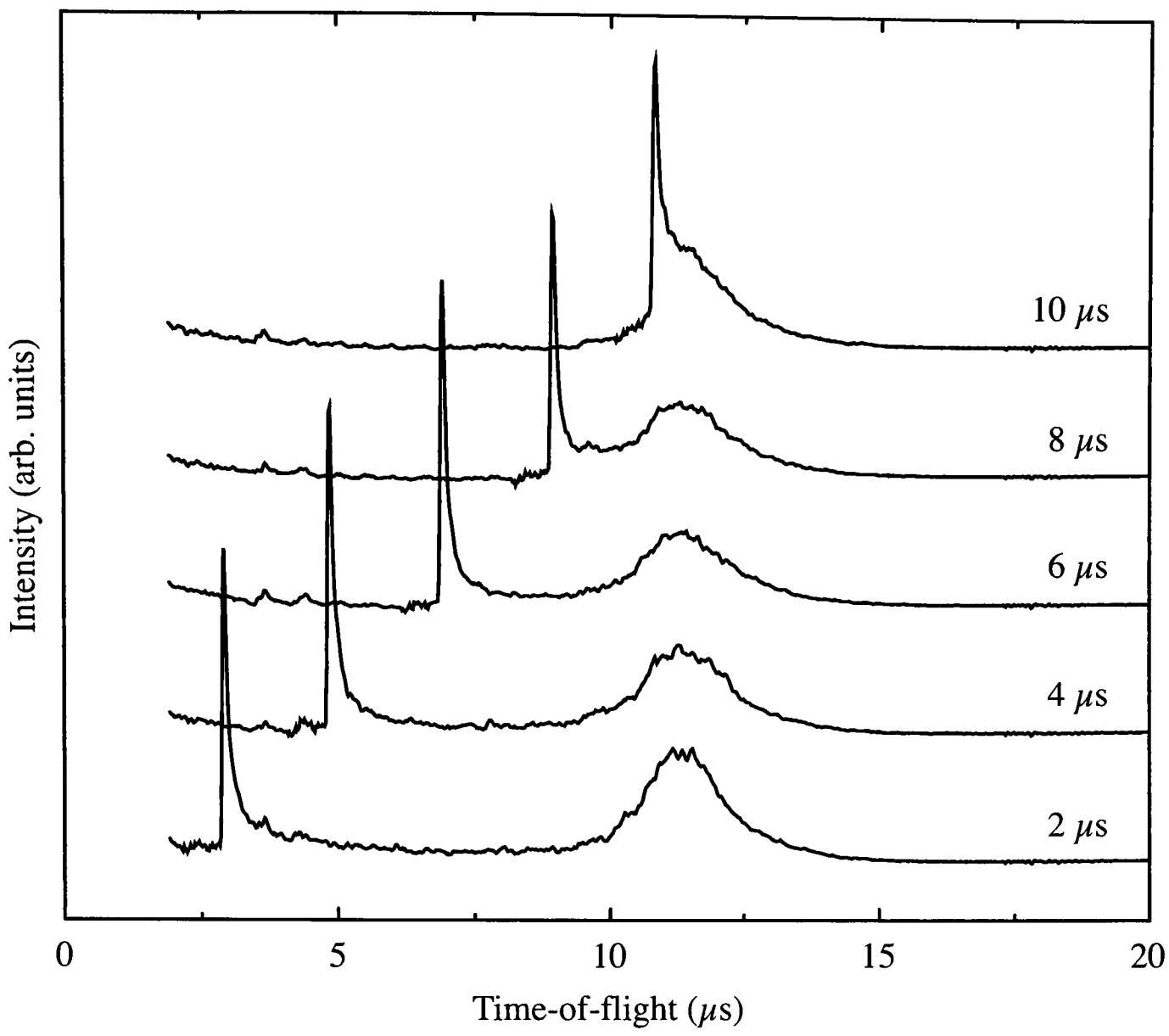

Figure 4.1: *Time-of-flight profiles illustrating the effect of altering the timing of the extraction field pulse on the arrival time of the two separate ions signals. The labels refer to the time of the pulse after the laser fires. The data corresponds to an initial population of* $(20d2)_1$ *Rydberg states and an extraction field applied was 300 V* cm^{-1}.

field ionisation, was facile. The arrival time of these ions is explicitly dependent on the timing of the field pulse, changing linearly as the timing of the pulse is altered as shown in Figure 4.1. The ions are seen to arrive $\sim 1\mu$s after the pulse is applied which is expected for the acceleration of light ions ($H_2{}^+$) in almost all but the smallest of electric fields. The second signal in Figure 4.1, also visible in Figure 3.9, exhibits an arrival time at the detector that appears independent of the pulse timing, with the constraint that the pulse must be applied at time before $\sim 10 - 12\ \mu$s. This indicates that although the electric field is necessary to detect the ions arriving at this later time, it is not required for their formation, leading to a possible conclusion that these ions are formed by a process involving the surface itself. Two further pieces of evidence confirm this proposition.

Firstly, the temporal location (in the region of 11 μs) and width of the signal are consistent with that expected for $H_2{}^+$ ions formed at the surface, given the

geometry of the experimental setup. Secondly, it is found that the exact position of the signal in the time-of-flight profile is related to the vertical position of the surface with respect to the excitation position. As mentioned in Section 3.2.1, the surface is mounted on a micro-translation stage, allowing precision control of the vertical position of the surface relative to the point of excitation. Hence, by lowering or raising the surface, the time taken for the molecular beam to reach the region in which surface induced ionisation can occur is varied. If the second signal is genuinely dependent upon the surface then it is expected that the ion arrival time at the detector should increase as the surface is lowered, and, conversely, decrease as the surface is raised. At this point it is essential to note that, when moving the surface, care must be taken to adjust the potential applied to both the grid and the surface such that the field in the region above the surface remains constant. It is worth mentioning here that the time-of-flight of the first signal, generated by direct field ionisation in the region between the grid and the surface, should be unaffected by the exact surface position. However, the time-of-flight observed for both signals will be affected to a very small degree by the change in the grid/surface separation, which will have an effect on the final velocity of any ions formed in this region, as the distance through which the ions are accelerated changes. This discussion is summarised in Figure 4.2 which shows the ion arrival times for two different vertical surface positions. As is clear, the position of the first signal remains constant whereas that of the second signal moves considerably in the time-of-flight profile.

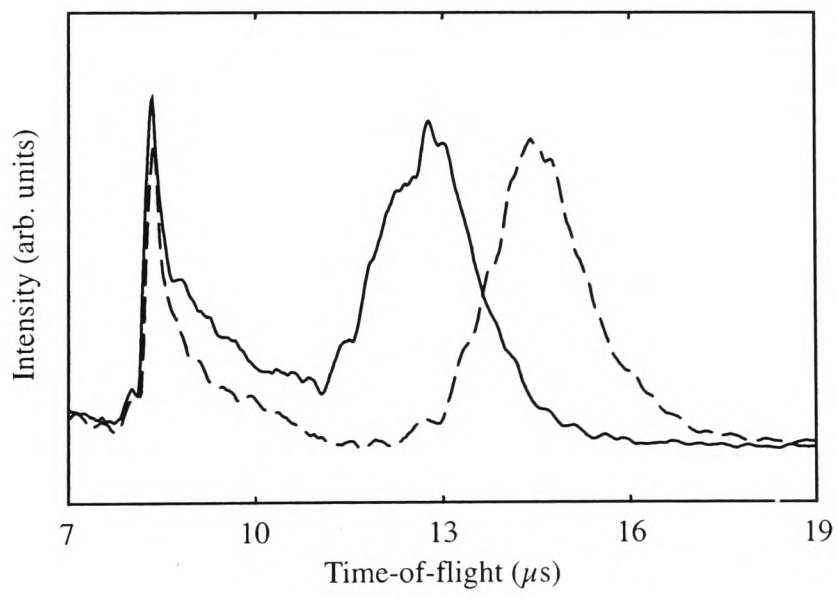

Figure 4.2: *Illustration of the dependence of the time-of-flight character of the signal on the position of the surface. The solid line represents a surface/grid separation of 12 mm, whereas the dashed line represents a separation of 12.8 mm. The data corresponds to an initial population of $(20d2)_1$ Rydberg states and an extraction field applied was 380 V cm^{-1}.*

4.1.2 Determination of the incident beam angle

The aim of the experimental investigations is to determine the separation between the surface and the Rydberg molecule required for surface induced ionisation to occur. In Section 4.2.1 an electrostatic model is presented that relates the minimum field required for the detection of the ions formed at the surface to the distance at which this ionisation occurs. However, this relationship incorporates the perpendicular kinetic energy of the ions at their time of formation. As such no study can be performed without a knowledge of both the distribution of molecular speeds and the distribution of incident beam angles. In Section 3.2.3 the mean speed of the H_2 molecules was assigned a value of 2535 ms^{-1}. The molecular speed characteristics of the pure H_2 beam are taken from previous research involving H_2 pulsed molecular beams [82]. However, in order to calculate the incident angle, further analysis of the time-of-flight profiles of the surface induced ion signal for a range of experimental conditions was necessary.

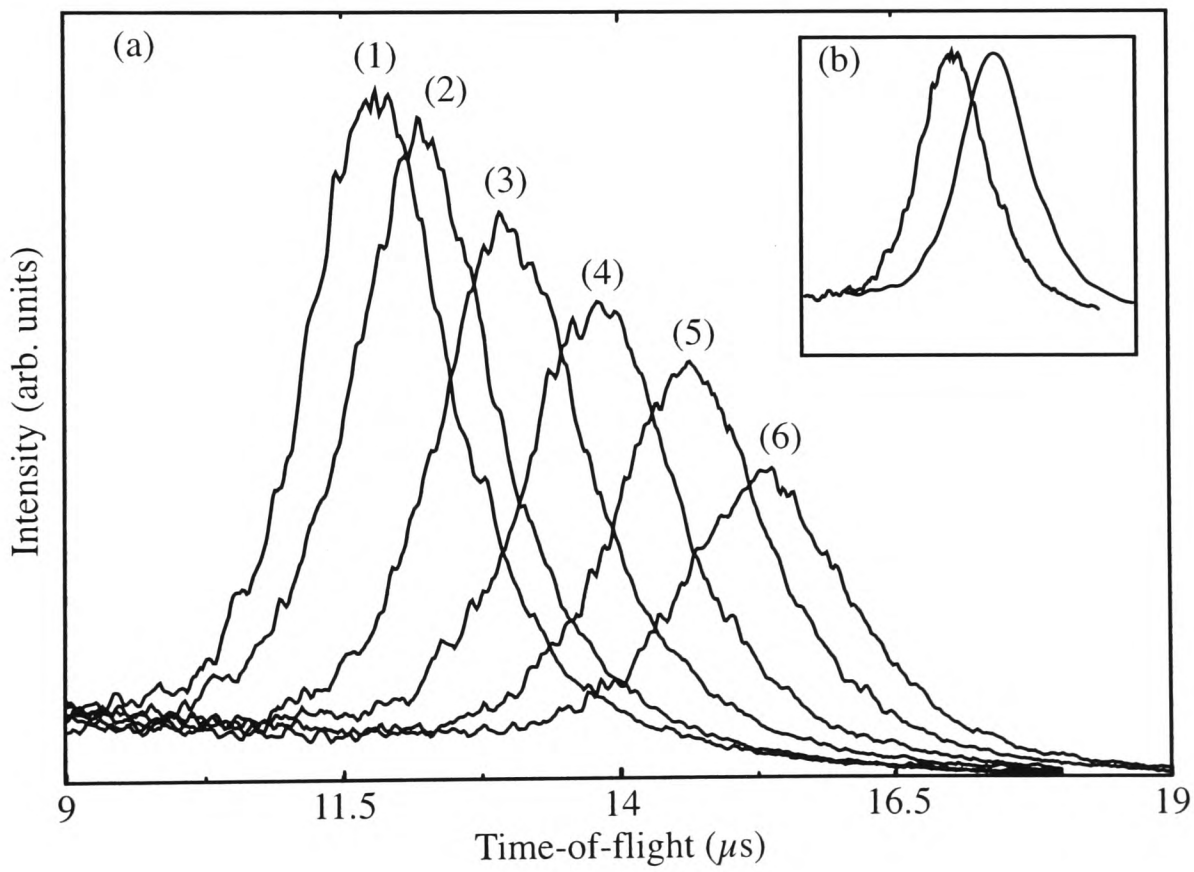

Figure 4.3: *A series of time-of-flight profiles recorded for $(22d2)_1$ states to extract information about the incident angle of the molecular beam (a). The labels refer to the surface/grid separation in mm: (1) 12.000, (2) 12.125, (3) 12.375, (4) 12.625, (5) 12.875, (6) 13.125. The inset (b) illustrates the curve fitting, based on a normal distribution, that was performed to extract the time of the maximum signal intensity for each profile.*

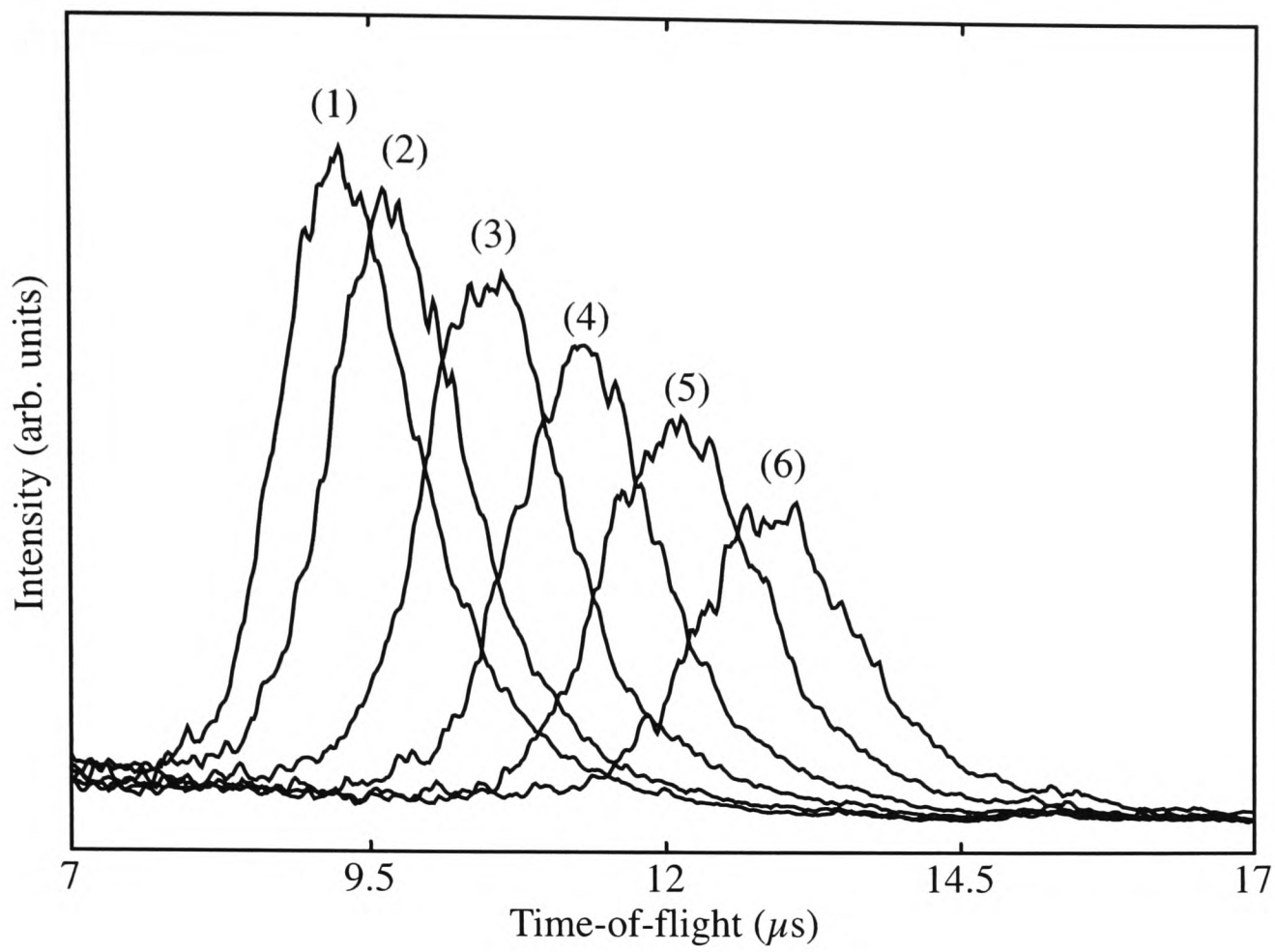

Figure 4.4: *A series of time-of-flight profiles recorded for* $(20d2)_1$ *states. The labels refer to the same surface/grid separation as in Figure 4.3.*

A series of time-of-flight profiles was recorded in which the position of the surface was varied. Data were collected for a total of ten surface positions such that each new position increased the spacing between the surface and the grid by 0.125 mm. Such a small and accurate variation of the vertical surface position was possible as the surface was mounted on a precision translation stage (see Section 3.2.3 for details). The minimum separation was 12 mm and the maximum 13.125 mm. The data is shown in Figure 4.3 for molecules initially excited to $(22d2)_1$ Rydberg states, although for clarity only six of the profiles are shown. A second set of data was recorded for the $(20d2)_1$ state and these time-of-flight profiles are shown in Figure 4.4. The potentials applied to the mesh grid and to the surface were varied so that for any given surface position the extraction field applied was 80 Vcm^{-1} in the case of states initially populated with principal quantum number $n = 22$, and 330 Vcm^{-1} in the case of $n = 20$ states. The different applied field for $n = 20$ compared with $n = 22$ was essential in order to observe the ions formed (see Section 4.2.2). By fitting a smooth curve to the time-of-flight profiles recorded, as shown in the inset in Figure 4.3, where the fitted curve is offset from the original data for clarity, a value for the arrival time of greatest signal intensity was obtained.

The arrival time of the ions, T_T, is given by

$$T_T = T_S + T_A + T_D \tag{4.1}$$

where T_S is the time taken from excitation for the molecules to reach the point above the surface at which they are ionised, T_A the time during which the resulting ions experience an accelerating force, and T_D the time required for the ions to reach the detector once they have left the region between the surface and the first grid. T_A and T_D are dependent upon the size of the extraction field applied and also the distance through which acceleration occurs but the variation arising from the change in surface/grid separation is negligible compared to the total time of flight recorded, that is $T_A + T_D \ll T_S$. As such, it is valid to assume the T_A and T_D remain constant throughout. Consequently any variation in T_T can be associated with the change of T_S due to the new position of the surface. This can be summarised by

$$\Delta T_T \approx \Delta T_S = \frac{\Delta d}{\bar{v} \sin \bar{\theta}} \tag{4.2}$$

where $\bar{v}$ is the mean beam velocity, $\bar{\theta}$ is the mean incident angle and Δd represents the relative change in surface position. Applying this approximation to the data recorded, it was found that the mean incident angle was 7.0°.

Clearly the assumption that $T_A + T_D$ remains constant is an over simplification because any variation in the surface position will affect the distance through which the acceleration occurs and consequently the final velocity of the ions as they enter the flight region from the grid to the detector. Analysing the data in more depth, employing Newton's equations of motion together with simple electrostatics, Equation 4.1 may be rewritten thus

$$\begin{aligned} T_T &= T_S + \frac{v_f - v_i}{a} + \frac{L}{v_f} \\ &= T_S + \frac{\sqrt{(v_i^2 + 2ax)} - v_i}{a} + \frac{L}{\sqrt{(v_i^2 + 2ax)}} \end{aligned} \tag{4.3}$$

where x is the separation between the surface and the grid, L represents the distance from the grid to the detector (0.197 m) and a is the acceleration due to the field. Calculating v_i using the incident angle obtained above, it is found that in fact the sum $T_A + T_D$ varies by less than 0.1 μs in the full electrostatic calculation (see Table 4.1). Consequently the initial assumption of $T_A + T_D$ being constant is valid, within the accuracy of the experiment, and it is possible to assign the mean angle of incidence of the molecular beam a value of 7.0°.

Grid/surface separation (mm)	T_A (μs)	T_D (μs)	T_A+T_D (μs)	T_T (μs)
12.000	0.23840	1.9629	2.2013	11.81
12.125	0.23964	1.9527	2.1924	12.19
12.250	0.24087	1.9427	2.1836	12.59
12.375	0.24210	1.9329	2.1750	12.93
12.500	0.24333	1.9232	2.1665	13.39
12.625	0.24454	1.9137	2.1582	13.81
12.750	0.24576	1.9043	2.1500	14.21
12.875	0.24696	1.8950	2.1419	14.65
13.000	0.24816	1.8859	2.1340	15.05
13.125	0.24935	1.8769	2.1262	15.39

Table 4.1: *A set of values for the variables T_A and T_D calculated using Equation 4.3, assuming a mean angle of 7.0° and speed of 2535 ms^{-1}. The total time-of-flight, T_T, for the $(22d2)_1$ state is also listed for comparison.*

4.2 Surface ionisation signals as a function of applied field

The variation in the total surface ionisation signal for the deposited aluminium surface, recorded as a function of the applied ion extraction field strength, is shown in Figure 4.5. The profiles show the behaviour of an initial population of $(nd2)_1$ Rydberg states with $n = 17 - 22$, as assigned in the figure. In all cases the ion extraction field is pulsed on 800 ns after excitation. The Rydberg molecules then fly, in the presence of the field, towards the target surface where ionisation occurs. If the extraction field is of sufficient magnitude then any ions formed in the vicinity of the surface will be detected. The drop in signal at the high field end of the profiles arises because the ions are directly ionised at such fields, prior to reaching the surface. As mentioned previously, this direct ionisation occurs shortly after the extraction pulse is applied and, consequently, ions formed in this manner are not detected in the same time gate as the ions under investigation and can therefore be successfully discriminated against in the process of data collection. However, to illustrate the fact that the drop in the surface induced ion signal is indeed associated with the onset of direct field ionisation, Figure 4.6 shows the field profiles of both types of ion signals for an initial population of $(nd2)_1$ Rydberg molecules where the value of the principal quantum number, n, is given in the figure.

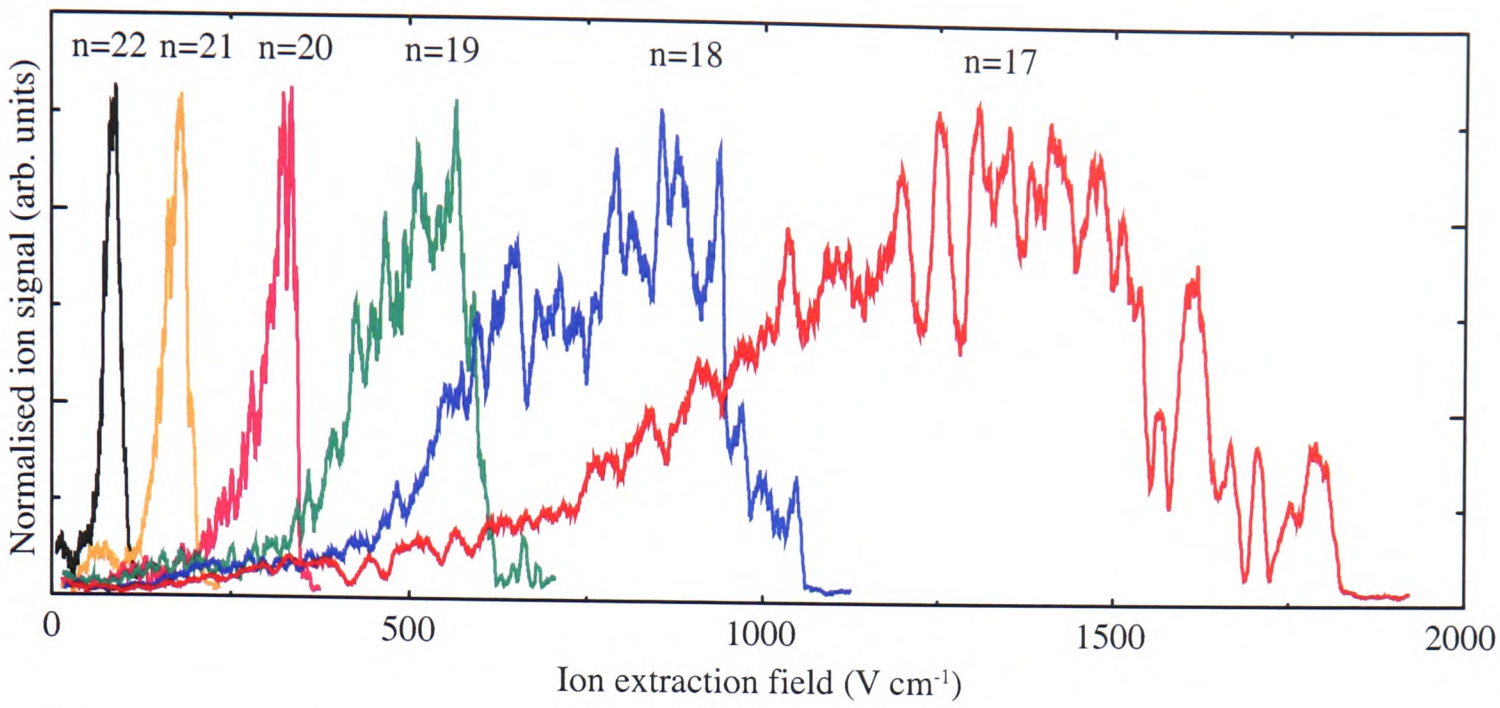

Figure 4.5: *Surface ionisation signal versus applied extraction field strength for population of the* $(nd2)_1$ *Rydberg states, incident on the deposited aluminium surface, for a range of values* $n = 17 - 22$.

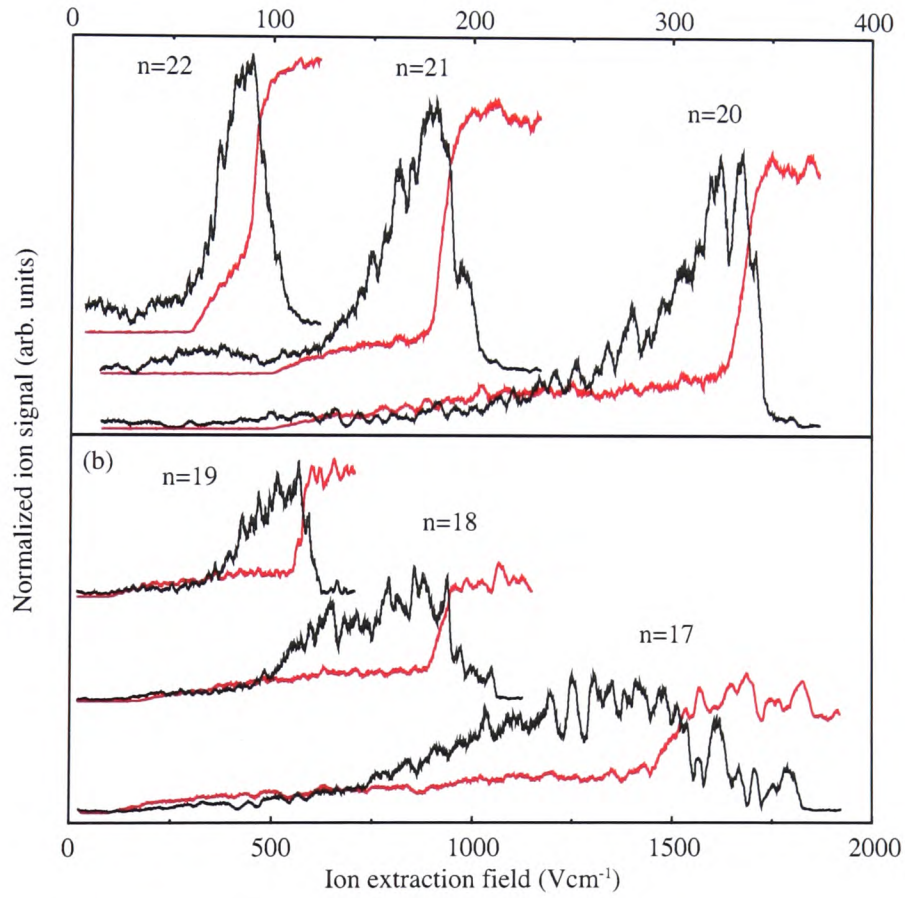

Figure 4.6: *Surface induced (black) versus direct field (red) ionisation as a function of applied field for a range of principal quantum numbers. It is evident from this that the sudden loss of surface induced signal can be attributed to the increased probability of direct field ionisation.*

Ignoring the apparent structure in the profiles (see Section 4.2.8 for more details) for the time being, the following sections detail the nature of the observations and a plausible explanation of behaviour is presented.

4.2.1 Electrostatic model

If surface induced ionisation were to occur at a molecule/surface separation Z_i then the minimum external field (in atomic units) that must be applied to prevent the ions striking the surface, and hence the minimum field required for ion detection, is given by [13]

$$E_{min}\left(Z_i, T_\perp\right) = \left[\frac{1}{2Z_i} + \sqrt{\frac{T_\perp}{Z_i}}\right]^2 \qquad 4.4$$

where $T_\perp = \frac{1}{2}mv_\perp^2$ is the kinetic energy, perpendicular to the surface, of the molecule at the point of ionisation, Z_i. This equation is based on an image charge model which assumes that the total energy of an ion in front of a surface and in the presence of an applied electric field, E, is given, in atomic units, by

$$U = -\frac{1}{4Z} - EZ + T_\perp. \qquad 4.5$$

Additionally, Equation 4.4 may be rearranged to give a value of the minimum separation at which ions formed will have their velocity reversed and be detected for a given field and kinetic energy

$$Z_{min}\left(E, T_\perp\right) = \frac{T_\perp + \sqrt{E}}{2E} + \frac{1}{2}\sqrt{\frac{T_\perp^2 + 2T_\perp\sqrt{E}}{E^2}}. \qquad 4.6$$

Consequently Equations 4.4 and 4.6 provide a link between the ion signal profiles recorded and the molecule/surface separation at which ionisation occurs.

4.2.2 Effect of the principal quantum number

Ionisation of the Rydberg molecule requires the removal of the Rydberg electron. This electron occupies an orbital of large radius and is, therefore, weakly bound. Referring to Section 1.2.2 the radius scales as n^2 and so it is not surprising to find that, in the data presented in Figure 4.5, the onset of the surface ionisation signal occurs at higher fields when states of lower principal quantum number are populated. This increase in the field reflects ionisation occurring at a smaller molecule/surface separation and is in agreement with the decreased extent of the electron orbital radius. Indeed, the hydrogenic theory presented in Chapter 2 and experiments involving xenon Rydberg states [13] have shown that the value of Z_i scales as n^2.

Through the link between ionisation distance and the applied electric field (see Equation 4.4), the profiles in Figure 4.5 can be considered to show how the tunnelling ionisation probability varies with distance from the surface, after taking into account the spread of incident kinetic energies in the molecular beam. At this time such a spread is not considered (see Section 4.2.3) and a value of $T_\perp = 3.6352 \times 10^{-5}$ a.u. is used which corresponds to the mean kinetic energy of the molecules, that is using the values, $\bar{v} = 2535\ \mathrm{ms}^{-1}$ and $\bar{\theta} = 7.0°$.

Using Equation 4.6, the x-axis of Figure 4.5 can be rescaled to represent the distance above the surface at which the detected ions were formed. If the x-axis is further scaled by a factor of $1/n^2$, where n is the principal quantum number of the initially populated Rydberg state, then, assuming the ionisation behaviour follows that of the atomic Rydberg states, it would be expected that all the profiles would lie at the same point on the x-axis and indeed be represented by a single curve, that is the data scales according to n^2. This rescaling is shown in Figure 4.7(a) and it is clear that such a relationship does not exist in the data presented here for an initial population of $(nd2)_1$ hydrogen Rydberg states.

In fact the field profiles are associated with much lower fields than would be predicted from Equation 4.4, assuming that surface ionisation occurs at $Z_i = 4.0n^2a_0$ as predicted from the calculations in Chapter 2, and using the quantum numbers assigned to the initially excited $N^+ = 2$ levels. If, however, an effective principal quantum number, ν_0, calculated with respect to the $N^+ = 0$ threshold (see Equation 4.7), is assigned to each state, the ionisation distances are found to scale as ν_0^2, as illustrated in Figure 4.7(b). The effective principal quantum number, ν_0, may be calculated as follows (ignoring the quantum defect with respect to the $N^+ = 2$ limit)

$$\nu_0 = \left[\frac{1}{n^2} - \frac{(IP_2 - IP_0)}{\Re_H}\right]^{-\frac{1}{2}} \qquad 4.7$$

where IP_i is the ionisation potential of the Rydberg series with rotational angular momentum quantum number i, and $\Re_H$ is the Rydberg constant for hydrogen. The effective quantum number generated is invariably non-integer.

This suggests that the overall ionisation mechanism involves complete transfer of energy from the H_2^+ ion-core rotation to the Rydberg electron. Indeed a similar phenomenon of field-induced autoionisation (see Section 1.3.3) has previously been observed for the ionisation of these same states in the gas phase [29, 30]. Also, Figure 4.7 (b) shows that ionisation occurs over an apparent separation range of $Z_i \sim 3 - 5\nu_0^2 a_0$ which is in good agreement with the range found

in previous experiments for xenon atoms [13] (except that ν_0 is used rather than n). A comparison with the simulations performed in Section 2.4.3 is presented later in Section 4.2.5.

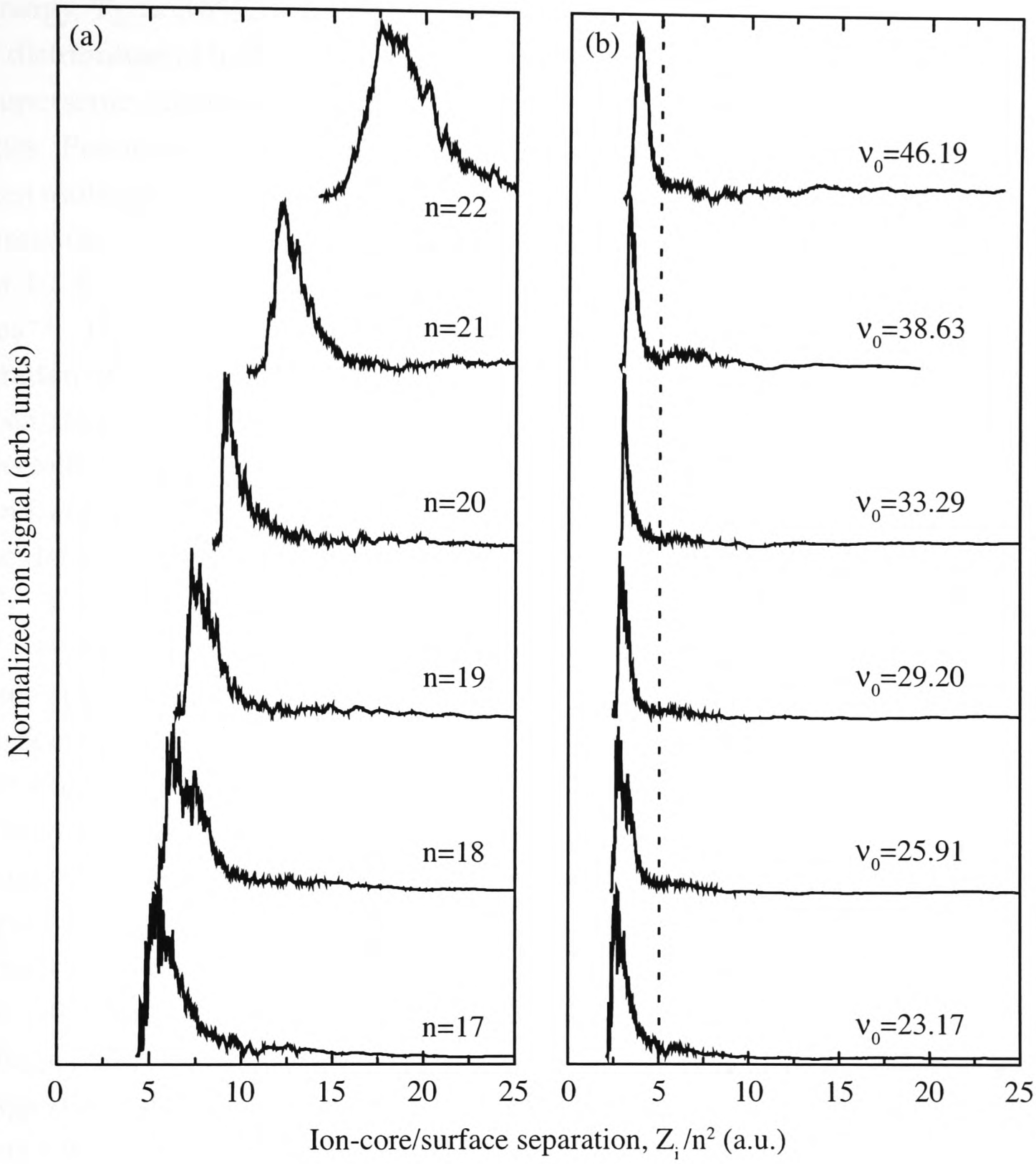

Figure 4.7: *(a) Surface ionisation profiles for $n = 17 - 22$ Rydberg states at an aluminium surface plotted as a function of Z_i/n^2 using Equation 4.6 and assuming a perpendicular velocity of $v_\perp = 309\ ms^{-1}$. (b) Same data as in (a) except that ν_0 (see Equation 4.7) is used in calculating the horizontal axis rather than n.*

4.2.3 The distribution of molecule kinetic energy in the beam

The analysis presented above and in the following sections, is based on the assumption that all molecules approaching the surface possess the same kinetic energy, $T_\perp = 3.6352 \times 10^{-5}$ a.u. (see Section 4.2.2). There is in reality, however, a distribution of both molecular speeds and incident angles within the skimmed, supersonic expansion, resulting in a distribution of perpendicular kinetic energies. Previous analysis of the molecular speed distribution of a beam of hydrogen molecules [82], in essentially the same apparatus with a comparable backing pressure, indicated that the distribution can be characterised by a temperature of 1.3 K. As such the standard deviation of the molecular speeds is $\sigma = 73.5$ ms^{-1}. The distribution of incident angles is less well characterised but consideration of both the experimental geometry (see Section 3.2.1) and the size of the excitation volume (a beam waist in the order of a few hundred microns is expected) suggests that a range $6.6° \leq \theta \leq 7.4°$ is realistic. Taking both the speed and angular distributions into account, three values of the kinetic energy can be defined. The first represents the slowest and shallowest molecule approach, $T_\perp = 3.014104 \times 10^{-5}$ a.u., the second the mean values of both parameters, $T_\perp = 3.63534 \times 10^{-5}$ a.u., and the third represents the fastest and steepest molecule approach, $T_\perp = 4.33615 \times 10^{-5}$ a.u.. Repeating the transformations detailed in Section 4.2.2, substituting each value of $T_\perp$, three scaled profiles are calculated for each quantum number. The profiles for $n = 22$ are shown in Figure 4.8. Similar variations are seen for other quantum numbers. Analysis of these profiles suggests that including the full range of kinetic energies in the scaling process would affect the position of the rise in the profile by, at most, $\pm 5\%$. Thus the major conclusion of the previous section is not compromised by the fact that the kinetic energy distribution has not been explicitly taken into account. The exact shape of the profiles, will however, be dependent upon the form of the kinetic energy distribution used in the transformation. Therefore, it would be beneficial in any future experiments to further collimate the molecular beam to the extent that the angular distribution of the approaching molecules may be more narrowly defined. Such a modification would be possible by introducing a second skimmer into the molecular beam path.

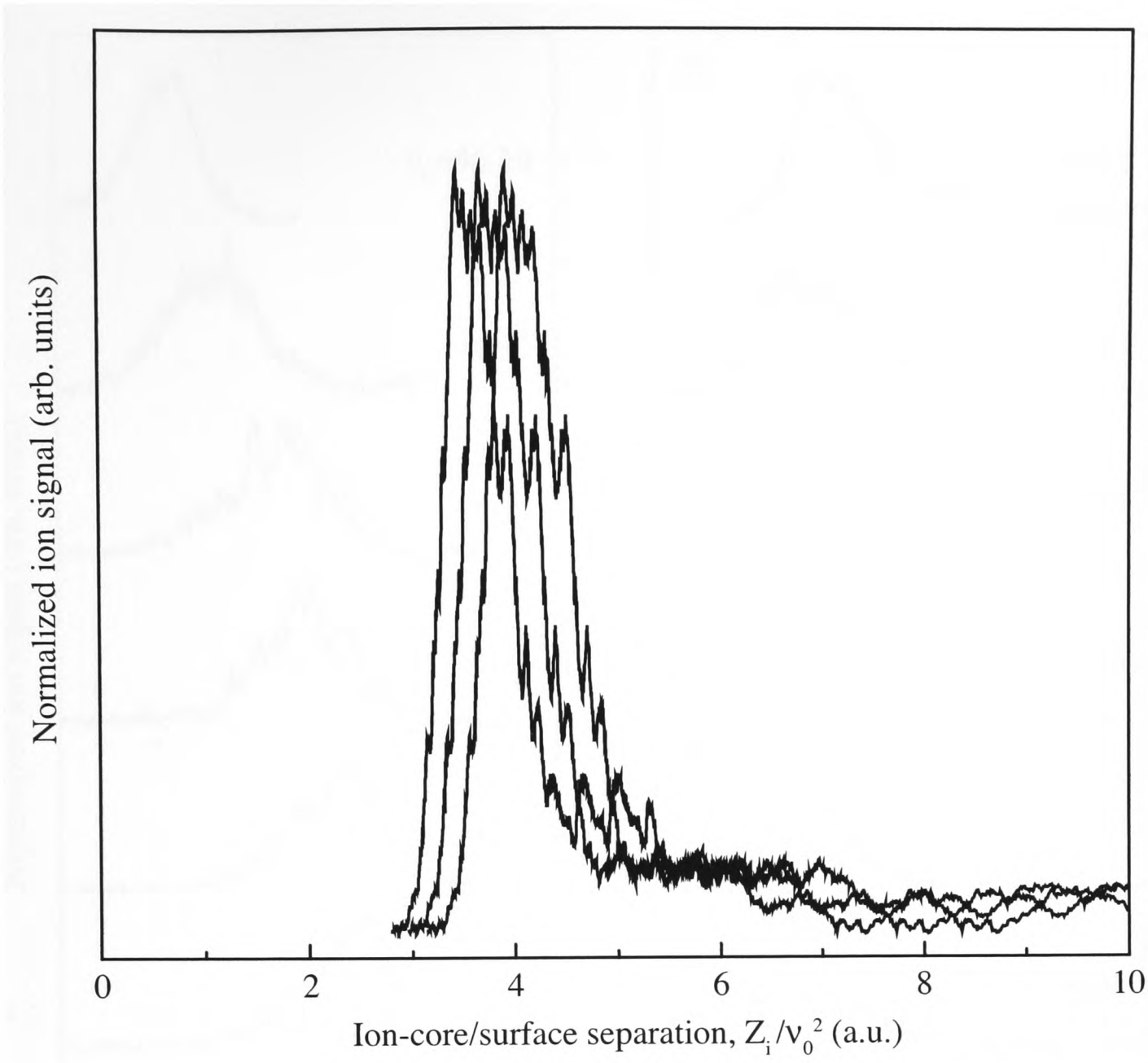

Figure 4.8: *Surface ionisation profiles for $n = 22$ Rydberg states at an aluminium surface plotted as a function of Z_i/ν_0^2 using Equation 4.6. Each profile is generated using a different value of $K_\perp$ as detailed in the text.*

4.2.4 Surface ionisation behaviour of the $N^+ = 0$ states

The behaviour displayed by the $N^+ = 2$ Rydberg states has been associated with the coupling between the $N^+ = 2$ and $N^+ = 0$ channels via a mechanism akin to forced rotational auto-ionisation. Were this the case, then one would expect the surface ionisation *vs* field profiles of the $N^+ = 0$ states to scale in a way similar to the atomic states, that is as n^2, as there is no rotational energy that can contribute to the ionisation process. Such a study is feasible by initially populating a series of $(nd0)_2$ Rydberg states. The $(41 - 45d0)_2$ states lie energetically between the $n = 22$ and $n = 21$, $(nd2)_1$ Rydberg states, and exhibit sufficient intensity to be detectable in the experimental setup used here. These states are clearly visible in Figure 3.11. The associated field *vs* signal profiles of these states, recorded in an identical manner to the data collected for the $N^+ = 2$ states, are shown below

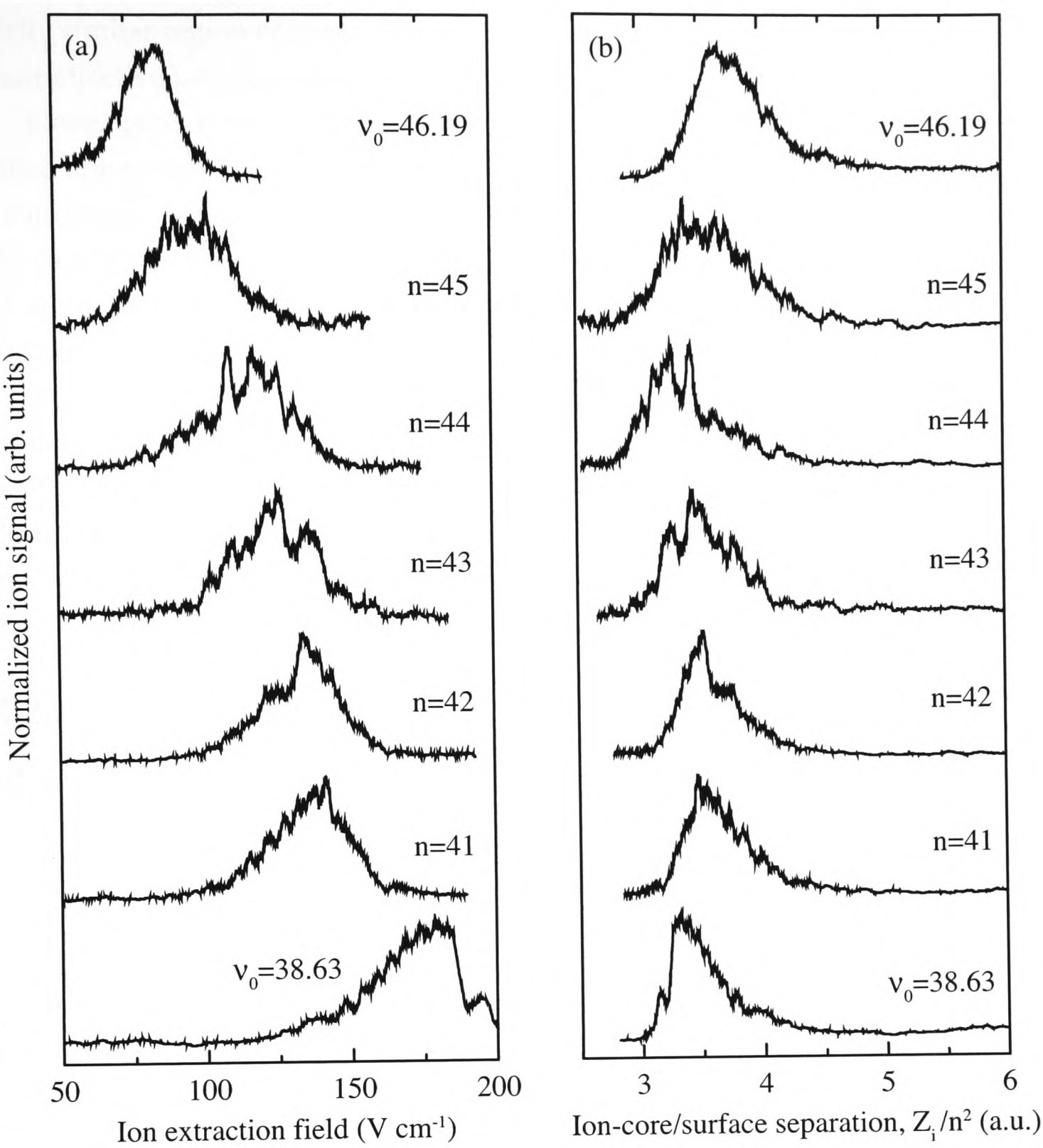

Figure 4.9: *(a) Surface ionisation signal versus applied extraction field strength for population of the* $(nd0)_2$ *Rydberg states for a range of values* $n = 41 - 45$ *together with data for the* $(nd2)_1$, $n = 21$ $(\nu_0 = 38.63)$ *and* 22 $(\nu_0 = 46.19)$ *states. (b) The same data as in (a) plotted as a function of* Z_i/n^2 *(or* Z_i/ν_0^2 *in the case of the* $(nd2)_1$ *states).*

in Figure 4.9(a). Once again, the profiles form a series where the extraction field required for ion detection decreases as the principal quantum number of the state initially populated increases. The variation is less marked however, and this can be understood by the fact that the radius scales as n^2. Hence as n increases so the degree of radial increase going from $n \rightarrow n+1$ is smaller. For comparison, the data for the $n = 22$ and $n = 21$, $N^+ = 2$ Rydberg states, which lie in an energet-

ically similar region of the spectrum, are included. These states are labelled with their effective principal quantum numbers, ν_0.

Once again, if the x-axis is rescaled such that it represents the ionisation distance rather than the field, a scaling factor for the ionisation distance, Z_i, can be determined. Such a transformation leads to data presented in Figure 4.9(b). In the case of the $N^+ = 0$ states the final ionisation distances have been divided by n^2 while those of the $N^+ = 2$ states have been divided by ν_0^2, as outlined in the previous section.

Immediately two things are apparent. Firstly, the $N^+ = 0$ data does indeed scale as n^2, as observed for atomic Rydberg states. Secondly, the $N^+ = 2$ states readily fit this scaling if the effective principal quantum number, ν_0, is employed. Both these observations lend considerable weight to the conclusion that surface ionisation of Rydberg states initially prepared in $(nd2)_1$ levels is indeed mediated through a process of forced autoionisation due to coupling with $N^+ = 0$ channel.

4.2.5 Comparison with calculated ion production profiles

At this stage it is prudent to consider whether or not the simulations carried out in Chapter 2 provide an accurate prediction of the experimentally observed ionisation behaviour. Given that the calculations are based on an atomic model it is clear that the ionisation profiles of the $N^+ = 2$ states, which exhibit a behaviour dependent upon the rotational energy of the molecule core, cannot be directly simulated. However, if this discussion is focused on the scaled profiles of ion signal *vs* ion-core/surface separation, as shown in Figure 4.7 for the $N^+ = 2$ states and Figure 4.9 for the $N^+ = 0$ states, then a comparison may be made.

Three separate approaches are presented in Figure 4.10. In (a) the calculated total ion production from Figure 2.13, assuming a population that is evenly spread across all possible states belonging to a given principal quantum number, is compared with the experimentally determined, ion signal. It is, in fact, the profile associated with the $N^+ = 0$, $n = 41$ state but the exact choice of state makes little discernible difference. It is clear that both the onset and slope of the predicted profile are under-estimates. In fact such an under-estimate in the position of the onsets is not unexpected as a similar discrepency was also observed in the xenon/surface experiments [13]. In the example shown in (a), the difference between simulated and experimental onset, determined by fitting a straight line through the data, is $\sim$0.4 a_0. The calculated curves in both (b) and (c) have been shifted to remove this systematic error.

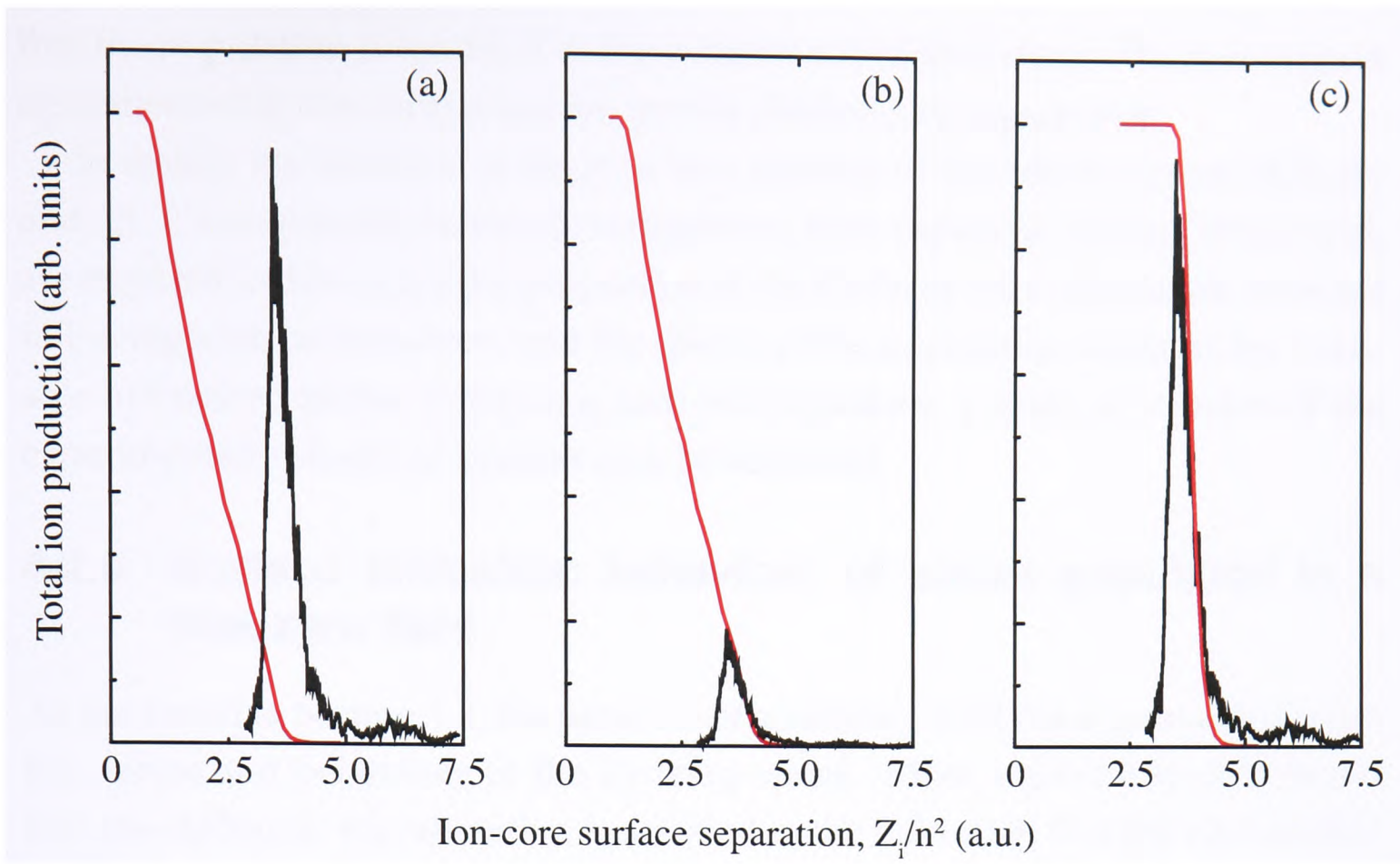

Figure 4.10: *Comparison of calculated ion production curves (red) with the experimentally determined profiles (black). An explanation of the three situations is provided in the text.*

The discrepancy between the slope of the calculated curve and that of the experimental data in (a) may arise for two reasons. Firstly, it is possible that the total population is not being ionised at the surface and detected by the application of fields below the threshold for direct ionisation. That is the direct field ionisation starts to cut in well before the surface signal has finished rising (this statement is justified by Figure 4.6). Consequently, a comparison of ion production based upon a full conversion of population is not valid. That is, the profile observed in the experiment is actually only sampling a small proportion of the total Rydberg state population. Such a situation is shown in Figure 4.10(b) where good agreement between the calculations and the experiment is achieved. In this case the surface ionisation profile is assumed to account for only 20% of the total Rydberg state population. If this were to be the case, then further information, obtainable through analysis of the direct ionisation signal, would be needed to clarify the exact proportion of the population that is ionised at the surface and subsequently detected. Secondly, the calculated curve shown in (a) and (b) assumes that the population is evenly spread amongst all $n - |m|$ hybridised states of a given Stark manifold n. This is not necessarily the case and indeed previous theoretical calculations [86] have suggested that the spread of population is not even. To this end, the simulated curve in (c) has been generated by assuming

that the population is localised in the extreme red-shifted state. This shows good agreement with the normalised ion profile obtained by experiment.

In reality, the situation is likely to be a mixture of the effects described in (b) and (c). Consequently, further investigations, both experimental and theoretical, are required to determine the proportion of the Rydberg state population detected following surface ionisation, and the spread of the population amongst the available hybridised states. Following such investigations, a better simulation of the experimentally observed profiles may be achieved.

4.2.6 Surface ionisation behaviour of states populated in a non-zero field

As discussed in Section 1.4, the presence of an electric field has a great effect upon the nature and behaviour of the Rydberg states. Most importantly, it is found that the electronic wavefunction is oriented in the field such that the blue-shifted states exhibit a wavefunction localized along the $+z$-axis while the red-shifted states have a wavefunction oriented along the $-z$-axis, where the z-axis is defined as the field axis (see Figure 1.8). Consequently, as the Rydberg molecules approach the surface it is expected that the blue-shifted states, whose electron distribution is aligned away from the surface, will ionise at significantly shorter molecule/surface separations compared to the red-shifted states (see Section 2.4), and hence require significantly higher fields to be applied for detection. This was investigated experimentally by selectively exciting an initial population of the $n = 18$ Stark manifold (whose intensity is derived from $(18d2)_1$ Rydberg states) in the presence of a 333 Vcm^{-1} electric field, generated by the application of a constant potential to the mesh-grid.

In order to identify suitable states for investigation, the doubled output of laser 2 was scanned between 294.10–294.33 nm and a +4000 V potential was applied to the surface 800 ns after excitation. The application of this potential had the effect of field ionising all the Rydberg states initially populated. The Stark spectrum obtained in this way is presented in Figure 4.11. A spectrum recorded over a greater range of excitation energies is shown in Figure 3.11. Three different members of the manifold were chosen to characterise the range of ionisation behaviour exhibited by the Stark states, belonging to the $n = 18$ manifold, incident on the surface. The chosen states, one blue-shifted state (a), one state in the centre of the manifold (b) and one red-shifted state (c), are highlighted in Figure 4.11. For each state a field *vs* ion signal profile was recorded in an analogous way to

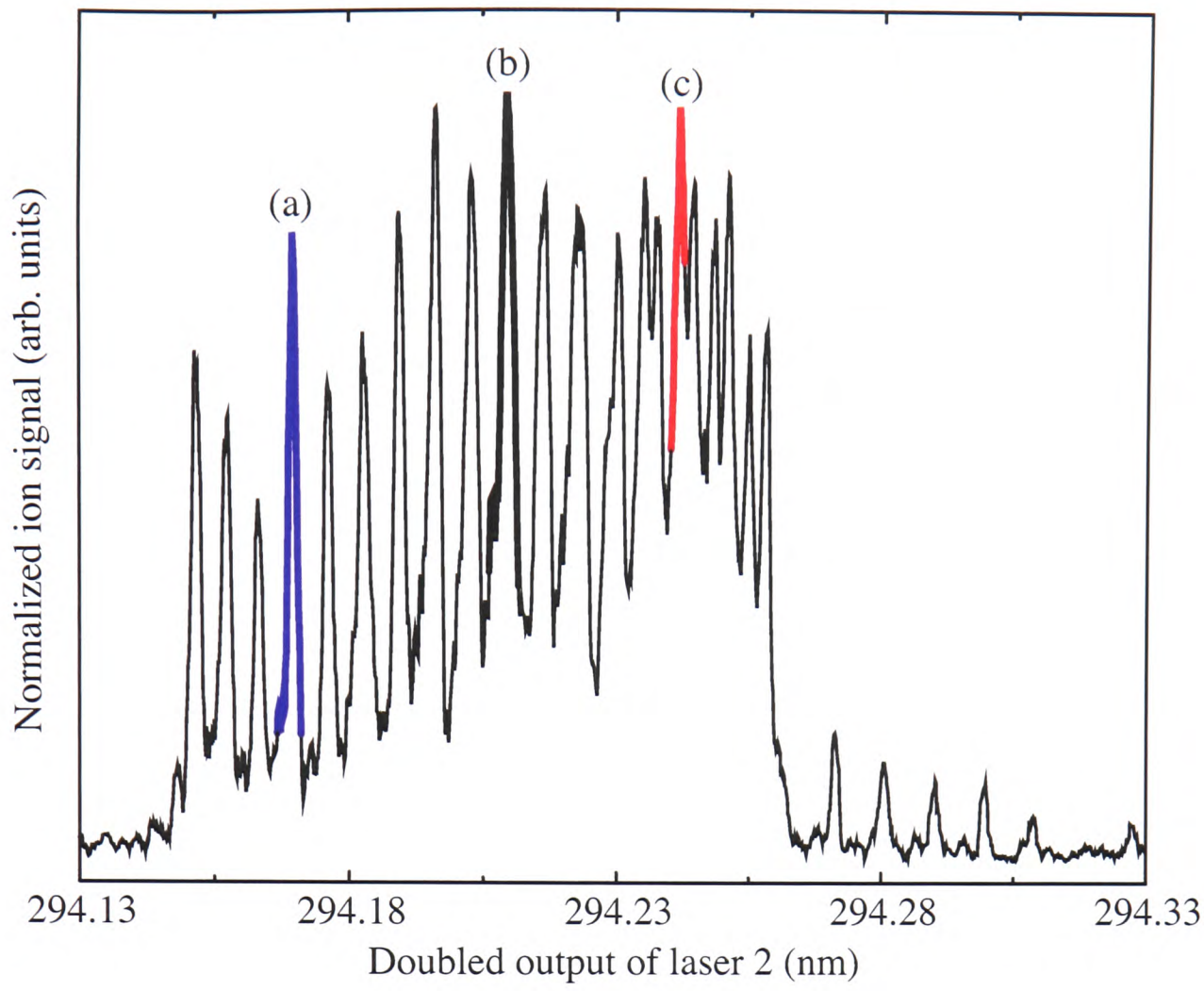

Figure 4.11: *Stark spectrum of H_2 recorded in the presence of a 333 Vcm^{-1} electric field. The spectrum arises from excitation to an initial population of $(18d2)_1$ Rydberg states. The three labelled lines are referred to in the text.*

the previous investigations of zero-field states detailed above, and the results are presented in Figure 4.12. Once again, the sudden drop in signal intensity at high field arises due to the molecules being directly ionised in the field following the application of the extraction pulse. The fact that the field at which this drop in signal intensity occurs is different in each case is evidence that different states have indeed been populated. It is also interesting to note that initial excitation to blue-shifted states results in the molecules being more readily ionised in the field than initial excitation to red-shifted states. This is in agreement with previous theoretical work [86] although this is not as predicted for purely diabatic (hydrogenic) ionisation (see section Section 1.4.2). The colours of the profiles in Figure 4.12 are related to the colours used for the individual members of the Stark manifold shown in Figure 4.11.

As is evident from position of the low field onset and the rise of the signals in Figure 4.12, no significant difference in surfaced induced ionisation behaviour arises when initially exciting blue-shifted states as opposed to red-shifted states. This is in agreement with the previous experimental work with xenon atoms [13].

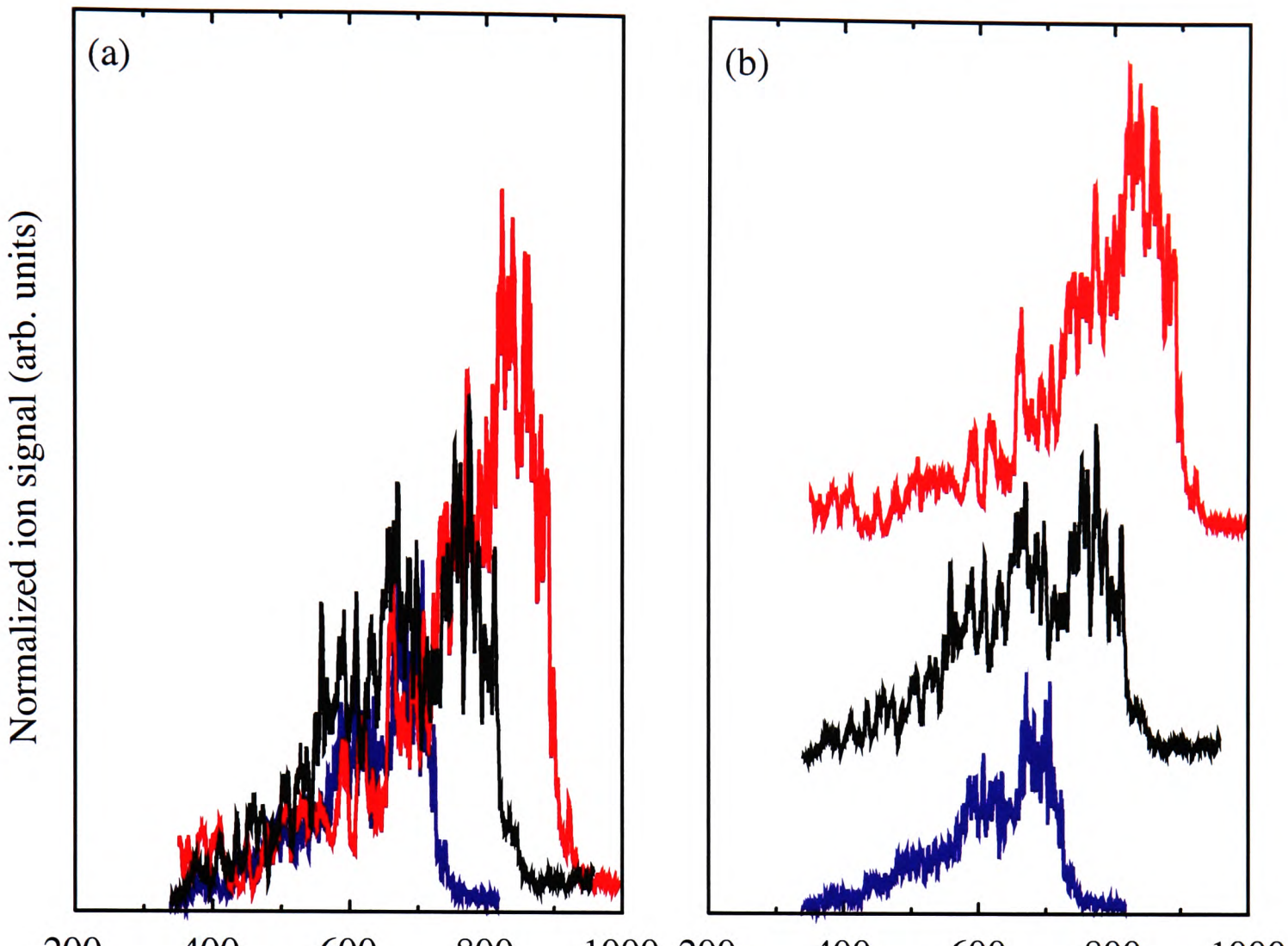

Figure 4.12: *(a) Surface ionisation profiles recorded as a function of applied extraction field strength for the three, $n = 18$, Rydberg states highlighted in Figure 4.11. (b) Same data as in (a) but offset for clarity.*

If one uses the same approach as given in [15] then the similar behaviour of all the members of the manifold can be explained by considering the evolution of the state as the surface is approached . Prior to reaching a sufficiently small molecule/surface separation for ionisation to take place, it is feasible that level crossings with levels in adjacent n manifolds will occur. In the hydrogen molecule such interactions between states of the same M_J quantum number are manifested as avoided crossings and the energy separations at these avoided crossings are strongly M_J dependent and are largest for the lowest M_J states (see Section 1.4.3). If these crossings are traversed *adiabatically* then the character of a molecule initially in a state $|nkM_J\rangle$ will assume the character of the state $|n'k'M_J\rangle$. As the surface is approached the molecule typically undergoes many such avoided crossings and the overall effect of this is that the electron probability densities associated with the blue and red-shifted states initially populated will, on average, be

similar. Consequently the surface ionisation behaviour of the initially populated blue-shifted and red-shifted Stark states is expected to be the same. The fact that this is indeed the behaviour exhibited by these Stark states suggests that such crossings are traversed *adiabatically*. However, an additional complication arises in the molecular case presented here. The question arises as to whether the crossings between the $N^+ = 0$ and $N^+ = 2$ manifolds influence the populations of the states. However, these processes are likely to be almost diabatic in character unless the system remains at a crossing point for a significant period of time (see Section 4.2.8).

4.2.7 The nature of the target surface

While all the results presented so far have involved H_2 molecules incident on a deposited aluminium surface, questions arise as to whether the ionisation behaviour of the Rydberg states may also be dependent upon the properties of the surface itself. Referring back to Section 2.2.2, it is noted that the total potential experienced by the incident particle is dependent on a surface potential term, which itself is dependent upon the electronic properties of the surface. In order to investigate this, a gold target surface was prepared in an identical manner to the aluminium surface, as detailed in Section 3.2.4. Data was collected for an initial population of $(nd2)_1$ Rydberg states, for the range of principal quantum numbers $n = 19 - 22$, using the same experimental methodology as previously used for the deposited aluminium surface. The results are presented in Figure 4.13.

Once again, efficient surface ionisation was observed in the range of principal quantum numbers investigated and structure is present in the field profile. In fact it was found that the surface material had very little effect on the ionisation characteristics of the $(nd2)_1$ Rydberg states. The results for both aluminium and gold target surfaces are compared in Figure 4.14 for H_2 $(nd2)_1$ states initially populated with principal quantum number $n = 20$ and 19. It is evident that the two profiles associated with a given quantum number are very similar and share the same ionisation properties, including the presence of the structure. Thus the resonant behaviour appears to be independent of the type of metal, although it is worth noting that there may be subtle differences which are not distinguishable within the signal-to-noise ratio. A similar comparison for the states $n = 21$ and 22 leads to an identical conclusion.

The form of the field profile is, however, dependent upon the surface roughness. Replacing the smooth surfaces, prepared via metal vapour deposition, with

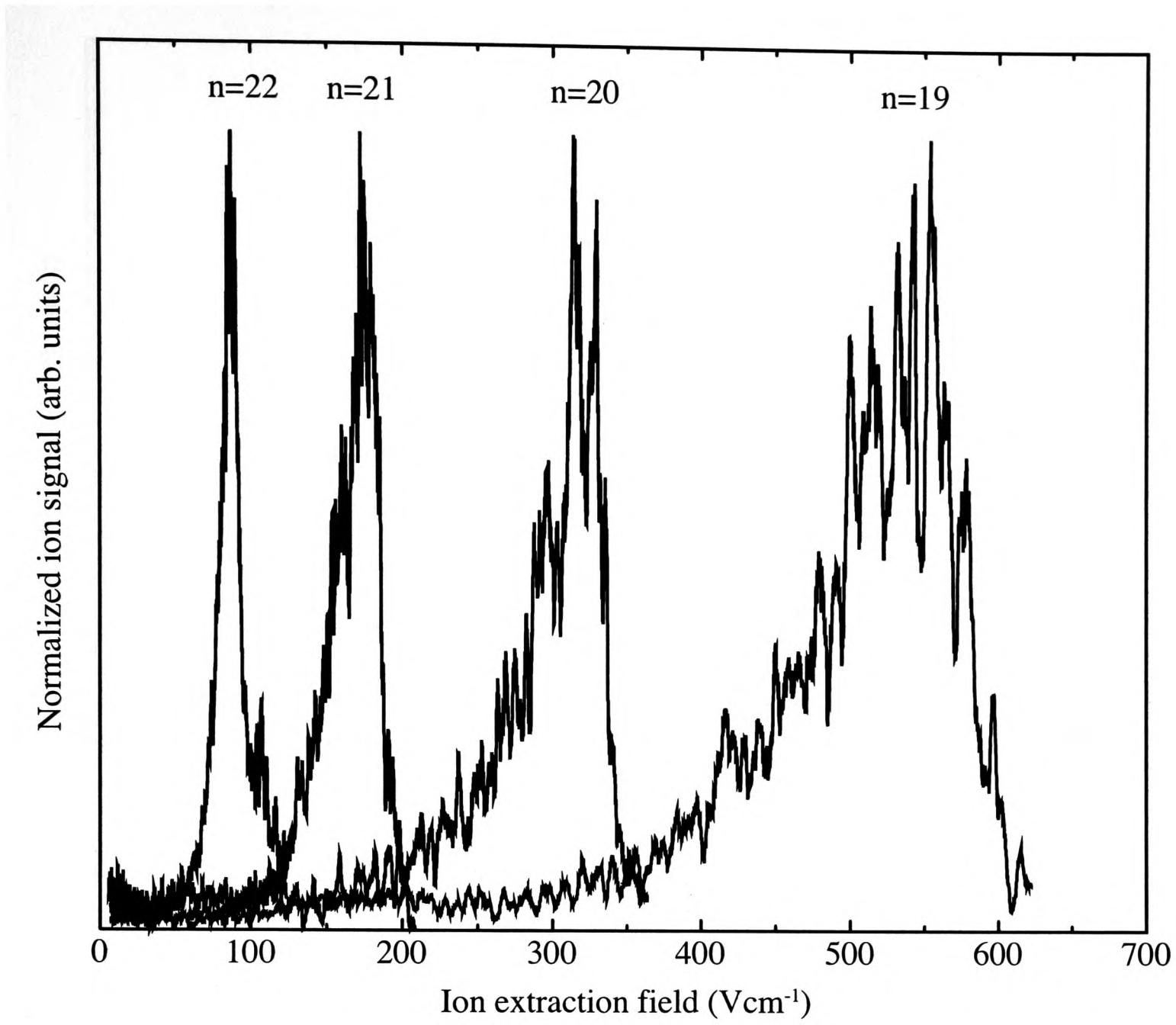

Figure 4.13: *Surface ionisation signal versus applied extraction field strength for population of the* $(nd2)_1$ *Rydberg states, incident on the deposited gold surface, for a range of values* $n = 19 - 22$.

a machined aluminium disc results in a marked change in the ionisation behaviour of the Rydberg states. Once again the investigations focused on initial populations of $(22 - 19d2)_1$ Rydberg states, and the profiles recorded are presented in Figure 4.15. The profiles are offset vertically for clarity. Comparing this data with the deposited aluminium and gold data, shown in Figure 4.5 and Figure 4.13 respectively, it appears that ionisation is detectable at much lower field strengths in the case of the rough surface. Such a result implies that ionisation occurs over a greater range of molecule/surface separation. However, this effect can be attributed to the different topographies characteristic of each surface. The surface analysis reported in Section 3.2.4 indicates that for the deposited aluminium surface the average height fluctuations across a 500 nm sample are less than 2 nm, while the equivalent value for the deposited gold surface is less than 1 nm.

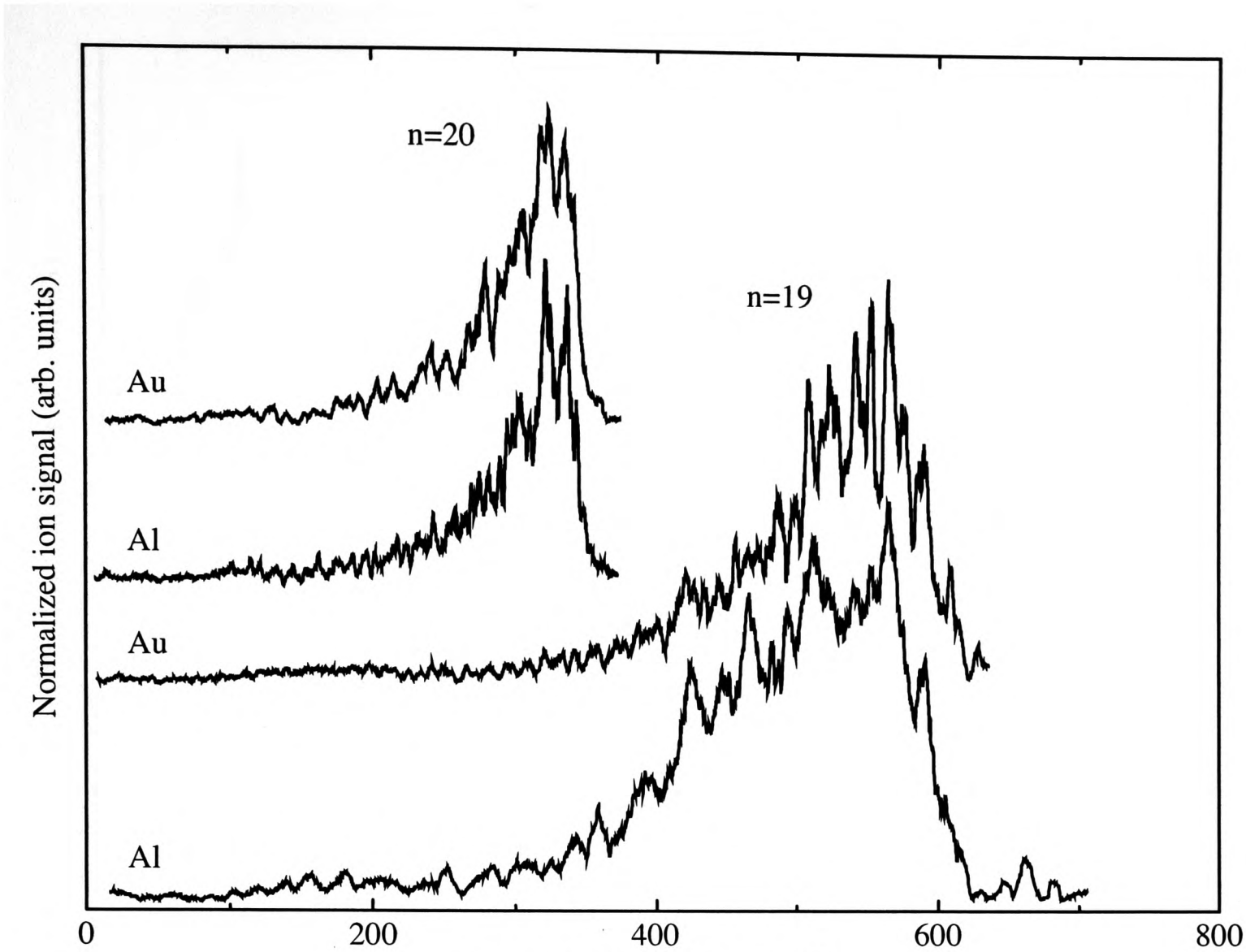

Figure 4.14: *Comparison of surface ionisation profiles for the* $(20d2)_1$ *and* $(19d2)_1$ *states, as labelled in the figure, using deposited gold and deposited aluminium surfaces.*

These two surfaces may therefore be thought of as "flat" from the perspective of an incident Rydberg molecule with a principal quantum number in the range $n = 17 - 22$. However, the machined aluminium has a characteristic roughness in the order of 300 nm with some micron sized defects on the surface. Such significant irregularities lead to a range of effective incident angles relative to the local orientation of the surface plane, resulting in the field profile being extended to lower (corresponding to shallower incident angles) and higher fields. The extension of the profile to higher fields is not observable due to the fact that direct field ionisation successfully competes at such fields, regardless of the nature of the surface, preventing the molecules reaching the region in which surface ionisation may occur. It may also be the case that surface irregularities cause the field to be locally inhomogeneous further modifying the ionisation characteristics of the Rydberg molecules.

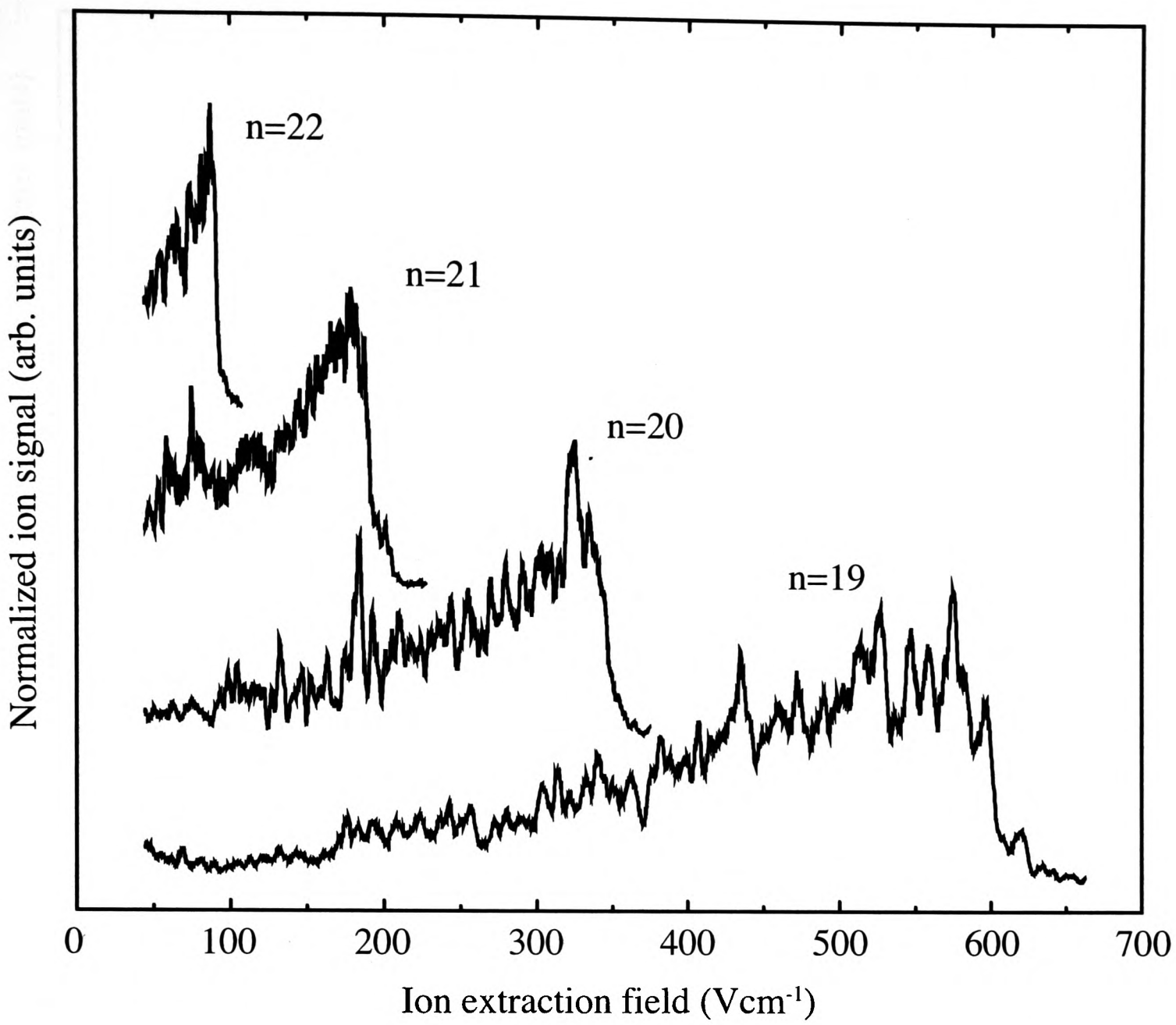

Figure 4.15: *Surface ionisation signal as a function of applied extraction field strength for population of the $(nd2)_1$ Rydberg states, incident on the machined aluminium surface, for a range of values $n = 22 - 19$.*

4.2.8 The presence of structure in the surface ionisation *vs* field profiles

An unexpected feature of the data presented above, for both the $N^+ = 0$ and $N^+ = 2$ states, is the presence of strong resonance behaviour. The profiles do not vary smoothly as the applied field is changed, as was apparently the case in previous measurements on atomic systems [13]. This structure is experimentally reproducible, as illustrated by Figure 4.16 which shows two separate measurements for the profile of the $(17d2)_1$ state incident on the deposited aluminium surface. It is also evident from Figure 4.14 that the resonance behaviour appears to be independent of the type of metal used to form the surface.

One possible explanation of the observed structure lies in the evolution of the

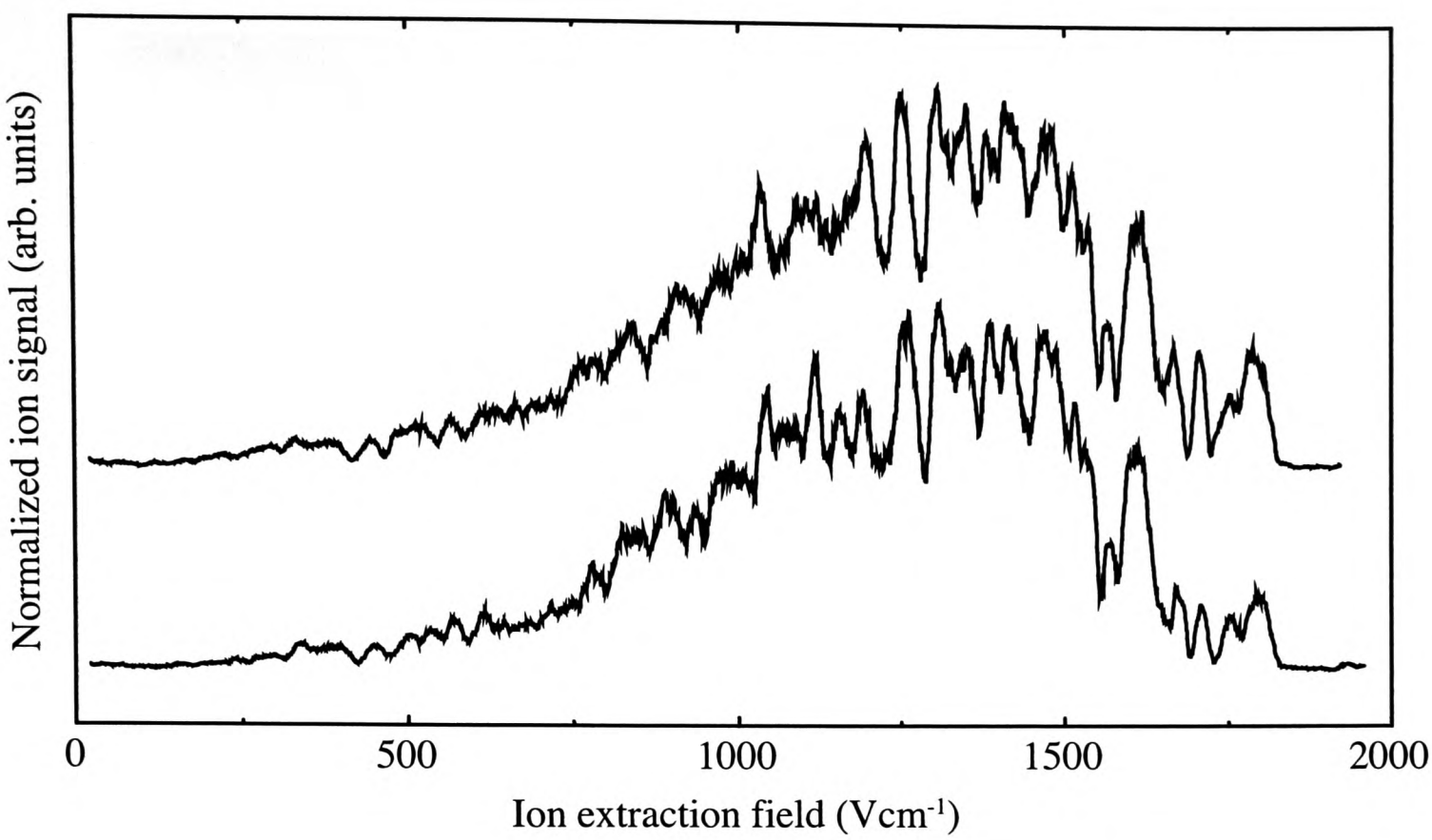

Figure 4.16: *Reproducibility of the surface ionisation signal as a function of extraction field for population of the* $(17d2)_1$ *state, incident on the deposited aluminium surface, in two separate field scans.*

population of the Rydberg state initially prepared in the laser focus. Approximately 800 ns after laser excitation the variable ion-extraction field is ramped up over a period of $\sim$ 100 ns and then held constant. It is feasible that this field ramp may result in the initially populated Rydberg state evolving into a superposition of Stark states. The ionisation behaviour in the presence of the surface potential will now be governed by the dynamics of this superposition, which is related to the magnitude of the applied extraction field.

In the case of an initial population of an $N^+ = 2$ state, it was demonstrated in Section 4.2.2 that the ionisation behaviour exhibited was more characteristic of a state with an effective quantum number defined with respect to the $N^+ = 0$ ionisation threshold. Consequently the presence of resonances may be attributed to a more facile mixing between $N^+ = 0$ and $N^+ = 2$ states for certain amplitudes of the applied field, leading to enhanced surface ionisation probabilities under these conditions. Such an enhancement is possible if the peak of the ramped field corresponds to the field of an avoided level crossing between the initially populated $N^+ = 2$ state and a suitable $N^+ = 0$ state. Analysis of the calculated Stark map [30], reproduced with permission in Figure 4.17, indicates that there are 12 avoided crossings predicted in the range 750-1500 Vcm^{-1} between the extreme red-shifted level of the $N^+ = 2$, $n = 17$ Stark manifold (with which the experi-

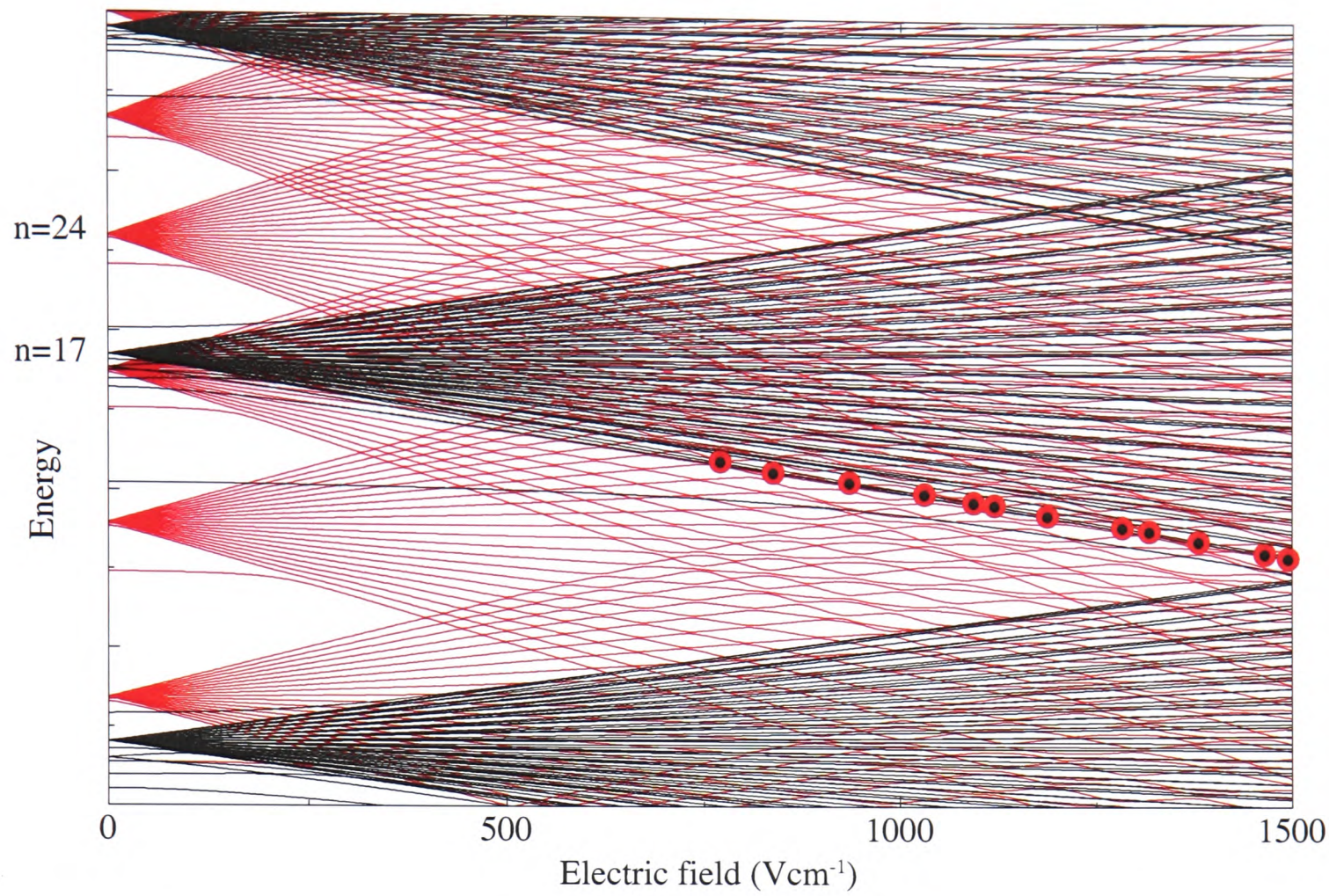

Figure 4.17: *Stark map including all the $N^+ = 0$ ($n = 21 - 26$) and $N^+ = 2$ ($16 - 18$) $M_J = 0$ states. The $N^+ = 0$ states are shown in red. Two states are labelled for reference. The red/black markers show the position of the 12 avoided crossings mentioned in the text.*

mentally populated $17d$ level correlates adiabatically) and the blue-shifted levels of the $N^+ = 0$, $n = 21$ and 22 Stark manifolds. The surface ionisation profile for $n = 17$ shown in Figure 4.16 has approximately the same number of peaks in this field range. While confident that the number of crossing points matches the number of peaks in the surface ionisation profile, the exact position of these crossings do not correlate with the position of the experimentally determined peaks. Owing to resolution limitations it has not, so far, been possible to perform spectroscopic experiments to accurately determine the energies of these crossing points. Consequently, it is not feasible to confirm that the crossings in the calculated Stark map are precisely positioned. As such, while there is qualitative agreement between the surface ionisation profile and the predictions based on the Stark map, no quantitative arguments can be inferred.

A similar but opposite argument can be presented to explain the presence of structure in the profiles collected for an initial population of $N^+ = 0$ states. Rather than thinking of the structure as an enhancement of ionisation probability leading to peaks in the profile, it is necessary to picture the structure as arising

from dips in the profile associated with fields where the Rydberg state is less sensitive to ionisation in the presence of the surface. Such a loss of sensitivity could arise from the $N^+ = 0$ state crossing back to an $N^+ = 2$ state (which requires a higher field for detection) at the crossing points.

4.2.9 Simulating the experimentally observed ionisation behaviour

While the hydrogenic simulations presented in Chapter 2 provide a prediction of the experimentally determined ionisation onset as observed for the $N^+ = 0$ states, and can be seen to provide a prediction of the $N^+ = 2$ behaviour if the necessary change in quantum number is adopted (see Equation 4.7), it is apparent that molecular specific effects can influence the ionisation behaviour of Rydberg hydrogen molecules interacting with metal surfaces. Therefore, in order to more accurately simulate the problem at hand, with the aim of fully understanding both the behaviour of the $N^+ = 2$ states and the presence of structure in the ionisation profiles, it would be necessary to modify the calculations. Adaptation of the model presented in Chapter 2 to include the behaviour of the $N^+ = 2$ states requires that the basis function given in Equation 2.17 is extended to include the rotational wavefunction of the $H_2{}^+$ core. The couplings between the rotational channels could be derived from non-zero quantum defects as shown previously in [30]. Both of these modifications result in considerably expanded matrices and it should be noted that the inclusion of a core rotational angular momentum of 2 actually multiplies the number of basis functions required by a factor of 5. Additionally, the investigation into origin of the structure would require the determination of the evolution of the Rydberg wavefunction, by integration of the time-dependent Schrödinger equation, as it passes a multitude of avoided crossings in the calculated Stark map because the field is ramped up during the molecules approach to the surface. Thus although the necessary methodology is established its implementation would invovle considerable computational challenges.

4.3 Conclusions

The initial investigations into the behaviour of molecular Rydberg states incident on a metal surface that are presented in this chapter have shown that the presence of rotational degrees of freedom does have a significant effect on the tunnelling ionisation process. Firstly, it appears that ionisation is facilitated by the complete transfer of energy from the $H_2{}^+$ ion-core rotation to the Rydberg electron. Such a conclusion can readily be drawn from the markedly different scaling of the molecule/surface separation, Z_i, at which ionisation occurs. For states with no core rotational angular momentum ($N^+ = 0$), Z_i scales as n^2, whilst for those states with two units of core rotational angular momentum ($N^+ = 2$) the scaling factor is ${\nu_0}^2$. Secondly, it appears that the presence of structure is in some way connected to the possibility of coupling between states exhibiting differing degrees of core rotational angular momentum. This differing scaling behaviour raises an interesting question as to whether the structure can be simulated by purely transforming data calculated at lower n. At this time it is felt that this would not be the case and that in order to accurately simulate the interactions of the $N^+ = 0$ states (scaling as n^2) with the $N^+ = 2$ states (scaling as ν_0^2) a full calculation as described in Section 4.2.9 would be required. Such a calculation would necessarily include $N^+ = 0$ states in the range $n = 40 - 50$. Taking this fact, coupled with the increased number of basis functions arising from the inclusion of the rotational wavefunction, it is prudent to ask whether such calculations are feasible.

CHAPTER

FIVE

Conclusions and future investigations

While the interaction of Rydberg atoms with metal surfaces has been investigated in the past, the work contained in this thesis has detailed for the first time the interaction of Rydberg *molecules* with metal surfaces. Experimentally determined surface ionisation profiles as a function of applied field have been presented for Rydberg molecules initially excited to states possessing either 0 or 2 units of core rotational angular momentum ($N^+ = 0$ and 2 respectively). It is shown that ionisation occurs at a molecule/surface separation in the range 3-5n^2a_0 for the $N^+ = 0$ states. This is in good agreement with previous experimental studies involving atoms, as well as theoretical studies based on a purely hydrogenic model. In contrast the behaviour exhibited by the $N^+ = 2$ states does not, at first glance, appear to fit this trend. Scaling the ionisation distance as a function of a new effective principal quantum number, ν_0, defined with respect to the $N^+ = 0$ first ionisation threshold, however, has been shown to indicate that the ionisation occurs at a molecule/surface separation of 3-5$\nu_0^2a_0$. Such an analogous result is attributed to the couplings between the $N^+ = 2$ and $N^+ = 0$ channels. This coupling facilitates the total transfer of rotational energy from the molecule ion core to the Rydberg electron. Thus it is clearly demonstrated that the presence of rotational degrees of freedom has a significant effect on the tunneling ionisation process.

Furthermore, the surface-ionisation profiles presented are not smoothly changing as a function of applied field, instead exhibiting strong resonance behaviour. The experimental reproducibility of this structure, together with the fact that the

observed effect does not change with variation of field step size, or the position at which the beam strikes the surface, indicates that this is a real phenomenon rather than an experimental artifact. While a plausible explanation has been discussed, suggesting that an enhancement of ionisation probability occurs at fields which correspond to avoided crossings in the Stark map between the $N^+ = 0$ and $N^+ = 2$ states, the exact origin of this structure has yet to be firmly established. Indeed it is not clear whether this is a feature exhibited solely by Rydberg *molecules* and, as such, experiments involving atomic Rydberg states, carried out in an identical manner to those presented here, would be a useful first step in characterising this structure. Further investigations could also focus on the interaction of other Rydberg molecules such as NO or CO. A comparison between their behaviour and that of hydrogen Rydberg molecules could shed further light on the rôle of channel interactions in the origin of the structure.

Although the above observations constitute the bulk of the experimental investigations, it has also been shown that the particular metal chosen as the target surface has no discernible influence on the ionisation behaviour exhibited by the molecules, when gold is compared to aluminium. Clearly such a small sample of metals does not provide sufficient evidence from which to draw conclusions about the influence of the surface material on the ionisation behaviour. It would, therefore, be of interest to extend the investigations to other metals and perhaps further still to semiconductors.

Furthermore, owing to the particular techniques employed to prepare the surface, it is feasible to control the thickness of the deposited layer. Consequently there is scope within the present setup to investigate the effect that the metal layer thickness has on the ionisation behaviour of the molecules. Recent calculations suggest large variations of ionisation behaviour [87, 88] with film thickness when the thickness is of comparable size to the dimension of the Rydberg orbit (for $n = 20, r_a = 20\text{nm}$).

The development of a theoretical model to simulate the experimentally observed ionisation behaviour is also presented. While a sufficient model has yet to be developed, the discussion of the complex scaling technique, together with the results for a system based on atomic hydrogen, do detail a proof of concept which can provide a stepping stone to the ultimate goal. In order to adapt the model for this new case of a Rydberg molecule interacting with a surface the basis set would need to be extended to include the rotational wavefunction of the $H_2{}^+$ core. A full treatment would additionally require the inclusion of predisso-

ciation and also the determination of the evolution of the Rydberg wavefunction and this is far from trivial.

In conclusion, this work clearly demonstrates that there is a specific molecular effect observed when Rydberg molecules interact with metal surfaces. Future investigations could focus on other molecular effects such as surface induced predissociation of the Rydberg molecules. It is conceivable that the neutral species generated in this process may be detected upon impact with the MCP detector. It may also be feasible to utilise the interaction of Rydberg molecules with surfaces to study reactive processes. In one scenario, the interaction of a Rydberg molecule with adsorbates on the surface may proceed via the transfer of the Rydberg electronic energy into the breaking of a chemical bond, for example a C-H bond, followed by secondary reaction with the incident molecule. It is hoped that this work will stimulate many future investigations into the interactions of Rydberg states with a variety of surfaces.

BIBLIOGRAPHY

[1] H. D. Hagstrum, Phys. Rev. **96**, 336 (1954).

[2] M. L. E. Oliphant and P. B. Moon, Proc. Roy. Soc. London **A127**, 388 (1930).

[3] H. D. Hagstrum, Phys. Rev. **150**, 495 (1966).

[4] K. Dohrenwendt, B. Fischer, and T. Heindorff, Phys. Scr. **41**, 712 (1990).

[5] A. Benninghoven, F. G. Rudenauer, and H. W. Werner, *Secondary Ion Mass Spectrometry: Basic Concepts, Instrumental Aspects, Applications and Trends* (J Wiley & Sons, New York, 1987).

[6] P. Williams, Appl. Surf. Sci. **13**, 241 (1982).

[7] J. Ishikawa, *Handbook of Ion Sources* (CRC Press, 1995), p. 289.

[8] J. Los and J. J. C. Geerlings, Phys. Rep. **190**, 133 (1990).

[9] C. Fabre, M. Gross, J. M. Raimond, and S. Haroche, J. Phys. B. **16**, L671 (1983).

[10] C. A. Kocher and C. R. Taylor, Phys. Lett. A **124**, 68 (1987).

[11] C. A. Kocher and G. E. McCown, Surf. Sci. **244**, 321 (1991).

[12] D. F. Gray, Z. Zheng, K. A. Smith, and F. B. Dunning, Phys. Rev. A **38**, 1601 (1988).

[13] S. B. Hill, C. B. Haich, Z. Zhou, P. Nordlander, and F. B. Dunning, Phys. Rev. Lett. **85**, 5444 (2000).

[14] P. Nordlander and J. C. Tully, Phys. Rev. Lett. **61**, 990 (1988).

[15] Z. Zhou, C. Oubre, S. B. Hill, P. Nordlander, and F. B. Dunning, Nucl. Instrum. & Methods. Phys. Res., Sect. B **193**, 403 (2002).

[16] I. Martinson and L. J. Curtis, Nucl. Instrum. & Methods. Phys. Res., Sect. B (2005).

[17] J. J. Balmer, Ann. Phys. Chem. **25**, 80 (1885).

[18] J. R. Rydberg, Kgl. Svenska Akad. Handl. **23**, 1 (1889).

[19] J. C. Boyce, Rev. Mod. Phys. **13**, 1 (1941).

[20] G. Herzberg, J. Mol. Spec. **33**, 147 (1970).

[21] P. M. Dehmer and W. A. Chupka, J. Chem. Phys. **65**, 2243 (1976).

[22] U. Hollenstein, H. Palm, and F. Merkt, Rev. Sci. Inst. **71**, 4023 (2000).

[23] F. Merkt, Chimia **54**, 89 (2000).

[24] T. P. Softley, Int. Rev. Phys. Chem. **23**, 1 (2004).

[25] A. Sommerfeld, Ann. Phys. Berlin **51**, 1 (1916).

[26] F. Merkt, S. R. Mackenzie, and T. P. Softley, J. Chem. Phys. **99**, 4213 (1993).

[27] S. R. Mackenzie and T. P. Softley, J. Chem. Phys. **101**, 10609 (1994).

[28] D. Townsend, A. L. Goodgame, S. R. Procter, S. R. Mackenzie, and T. P. Softley, J. Phys. B. **34**, 439 (2001).

[29] S. R. Procter, Y. Yamakita, F. Merkt, and T. P. Softley, Chem. Phys. Lett. **374**, 667 (2003).

[30] Y. Yamakita, S. R. Procter, A. L. Goodgame, T. P. Softley, and F. Merkt, J. Chem. Phys. **121**, 1419 (2004).

[31] E. Vliegen and F. Merkt, J. Phys. B. **38**, 1623 (2005).

[32] H. L. Bethlem, F. M. H. Crompvoets, R. T. Jongma, S. Y. T. van de Meerakker, and G. Meijer, Phys. Rev. A **65**, 053416/1 (2002).

[33] N. Bohr, Philos. Mag. **26**, 1 (1913).

[34] B. Broers, J. F. Christian, J. H. Hoogenraad, W. J. van der Zande, H. B. van Linden van den Heuvell, and L. D. Noordam, Phys. Rev. Lett. **71**, 344 (1993).

[35] J. R. R. Verlet and H. H. Fielding, Int. Rev. Phys. Chem. **20**, 283 (2001).

[36] M. J. Seaton, Rep. Prog. Phys. **46**, 167 (1983).

[37] C. Fabre and S. Haroche, *Rydberg States of Atoms and Molecules* (Cambridge University Press, 1983).

[38] G. Herzberg and C. Jungen, J. Mol. Spec. **41**, 425 (1972).

[39] G. Herzberg and C. Jungen, J. Chem. Phys. **77**, 5876 (1982).

[40] B. H. Bransden and C. J. Joachain, *Physics of Atoms and Molecules* (Wiley, 1983).

[41] T. F. Gallagher and W. E. Cooke, Phys. Rev. Lett. **42**, 835 (1979).

[42] T. F. Gallagher and W. E. Cooke, Phys. Rev. A **20**, 670 (1979).

[43] F. Gounand, P. R. Fournier, J. Cuvellier, and J. Berlande, Phys. Lett. A **59A**, 23 (1976).

[44] T. F. Gallagher, *Rydberg Atoms* (Cambridge University Press, 1994).

[45] H. A. Bethe and E. E. Salpeter, *Quantum Mechanics of One- and Two- Electron Atoms* (Springer, 1957).

[46] F. Merkt and T. P. Softley, *VUV Photoelectron Spectroscopy; Final State Interactions in Small Molecular Systems* (Wiley, 1995).

[47] R. F. Stebbings and F. B. Dunning, Phys. Rev. A **8**, 665 (1973).

[48] R. S. Berry, J. Chem. Phys. **45**, 1228 (1966).

[49] R. N. Zare, *Angular Momentum* (Wiley, 1988).

[50] R. J. Damburg and V. V. Kolosov, J. Phys. B. **12**, 2637 (1979).

[51] H. J. Silverstone, Phys. Rev. A **18**, 1853 (1978).

[52] G. Valent, Amer. J. Phys. **71**, 171 (2003).

[53] J. R. Oppenheimer, Phys. Rev. **31**, 66 (1928).

[54] F. Merkt, Annu. Rev. Phys. Chem. **48**, 675 (1997).

[55] W. A. Chupka, J. Chem. Phys. **98**, 4520 (1993).

[56] F. Merkt, R. J. Rednall, S. R. Mackenzie, and T. P. Softley, Phys. Rev. Lett. **76**, 3526 (1996).

[57] S. R. Procter, D. Phil. thesis, University of Oxford (2004).

[58] J. R. Rubbmark, M. M. Kash, M. G. Littman, and D. Kleppner, Phys. Rev. A **23**, 3107 (1981).

[59] I. V. Komarov, T. P. Grozdanov, and R. K. Janev, J. Phys. B. **13**, L573 (1980).

[60] U. Even, Philos. Trans. Roy. Soc. London **355**, 1539 (1997).

[61] F. Merkt and R. N. Zare, J. Chem. Phys. **101**, 3495 (1994).

[62] T. P. Softley and R. J. Rednall, J. Chem. Phys. **112**, 7992 (2000).

[63] H. D. Hagstrum, J. Vac. Sci. & Tech. **12**, 7 (1975).

[64] M. Remy, J. Comp. Phys. **53**, 2487 (1970).

[65] J. W. Gadzuk, Phys. Rev. B **1**, 2110 (1970).

[66] A. G. Borisov, D. Teillet-Billy, and J. P. Gauyacq, Nucl. Instrum. & Methods. Phys. Res., Sect. B **78**, 49 (1993).

[67] S. A. Deutscher, X. Yang, and B. Joachim, Phys. Rev. A **55**, 466 (1997).

[68] W. P. Reinhardt, Int. J. Quant. Chem. **S10**, 359 (1976).

[69] B. R. Junker, Adv. At. Mol. Phys. **18**, 107 (1982).

[70] W. P. Reinhardt, Annu. Rev. Phys. Chem. **33**, 223 (1982).

[71] N. Moiseyev, Phys. Rep. **302**, 211 (1998).

[72] A. J. F. Siegert, Phys. Rev. **56**, 750 (1939).

[73] J. Aguilar and J. M. Combes, Comm. Math. Phys. **22**, 269 (1971).

[74] E. Balslev and J. M. Combes, Comm. Math. Phys. **22**, 280 (1971).

[75] N. D. Lang and W. Kohn, Phys. Rev. B **1**, 4555 (1970).

[76] P. Nordlander and J. C. Tully, Phys. Rev. B **42**, 5564 (1990).

[77] P. J. Jennings, R. O. Jones, and M. Weinert, Phys. Rev. B **37**, 6113 (1988).

[78] M. Abramovitch and I. A. Stegun, *Handbook of mathematical functions* (Dover, 1965).

[79] A. A. Radzig and B. M. Smirnov, *Reference data on atoms, molecules and ions* (Springer, 1985), p. 396.

[80] H. Rottke and K. H. Welge, J. Chem. Phys. **97**, 908 (1992).

[81] J. M. Gilligan and E. E. Eyler, Phys. Rev. A **46**, 3976 (1992).

[82] S. R. Mackenzie, D. Phil. thesis, University of Oxford (1995).

[83] W. L. Glab, K. Qin, and M. Bistransin, J. Chem. Phys. **102**, 2338 (1995).

[84] H. H. Fielding and T. P. Softley, J. Phys. B **25**, 4125 (1992).

[85] A. L. Goodgame, H. Dickinson, S. R. Mackenzie, and T. P. Softley, J. Chem. Phys. **196**, 4922 (2002).

[86] M. Pounds, Part II thesis, University of Oxford (2005).

[87] B. Bahrim, P. Kürpick, U. Thumm, and U. Wille, Nucl. Instrum. & Methods. Phys. Res., Sect. B **164-165**, 614 (2000).

[88] U. Thumm, P. Kürpick, and U. Wille, Phys. Rev. B **61**, 3067 (2000).